QUEEN MARY UNIVERSITY OF LONDON

A COMPUTATIONAL STUDY OF COOLING VIA ULTRASOUND ENHANCED HEAT TRANSFER OF ACOUSTICALLY DRIVEN FLOWS

by

RAHEEM ABBAS NABI

A thesis
submitted in full fulfillment of the requirements
for the Doctorate of Philosophy in Aerospace Engineering
to the School of Engineering and Material Science
at the Queen Mary College, University of London

London, United Kingdom
April 2022

Date of thesis defense: June, 2022

DECLARATION

I declare that the contents of this dissertation are original and it has not been submitted in whole or in part for consideration for any other degree or qualification in this, except for those with specific reference made to the work of others. This dissertation is based on my own work and includes nothing which is the outcome of work done in collaboration, except that where specific indications have been made in the text.

Raheem Abbas Nabi

April 2022

ACKNOWLEDGEMENTS

ABSTRACT

Previous work has shown that acoustic streaming improves heat transfer via enhanced fluid mixing. A fluid undergoing ultrasonic propagation is seen to exhibit distinctive circulatory flow structures that encourage thermal boundary layer dispersion of any given heat source. The work is found to be essential for enhanced cooling in applications such as microelectronics where the use of thermoacoustic engines can be used to continually provide a cooled environment though enhanced heat transfer. Computational Fluid Dynamics can provide an in-depth understanding of the flow structures and resulting behaviours for a fluid undergoing acoustic streaming. A computational procedure has been developed to simulate the acoustic effects of a given fluid from a 2nd-order solution. The model was found to produce results that formed a good approximation to the experimentation, built upon a base convection model whose mesh was validated using a previous experiment to observe thermal boundary layer behaviour.

A detailed frequency study on the effects of fluid structure and development was modelled in a given geometry. A study was conducted on the mechanisms behind the flow development between each incremental rise in frequency. It was found that a change was induced between the number of circulatory loops in each configuration along with a cut-off point in frequency magnitude beyond which the circulation was found to concentrate around the acoustic source.

Insight into the degree of dynamic stability was gained through modelling the fluid through one wave period where it was found that the model was able to resolve the expansive and contractive behaviour of a boundary layer through one wave period. The results were also able to visualise the cooling mechanisms by resolving the temperature distribution across the entire period. The effects of geometry on heat transfer were studied to ascertain an optimum configuration where enhanced heat transfer was seen to be at its greatest for the given domain. A detailed study of geometry height was conducted to investigate the changes in loop formulation and the consequential effect on heat transfer. Heat transfer was found to correlate with flow structure stability in which two distinctive counter rotating loops resulted in an increase disruption to the thermal boundary layer. This was found to happen in the medium position of the height range.

TABLE OF CONTENTS

ILLUSTRATIONS

LIST OF SYMBOLS

A	amplitude (unless stated otherwise)
c	speed of Sound
F	"function of parameter" term
h	heat Transfer Coefficient
i	sound intensity
I	acoustic intensity
k	specific dissipation energy (unless stated otherwise)
K	kinematic momentum
L	length of enclosure path
Nu	nusselt number
p	pressure
P_{rms}	root mean square acoustic pressure
q	volumetric heat supply
R	radius
Re	reynolds number
S	acoustic jet width
t	time
T	temperature, measured in Kelvin
u	velocity
x	unit of length
X	unit of length (for the purposes of derivation)
$Greeks$	
α	acoustic pressure attenuation
β	thermal expansion coefficient
δ	viscous penetration depth
η	thermal diffusivity
λ	wavelength
ρ	density
ρ_{lin}	linear density
μ	kinematic viscosity
ν	dynamic viscosity
ω	angular frequency
$Subscripts$	
0	zeroth order

1   first order
2   second order

Chapter 1

Background

A prime goal behind the design of engineering systems is the optimization of engineering efficiencies. This entices a variety of methods to streamline operational capabilities, including but not limited to improved cleaning, intensifying chemical reactions, drying and even welding. The focus on this thesis is however the improvement of the heat transfer process for wider engineering applications related to enhanced cooling. This is particularly important for the design of components such as heat exchangers, thermoacoustic devices and so forth. In this context, ultrasound has played a major role in the manor of heat transfer enhancement in a fluid medium. Several phenomena result from ultrasonic propagation in a liquid. One of them, of major importance for heat transfer enhancement is acoustic streaming. The speed gained by the fluid as a result of this phenomena, allows for a better convection heat transfer coefficient near the solid boundaries, occasionally leading to turbulence and thus promoting better heat transfer. Its appearance is distinctly characterised by a pair of circulatory convection cells that are counter-rotating. Several mathematical descriptions are available to describe the phenomena and will be outlined in this thesis. The overall objective of this work is to build a robust model for CFD that is able to resolve the global effects of acoustic streaming from ultrasonic flow, that can be validated experimentally and can be utilized in a variety of cases. The research therefore has wider implications across the industrial spectrum, from the design of heat exchangers all the way to the feasibility of enhanced cooling for computer chips.

1.1 Ultrasound

Ultrasound is a range of sound waves with frequencies higher than the upper audible limit of human hearing, ranging from 20 kHz up to several GHz. Sound travels in the form of a wave involving the elastic straining of the material therefore the properties of the travelling sound are dependent on the properties of the material. In the case of sound travelling through a fluid, the fluid is compressed and dilated as the wave travels through the medium [1]. In general, for elastic fluids, velocities are presented as follows.

$$C_L = compression wave speed = \left[\frac{K}{\rho}\right]^2 \tag{1.1}$$

K is the bulk stiffness modulus of the fluid. We can therefore deduce that the velocity of the sound wave and its propagation are thus properties of the medium they travel through. The propagation of said sound wave is usually expressed as a complex exponential. Let us consider a particle displacement u, particle velocity v, and pressure σ for a compression wave travelling in the X direction [1]. This can be described by the following.

$$u_X = Ae^{i(kx-\omega t)} \tag{1.2}$$

$$v_x = i\omega u_x \tag{1.3}$$

$$\sigma_X X = i\omega C\rho u_X = C\rho v_X \tag{1.4}$$

A is the displacement of the wave. C in this case is the wave velocity and k is the wave number defined as follows.

$$k = \frac{\omega}{C} = \frac{2\pi}{\lambda} \tag{1.5}$$

Ultrasound has numerous applications both in engineering and medical applications. Their most prominent use in current times is seen in the medical field where their propagation effects are used for imagery purposes for biological tissue. However, over the years they have seen usage in a whole host of practical applications starting in 1912 with the unsuccessful search for the ill-fated RMS Titanic [2]. SONAR (Sound Navigation and Ranging) saw significant military research for their applications, triggered by the start of World War 2, followed by a period in the mid-century in non-destructive testing of materials [3]. Their first use as a diagnostic tool came in 1942 for the localisation of brain tumours [4]. 2D medical imagery was subsequently made possible during this period followed by real-time imaging in 1965 [5].

Most common ultrasonic transducers contain Piezoeletric crystals that are responsible for generating ultrasonic waves. These are crystals that have uniquely electromagnetic properties that allow them to vibrate when an electric current is passed through them. These vibrations generate sound waves between 20 KHz and 8 MHz [6]. Figure 1.1 presents a schematic of this.

1.2   Acoustic Streaming

Ghani et al. [7] defines acoustic streaming as a quasi-steady flow in the direction of wave propagation. The convection yielded subsequently enhances mass transfer. The streaming itself originates from the none-linear effects in the momentum equations for a compressible fluid. Legay [8] explains in greater detail the fluid-wall
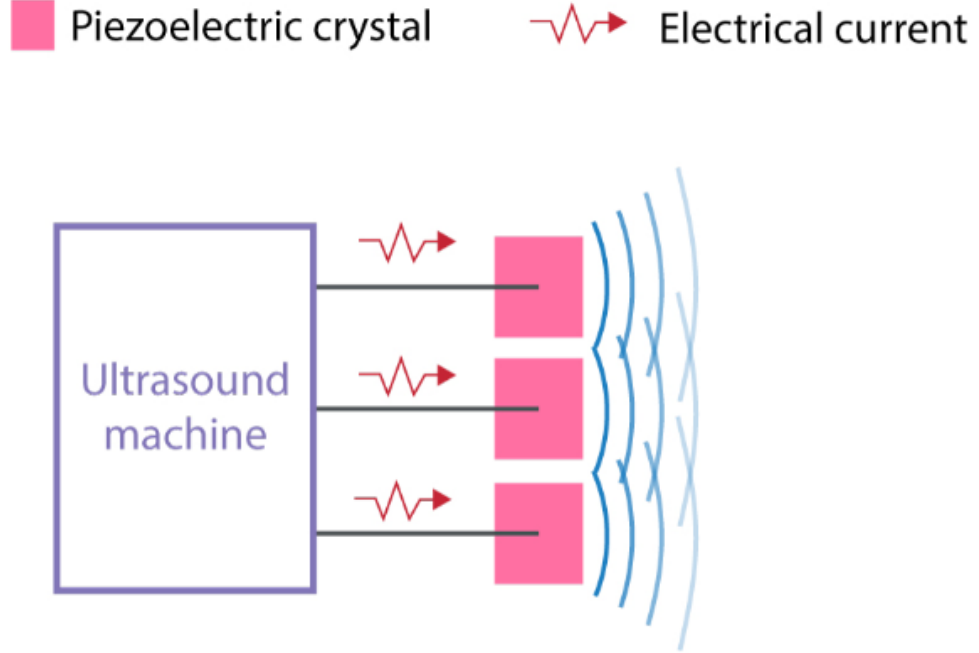
Figure 1.1: Application of a current to a Piezoelectric crystal causes it to vibrate and thus generate ultrasound waves [6]

interaction that subsequently results in enhanced heat transfer. They outline that with the enhanced mass transfer as explained by Ghani et al. [7] that the enhanced fluid-solid interaction disrupts the thermal and velocity boundary layers thus reducing thermal resistance and creating micro-turbulence. This is visualised in Figure 1.2
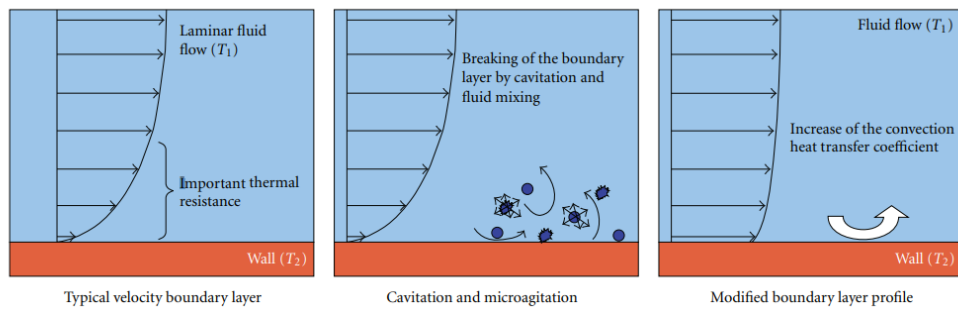
Figure 1.2: Explanation of Heat Transfer Enhance through a closeup of fluid behaviour at the wall [7]

Luo et al. [9] attributed the resulting increased friction between the chamber wall and the fluid to be one of the primary contributors to the none-uniformity of the acoustic pressure in the fluid domain. He also goes on to outline different types of acoustic streaming at different spatial scales. These are Eckhart Streaming,

Rayleigh Streaming and Schlichting Streaming as shown in Figure 1.3 and will be further elaborated on in Chapter 2.
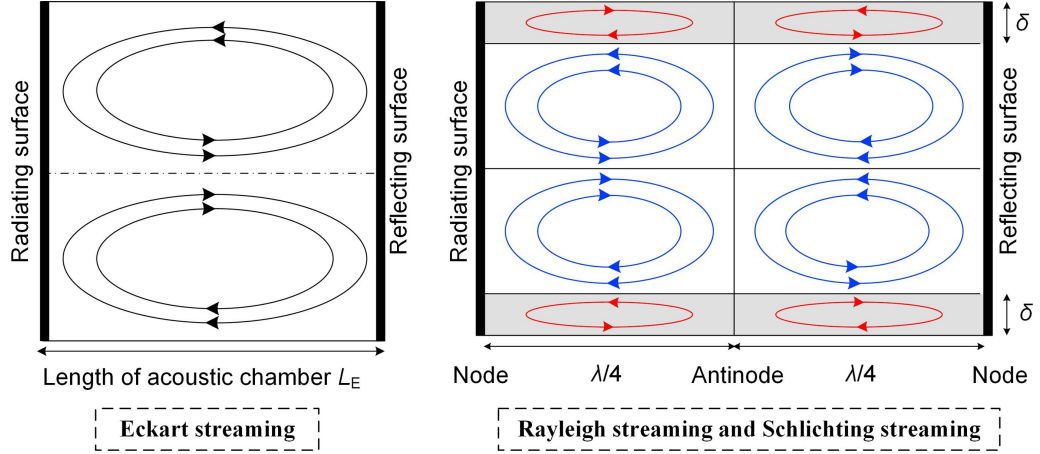
Figure 1.3: Different spatial scales of acoustic streaming [9]

Eckhart Streaming takes place for large scale domains whose sizes are larger than one wavelength. The length of Eckhart streaming tends to be the length of the acoustic chamber. It is sometimes known as "Quartz wind" and is formed from the dissipation of acoustic energy in the bulk of the fluid as defined by Wiklund et al. [10]. The fluid absorbs the acoustic energy at a rate typically proportional to the square of its frequency as specified by Stoke's law of attenuation. The amplitude is found to decrease with distance from the acoustic source and the loss of acoustic energy creates a momentum flux, thus forming a jet of fluid inside the acoustic beam.

1.3 Introduction

In general, the generation of ultrasound can be attributed to a transducer as mentioned in Section 1.1, a device mentioned throughout this investigation (particularly in chapter two) which converts energy from one form to another. The literature throughout chapter two makes mention of piezoelectric devices in their findings. Like Piezoelectric crystals mentioned in Section 1.1, the "Piezoelectric effect" first described in 1880 by Pierre and Jacques Curie (Katzir [11]), is the ability of certain materials to generate a charge in response to applied mechanical stresses. Moreover, an acoustic wave can be generated when a voltage is applied across such a device. Lead zirtcontate titanate (PZT) is used in nearly all ultrasonic transducers and has the added advantage being manufactured in all types of shape with the most common being the circle for single crystal transducer assemblies and rectangle for multiple transducer assemblies.

The potential for ultrasonic applications is boundless and transcends not only the medical field but also the fluids field. Research in fluid dynamics has found that they have enhancing effect on heat transfer across boundaries through two major phenomena; acoustic cavitation and acoustic streaming. The findings of this project and its investigation focus mainly on acoustic streaming. To explain the

mechanism of acoustic streaming we must first refer to Lighthill [12] who provided a comprehensive mathematical description of the phenomena in 1978 for which will be further elaborated in Chapter 2. Principally, he surmised that the dissipation of acoustic energy by acoustic streaming permitted gradients in momentum and therefore fluid currents. In effect, the resulting increase in speed near the solid boundaries allows for a better convection heat transfer coefficient. This resulted from the disruption of the thickness of a thermal boundary layer of any given heat source in the domain considered. Work carried out by authors such as Dehbani et al. [13] and Catarino et al. [14] have shown that it is possible to model ultrasonic perturbations in a computational domain of fluid flow, I.E. in Computational Fluid Dynamics (CFD).

1.4 Acoustic Modelling

Models have already been established to resolve the perturbations of sound through a liquid medium. In particular, we can talk about two distinct approaches; the standardised partial-wave approximations (for which there are several sub-approaches adopted) and full wave modelling.

1.5 Full Wave Modelling

1.5.1 *The Hermoltz Equation*

Having mentioned Lighthills [12] description of acoustic energy dissipation, an example of full wave modelling can be found in the findings of Trujillo [15] and Huttenen et al. [16]. The Hermoltz equation is able to model a continuous wave and has the added advantage (compared to standardised partial differential approaches) of being easily adjusted for complex geometries. Trujillo formulated new expressions for said equation describing the continuous ultrasonic propagation through liquids, coming up with specific formulations for wave number.

Let us consider the spatial variable:

$$r = (x, y, z)$$

The wave equation can subsequently model the linear time dependant pressure field in an inhomogeneous fluid with spatially varying speed of sound:

$$c = c(r)$$

thus the wave equation becomes:

$$\rho \nabla \cdot (\frac{1}{\rho} \nabla P) - \frac{1}{c^2} \frac{\partial^2 P}{\partial t^2} = 0 \tag{1.6}$$

For continuous waves:

$$P(r,t) = p(r)e^{-i\omega t}$$

the wave equation for the spatially dependent part p reduces to the Helmoltz equation:

$$\nabla \cdot (\frac{1}{\rho}\nabla P) + \frac{k^2}{\rho}p = 0 \tag{1.7}$$

The wave number k in this case is defined and the angular frequency is defined as:

$$k = \frac{\omega}{c(r)} + i\alpha(r) \tag{1.8}$$

The angular frequency ω is defined as $\omega = 2\pi f$. In this form, the absorption can be accounted for using complex valued wave numbers where $\alpha(r)$ is the absorption coefficient. Huttenen et al. [16] solved the Hermoltz equation using ultra-weak variational formulation in geometries that consisted of layered structures.

Trujillo [15] was able to build upon this. By developing newer expressions for wave number of a mixture, thus developing the none-linear Hermoltz equation where the wave number k was defined as a function of the pressure amplitude. Further developing on Lighthills description, he found correlation between average acoustic energy and the average energy dissipation for a complex pressure field P where the real part related to the average acoustic energy and the imaginary part related to the average energy dissipation or rate at which kinetic energy was being converted to thermal energy. The equations are as follows:

$$\nabla^2 P + k_m^2 P = 0 \tag{1.9}$$

The wave number k_m^2 for a poly-dispersed population of bubbles can be defined as:

$$k_m^2 = \frac{\omega^2}{c_l^2} + 4\pi\omega^2 N_t ot \int_0^\infty \frac{R_o f(R_o)dR_o}{\omega_o^2 - \omega^2 + 2ib\omega} \tag{1.10}$$

and for non-dispersed populations of bubbles:

$$k_m^2 = \frac{\omega^2}{c_l^2} + \frac{4\pi\omega^2 N_{tot} R_o}{\omega_o^2 - \omega^2 + 2ib\omega} \tag{1.11}$$

where N_{tot} is the local bubble density and $f(R_o)dR_o$ is the probability density function of the equilibrium bubble radius. Trujillo was able to demonstrate the Hermoltz equation without the limit of linearization. He therefore developed new expressions for wave number thus culminating into:

$$\nabla^2 P + \frac{\omega^2}{c_l^2}P = -\frac{\rho_l\omega^2}{\pi}\int_0^{2\pi}\frac{\partial^2\beta}{\partial\tau^2}sin(\tau)d\tau \tag{1.12}$$

The term P in both cases denotes the complex static pressure field denoted by a real and an imaginary part. Here, the unique nature of the model is noted. The overall model is a development of a previous linear model which does not take into account linear radial oscillations. Thus by coupling the real part and an imaginary part of the square of the wave number, a relation is obtained with the energy dissipation density. Thus, correspondingly, representation of the real and imaginary components

of the pressure field allow for both a qualitative and quantitative approximation of experimental pressure distribution. This ability allows for an improved representation of non-uniform pressure fields. Trujillo [15] denotes this as the inhomogeneous Helmholtz equation due to none-zero terms on the right hand side. β in this case is defined as the void fraction, a term that describes the radial oscillation of bubbles at a point in space with respect to time.

As mentioned previously, the correlation derived from the trends between the real and imaginary parts of the source term in the Helmholtz equation where the real part represented the average acoustic energy and the imaginary part represented the average energy dissipation with both predicted from the calculations of the volumetric fluctuations. The work was important due to previous linear models as in Huttenen et al. [16] and their inability to represent acoustic pressure fields because of a lack of dependency on pressure amplitude. (This particularly applies in the context of liquids undergoing acoustic cavitation). The work showed that it was possible to use pressure fluctuations to successfully model sound propagation. Combining this with Huttenunen, the comparisons between continuous wave analysis and peturbations analysis were made clear. The limitations in continuous wave analysis being the fact that mode conversion issues at low angles of incidence led to insufficient modelling- and as a results paved the way for the modelling methodology chosen in this work in the form of perturbation analysis (as outlined in the methodology in Section 3.

1.5.2 *Frequency Power-Law Attenuation*

Another example of full wave modelling as outlined by Szabo makes use of empirical frequency power-law attenuation through a casual convolutional operator directly in the time-domain equation [17]. This specific operator represents the memory effect of the medium which depends on the past history of the wave propagation. It has added advantages over previous models in that it is not restricted to linear functions for frequency and it able to take into account reflection and refraction although it should be noted that a complete time step history would be needed for all acoustic quantities which would therefore limit the models functionality in terms of memory space.

In essence, the acoustic approximation of the original hydrodynamic equations are combined with the frequency power-law attenuation. Acoustic variables p and ρ are considered so that linear equations for conservation of mass and momentum are obtained for a homogeneous ideal fluid model.

$$\frac{\partial p}{\partial t} = -\nabla(\rho_0) \tag{1.13}$$

$$\frac{\partial v}{\partial t} = -\frac{1}{\rho_0}\nabla p \tag{1.14}$$

The system of equations is closed by adding a linear equation of state denoted by $p = p(\rho)$ and in the form $p = c_0^2\rho$.

For homogeneous media, and assuming $p_0(x) = const$ and $\rho_0(x)$ is independent of t, Equation 1.14 should be replaced by

$$\frac{\delta p}{\delta t} = c_0^2 \left[\frac{\delta \rho}{\delta t} + v\nabla\rho_0 \right] \tag{1.15}$$

The frequency power law governs the exponential attenuation with propagation distance δx for an ultrasonic wave in biological media with amplitude $\hat{w}_0$

$$\hat{w}_0(x + \delta x) = \hat{w}_0(x)e^{-\alpha(\omega)\delta x} \tag{1.16}$$

$$\alpha(\omega) = \frac{\alpha_0{}^y}{2\pi} \mod \omega^y \tag{1.17}$$

In this case, $\hat{w}$ denotes the amplitude for any acoutic field variable w such as pressure or velocity. $\alpha(\omega)$ is the attenuation coefficient and α_0 is the attenuation constant. y is the frequency-power exponent and $\omega = 2\pi f$.

The modelling equations for a one-dimensional plane-wave propagation in an ideal lossless medium in the x-direction can be derived using Equation 1.16.

$$\frac{\partial w}{\partial t} + c_0 \frac{\partial w}{\partial x} \tag{1.18}$$

Equation 1.18 can be transformed into the frequency domain with the Fourier transform which leads to

$$\frac{W(x,\omega)}{\partial x} + j\frac{\omega}{c_0}W(x,\omega) = 0 \tag{1.19}$$

Taking into account the dispersion relation $k(\omega) = \beta_0 = \frac{\omega}{c_0}$

Tzabo then introduced what is known as the time-casual model which was able to accurately predict none-linear attenuation. Here, dispersion and attenuation are related through a Hilbert Transform directly in the time domain.

$$L_{\beta'}t = -j sgn(t)L_\alpha(t) \tag{1.20}$$

$$L_\alpha(t) = j sgn(t)L_{\beta'}(t) \tag{1.21}$$

Where $H(t)$ is the Heaviside function and the loss operator L_α is given by

$$L_\alpha(t) = \gamma^1 L_\alpha(\omega) = \frac{1}{2\pi}\int_{\infty}^{-}\infty - \frac{\alpha_0}{(2\pi)^y}|\omega^y|e^{-j\omega t}d\omega \tag{1.22}$$

$$\longrightarrow 2H(t)L_\alpha(t) \tag{1.23}$$

1.6 Partial Analysis

Perturbation analysis (in combination with expansion of equilibrium) as mentioned previously, is the other major approach to modelling acoustic flow. Ovchinnikov et al. [18], broke the method down into well-defined concepts; A stationary component and an oscillatory component for the pressure and velocity field along with an acoustic frequency ω.

$$p = p_0 + Re(p_\omega e^{i\omega t}) \tag{1.24}$$

$$v = v_0 + Re(v_\omega e^{i\omega t}) \tag{1.25}$$

The terms p_ω and v_ω are complex valued amplitudes that represent both magnitude and the phase of acoustic motion. The incompressible Navier-Stokes and continuity equation for the fluid is:

$$\frac{\partial v}{\partial t} + (v \cdot \nabla)v = -\frac{1}{\rho}\nabla p + v\nabla^2 v \tag{1.26}$$

substituting Equation 1.25 into Equation 1.26 and separating the stationary and oscillatory terms yields two equations for oscillatory and steady-state velocities:

$$i\omega v_\omega + (v_0 \cdot \nabla)v_\omega + (v_\omega \cdot \nabla)v_0 = -\frac{1}{\rho}\nabla p_\omega + v\nabla^2 v_\omega \tag{1.27}$$

$$(v_0 \cdot \nabla)v_0 + \frac{1}{2}Re[(v_\omega \cdot \nabla)v_\omega^*] = -\frac{1}{\rho}\nabla p_0 + v\nabla^2 v_0 \tag{1.28}$$

The principal assumption for this approach is that $v_0 << v_\omega$ and that inertial terms in Equation 1.27 are neglected, thus giving rise to the following equation:

$$i\omega v_\omega = -\frac{1}{\rho}\nabla p_\omega + v\nabla^2 v_\omega \tag{1.29}$$

From this approximation, it can be gauged that the steady streaming does not affect the acoustic motion of the fluid.It was stipulated however, that the limitations were the fact that accuracy was compromised at significantly higher amplitudes. This said, Ovchinnikov et al. [18] was able to obtain good agreement between the steady-state solution and the direct transient solution of the Navier-Stokes.

Further work by Trujillo [19] was also conducted on the CFD modelling of acoustic streaming in horn reactors a phenomenon which was first described by Rayleigh as a steady flow in a fluid, induced by the absorption of high amplitude acoustic oscillations. Its appearance is characteristic of a body of fluid formed of distinctive circulatory regions that are counter-rotating, Trujillo [19] was able to obtain good agreement between experimental data and CFD predictions (see the problem shown in Figure 1.4).
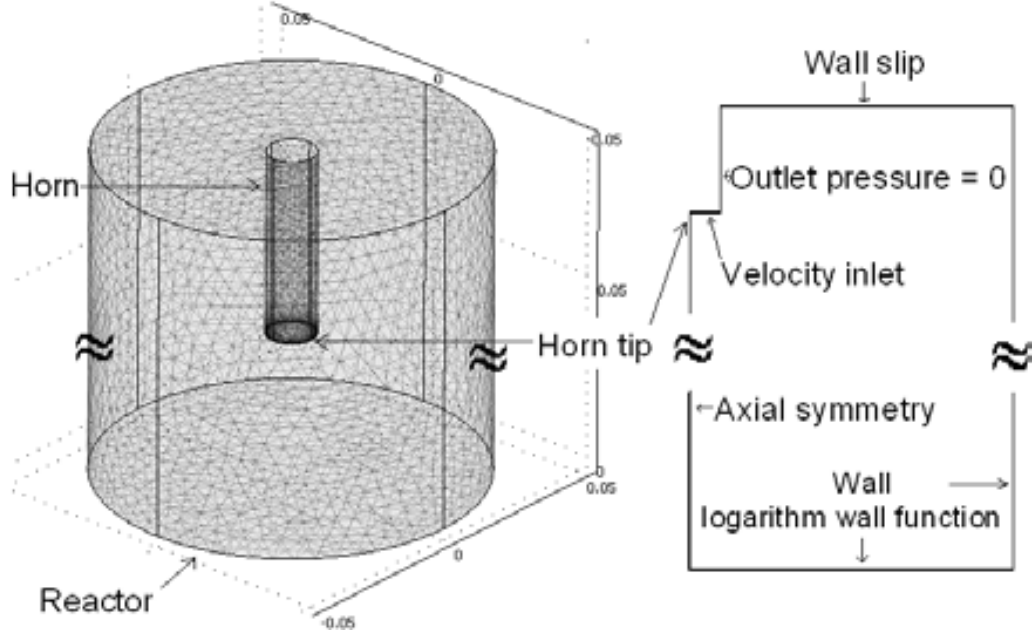
Figure 1.4: Schematic diagram of the problem geometry representing the horn geometry from Trujillo [19] (3D view on the left and 2D axial symmetric cross section on the left showing boundary conditions).

1.7 High vs Low Power Ultrasound

In essence, ultrasonic propagation consists of the propagation of periodic pressure waves in a transmitting medium [20]. The range between 20 and 100 kHz, is often defined as "low frequency" or "high power" [21]. The literature often refers to this range as "power ultrasound" as the sound waves have a high sound intensity of $\geq 0.1 W cm^{-2}$ [22] . Low power, high frequency power on the other hand consisting of a sound intensity between 0.5 to 3.0 W cm^{-2}. In the area of acoustics, sound intensity i is determined as the product of sound pressure and the component of the particle velocity in the direction of the intensity vector. It measures the rate at which work is done on the medium of propagation. It is related to the root mean square (rms) acoustic pressure, and if reflection is neglected and a distance that is considerably far away compared to the location of the source is considered, it follows that [23]:

$$i = \frac{P_{rms}^2}{\rho c} \tag{1.30}$$

where ρc is considered as the acoustic impedance. The term "root mean square acoustic pressure" is defined within the context of a sound signal where instantaneous sound pressures for a given time are squared and then averaged to give the term P_{rms}. The sound power $\dot{W}$ is the total sound energy emitted by a source per unit time measured in watts. It makes use of the integral of the sound intensity i and is defined as the total sound energy propagated by the source in the specified frequency

10

band-width divided by the specified time interval. The sound intensity is integrated over an imaginary surface with area A surrounding a source [23]:

$$\dot{W} = \int_A i \cdot n dA \tag{1.31}$$

The intensity component normal to the enclosing surface is defined as the dot product of i and n. Therefore, if a wave that propagates from rest at time 0 is considered, then the larger the intensity, the larger the sound power hence the term "power ultrasound" is used.

1.8 An Overview of Benefits and Applications

Prominent theoretical studies conducted by Rayleigh [24] and Nyborg [25] are just two examples where mathematical derivations have provided a basis for computational simulations of ultrasound in fluid flow. Within the context of engineering applications, not only is there scope in the research to be able to properly understand the flow physics behind the phenomenon, but further, to also increase the degree of flow control that can be applied to such phenomena. There is a computational challenge on developing solvers that can incorporate the Navier-Stokes equations for incompressible flow and also solve for the compressible perturbations of pressure when a fluid medium is subject to acoustic propagation. This is as much of a research challenge as it is a justification. The need for this research stems from the benefits seen from the associated flow physics. Acoustic streaming in a low Mach fluid flow is seen to have numerous benefits for enhanced heat transfer in engineering systems. Within melting and solidification for example, the improved heat transfer reduces the size of ice crystals in frozen products and therefore an enhancement in quality [26]. Benefits are also seen for the storage and transport of cold thermal energy [27] with cooling being a major energy consuming process, cold thermal energy can be added to a medium, and extracted when needed. It is stored by virtue of change in the internal energy or a phase transformation. In this case, acoustic flow has made the control of supercooled water a possibility. The resulting product is ice slurry, a solid-liquid mixture that can easily be stored and transported. During the discharging process, the cold thermal energy from this storage can be retrieved and supplied for end use in the form of cooling [28] . Furthermore, as highlighted by a review conducted by Legay [8], whilst there is some literature on the effects of ultrasound on heat transfer, numerical studies form a mere percentage of this as seen in Figure 1.5 for a review of 62 papers.

The mathematical description for acoustic streaming was first set by Lighthill [12]. At a microchannel level, the encouragement of fluid mixing by acoustic streaming was found to lead to the provision of additional liquid to a heat transfer surface in certain investigations [29]. Additionally, there are findings to suggest that the heat transfer rate increases linearly with sound amplitude when water is the selected medium. Such findings are important for the potential feasibility of cooling computer chips in laptops, medicinal cleaning in areas such as endodontics and blood flow along with additional applications in food technologies. Enhanced convective
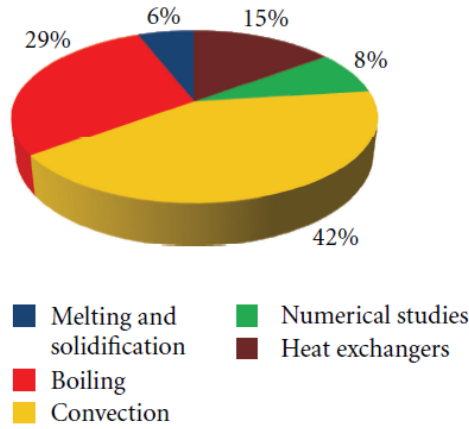
Figure 1.5: Percentage of studies conducted from 62 papers as conducted by Legay [8].

heat transfer is paramount to many engineering applications. The literature has established the observation of acoustic streaming and the effects have been tallied and investigated but not fully understood. If a robust acoustic model is built then systems can be designed with the ability to both predict and control the flow physics of an acoustic flow. Additional applications have also been found in levitation and particle trapping.Marzo et al. [30] for example showed that it was possible to use high speed acoustic vortices to trap and levitate particles using their orbital angular momentum. Settnes and Bruus [31] were able to take this a step further by calculating the acoustic radiation force on compressible spherical particles suspended in a viscous fluid. The aim behind their investigation was to provide an analytical expression for the viscous correction to the acoustic radiation to analyse implications for the studies presented in this thesis on microchannel acoustics.

In previous research the ultrasonic effects of conduction increased the heat transfer coefficient up to 25 times [32]. Lin and Farouk [29] postulated that heat exchangers could be optimized if wave and flow patterns could be predicted precisely. Thus the importance of acoustic streaming and its applications cannot be understated.

1.9 Challenges, Aims and Objectives

Overall, the research challenges of computational studies of ultrasonic effects on heat transfer span from the coupling of an incompressible low Mach flow solver to incorporate the compressible aspects of a pressure-perturbed flow, to the ability to validate this model with reliable data. The aim of this research can be outlined in three main points; Procedure, understanding and applications. A computational procedure will be developed for ultrasound enhanced heat transfer prediction to run multiple simulations. This would be achieved by building a model that is able to increase our understanding of acoustic streaming by accurately predicting the flow physics for various computational cases with benefits to engineering applications by

identifying methods to control the flow. In the process of building such a robust solver, a niche gap in the literature can also be explored. In particular, the increased understanding of the differences between and the challenges associated with an uncoupled and a coupled solver. A parameterization study is the ideal outcome for this research, outlining effects such as geometry height on heat transfer enhancement along with frequency on the changes in flow physics. The solver will be built in OpenFOAM due to the ease of access to its source code and the availability of various heat transfer models with which to build an acoustic model from. The objectives for this research are

- To Choose an appropriate mathematical approach that resolves both the incompressible Navier-Stokes equations and the components that constitute the resulting pressure perturbations from acoustic propagation

- To Establish a validated methodology for convective based flows that gives experimentally validated data that is reliable

- To build a fully validated solver using the established heat transfer model as a base, the model should be robust enough to be easily utilized in a variety of cases

- To conduct a study of batch simulations, identifying the effects on the flow physics whilst varying acoustic quantities such as frequency and amplitude

- To conduct a parametric geometry study based on gaps in the literature to ascertain the most prominent effects on heat transfer

With this in mind, the research of this PhD project is able to pose four major contributions to the CFD knowledge base:

- A methodology that can accurately predict the flow physics of acoustic flow thus providing us with the appropriate understanding to control it

- Research that will contribute to the overall understanding of coupled solvers and their implementation within the Navier-Stokes equations

- Studies of domain aspects such as height which have not been done to such a full degree in the previous literature

- To build upon existing experimental work outlined in their initial observation of the phenomenon, enhancing our understanding of its behaviour, and to be able to provide a knowledge base for engineering applications

The following chapters of this PhD thesis are organised as follows:

- Chapter 2 deals with an introduction to the existing literature, splitting the review into areas covering engineering and biomedical applications, the main two categories that cover applications for this field. Outlined in both are experimental and computational studies of acoustic streaming within the two categories

- Chapter 3 outlines the research methodology for modelling and simulation. Direct method, expansion of equilibrium and perturbation method are three primary computational models that are identified. The section also covers the coupling between CFD and acoustic modelling along with the associated numerical methods

- Chapter 4 is a study of a thermal boundary layer and the resulting effects of changing frequency on an acoustically driven flow. The effects on the boundary layer from parameters such as frequency and amplitude will be studied for a simple duct geometry. The focus here is to produce data for a range of frequencies between 20 kHz and up to 1.7 MHz

- Chapter 5 builds on the results achieved in chapter 4 for the same geometry and boundary conditions and looks at two specific frequencies and their respective dynamic behaviour for similar parameters such as boundary layer size and circulation

- Chapter 6 consists of a geometry study with slightly more complexity, covering a parameterization study of height resolution and its effects on flow structure and heat transfer. The investigation is based on literature from Dehbani et al. [13]

- Chapter 7 will conclude this with final remarks covering a summary of findings and recommendations for further study

Chapter 2

Literature Review

The following chapter is divided into six distinctive sections. Section 4.5 describes the fundamental theory behind acoustic streaming, including the initial mathematical derivations from Lighthill, a summary of the principle flow structure and the literature surrounding this flow structure. Section 2.3 outlines literature on acoustic streaming and its effects on mixing, including the primary factors of acoustic streaming that influence mixing extent. These include the effects of the geometry of the flow domain, the streaming velocity and the boundary layer thickness. Mixing efficiency is also touched upon here in relation to streaming velocity and applied voltage. The investigations were primarily experimental. Maximum streaming velocity is then covered in Section 2.4. In particular, the literature covers micro-devices and the varying effects of their geometry with maximum velocity. The section primarily consists of CFD simulations and identifies trends between acoustic properties such as amplitude and pressure with geometrical aspects such as channel height and radius. Section 2.6 then takes a sidestep towards biomedical applications, outlining the benefits of ultrasound and relating acoustic phenomena such as acoustic streaming and cavitation to the importance of procedures such as ablation and histotripsy. Further work is also covered in the investigation of blood vessels in tumours. The section also summarises the recent publications in the use of ultrasonic instrumentation in endontics. Additional applications are covered in Section 2.7 primarily in industrial cleaning. Section 2.9 covers heat transfer and engineering applications with a specific focus on electronic components with cooling capabilities. Examples include micro-pumps and micro-mixers. Most importantly, three distinct heat transfer mechanisms are identified here; steady streaming due to viscosity dependence, thermoacoustic heat pumping and steady streaming due to oscillating boundaries. The final section (2.10) covers the mathematical approximations behind the flow physics, in particular, the jet velocity distribution from an ultrasonic horn tip. Various researcher use different models, including a Gaussian distribution, a sinusoidal movement to model displacement and a timescale discrimination approach.

15

2.1 Introduction to Acoustic Streaming, its Applications

First discovered by Faraday who observed its behaviour through the motion of powder above a vibrating Chaldni plate [33] [34], Suh [35] defines the phenomenon of acoustic streaming as a steady circulatory current in a fluid field. Originating from the field of acoustics, the phenomenon occurs when a fluid, compressible or incompressible interacts with a certain source of sound. Its appearance is distinctly characterised by circulating cells between nodes [36] and has found applications in micro-cooling [36], Sonochemistry [37] and nanoparticle manipulation [38]. Specifically, within Sonochemistry, there is a wide range of application in various subfields such as chemical synthesis, wastewater treatment, biotechnology and polymer engineering [[39]]. An example of such particle manipulation can be found in an investigation by Collins et al. [40] who captured the mixed suspension of 1 μm particles by characterising the forces relevant for vortex streaming in a combined lateral flow system. A further example of cell suspension can be found in an investigation by Oyama et al. [41] who studied large scale suspension for tissue development as a more efficient form of tissue development. Another investigation is by Spengler and Coakley [42] who studied the aggregation and flocculation of latex particles in an ultrasonic standing wave. The resulting capabilities have allowed for manipulation of objects such as polystrene micro-spheres and even microbubbes [43]. As a consequence, the research has paved the way for non-invasive medical procedure through the manipulation of cells. Bernassau et al. [44] highlighted the importance of further understanding acoustic streaming in the area of tissue engineering as it was often an unwanted side-effect that could disturb medical procedure. Specifically, it was found that for cell patterning and engineering, streaming would effect the positioning of cells, possibly preventing them from adhering to the surface upon which they are growing [45]. Of particular interest to this thesis is the application of acoustic steaming to enhanced heat transfer. Historically, processes such as heat exchange, sublimation and dissolution have seen improvements as a result of vibration mechanisms imposed on the fluid [46]. Baran et al. [47] were able to induce acoustic streaming by the mere vibration of the far-end vertical wall in a narrow u-shaped channel. Richardson [46] focuses on the effects of oscillation on natural convection and highlights the generation of steady secondary flow. The nature of this flow is outlined in more detail in Section 4.5 and classifies distinct regions of streaming such as Schlichting and Eckhart. Already, the research into heat transfer applications is finding traction in areas such as computing. Koster [48] for example has developed a novel type of computing chip that employs acoustic surface waves as a pumping mechanism for fluids. The streaming patterns observed, due to the interaction between the waves and the adjoining volume of fluid allows for a more efficient cooling thus paves the way for the design of smaller cooling devices in the field of microelectronics. Similar work was also conducted by the likes of Maramizonouz et al. [49] who validated computational models for a microfluidic device based on direct calculation of density and velocity fields and also a low-fidelity approach that captured the acoustic streaming effects without modelling the entire acoustic field itself.

The overall research into acoustic streaming in fact transcends that of computing science and can even be found in the field of space exploration. NASA highlighted the absence of buoyancy in micro-gravity, thus potentially leading to the malfunction of any needed heat or mass exchangers [50]. Thus they highlighted acoustic streaming as a method of enforced circulation and continue to conduct research into the development of induced ocillatory motion to control a particle environment, further enhancing the technology developed for microgravity [51]. The justifications for this research are further backed by Hasegawa et al [52] who emphasised the importance of droplet manipulation in low gravity scenarios to conduct mid-air laboratory research. Furthermore, an analysis through direct numerical simulations was conducted by Charrier-Mojtabi et al. [53] to induce species seperation of a binary mixture in a microgravity environment. Within the context of heat transfer for this thesis, research has even been conducted into the negative effects of acoustic streaming in liquid injection rocket engines [54]. The result is an elevated heat transfer to the rocket injector faceplates, strong roll torques and chamber over pressurisation. Thus it can be argued that the importance in increasing understanding and behaviour of acoustic streaming has applications across a vast array of engineering fields that transcends even space exploration.

2.2 Theoretical Background, the Flow Structure and Physics of Acoustic Streaming

For a wave, propagating through a bulk fluid, distinctive convective cells can form in the fluid structure resulting from the momentum gradients created by the acoustic energy dissipation. This is the so called acoustic streaming, a set of equations which were first mathematically derived by Lighthill [12]. Lighthill notes that the streaming motion results from the action of Reynold's stresses whilst the momentum flux that induces this streaming motion is originates from the dissipation of acoustic energy flux. Two fundamental equations were derived for a narrow ultraonsic beam of cross-sectional area S_b; The force acting per unit length F_l and the resulting intergral along its length to output the total force acting F_t.

$$F_l = \frac{1}{3}\rho_0 U_0^2 S_b \frac{\delta\omega}{c} e^{-4\frac{\delta x}{3}} \tag{2.1}$$

$$F_t = \frac{1}{4}\rho_0 U_0^2 S_b \tag{2.2}$$

Lighthill was able to show that if P is the power, measured in watts, emitted by the acoustic source in a narrow beam then it can be said that:

$$F_t = \frac{P}{c} \tag{2.3}$$

thus using both equations for F_t it can be said that:

$$U_0 = 2\left[\frac{P}{\rho c S_b}\right]^{\frac{1}{2}} \tag{2.4}$$

If the total force produces acoustic streaming with a characteristic velocity U_s in a system with length scale l then $U_s = \frac{U_0 S_b}{l^2} = 2\left(\frac{PS_b}{\rho_0 cl^4}\right)$. This in turn gives a streaming Reynold's number R_s:

$$R_s = \frac{U_s l}{v} = 2\left[\frac{PS_b}{\mu v c l^2}\right]^{\frac{1}{2}} = O(QS_b)^{\frac{1}{2}} \tag{2.5}$$

Visibly, a fluid undergoing acoustic streaming can be characterised by symmetrical pairs of circulatory cells in its fluid structure. Throughout the literature the acoustically driven flow is found to undergo stationary re-circulation in the context of these cells. Their structure does not change with time.

Acoustic streaming can be classed into several types as defined by Riley [55]. Rayleigh Streaming is defined as streaming within the boundary layer and is defined by the acoustic energy dissipation within the stokes boundary layer adjacent to the solid boundaries. Schlichting streaming (or inner streaming which exists as a steady cell of flow that circulates in the opposite direction to the surface bound Rayleigh streaming. Landau and Lifshitz [56] highlight that Rayleigh Streaming is especially prominent under the condition $\lambda >> h >> \delta_v$ where λ is the acoustic wavelength, h is the characteristic length scale of the fluid and δ_v is the viscous penetration depth. For an oscillating flow this is given by:

$$\delta_v = \sqrt{2v/\omega} \tag{2.6}$$

So for an ultrasonic propagation in the low MHz range λ is of order of $1mm$ and δ_v is of the order $1\mu m$. Thus Rayleigh streaming is theorised to be most pronounced for chambers with length scales that are a fraction of the wavelength. Tan and Yeo [57] also confirmed this, highlighting the difference in modelling approaches between bulk streaming in the fluid domain for larger channel heights and surface bound Rayleigh streaming. They found ironically, that at this scale of flow, the inertial-dominant flow resembled a parabolic velocity profile for pressure-driven laminar flow. Figure 2.1 presents an outline of the Rayleigh-bound vs Schlichting structure in more detail:

With regards to the fluid structure itself, as noted in Figure 2.1, Rayleigh [24] was also able to show the formation of two streaming vortices formed per quarter wavelength ($\lambda/4$). This was for a standard parallel plate channel with infinite length with a standing wavelength much larger than the plate separation where the two vortices formed symmetrically around the channel centreline. It can be seen as demonstrated by Figure 2.1 that for a two-dimensional formation that the vortices form perpendicularly to the face of the acoustic transducer. These findings correspond well with those of Tajik et al. [58] who identified that there was an even number of vertical loops with the quantity being half the wavelength. When they set the enclosure height to equal the wavelength, the primary circulation was found to divide into two smaller circulations with half thicknesses. Osipov and Almakaev [59] studied the effects of acoustic streaming on aerosol particles in a polytropic gas using a numerical model compiled in OpenFOAM. They confirmed a structure similar to figure 2 in that two inner Schlichting vortices and two outer Rayleigh vortices formed. The region of contact between these the inner and outer vortices was found
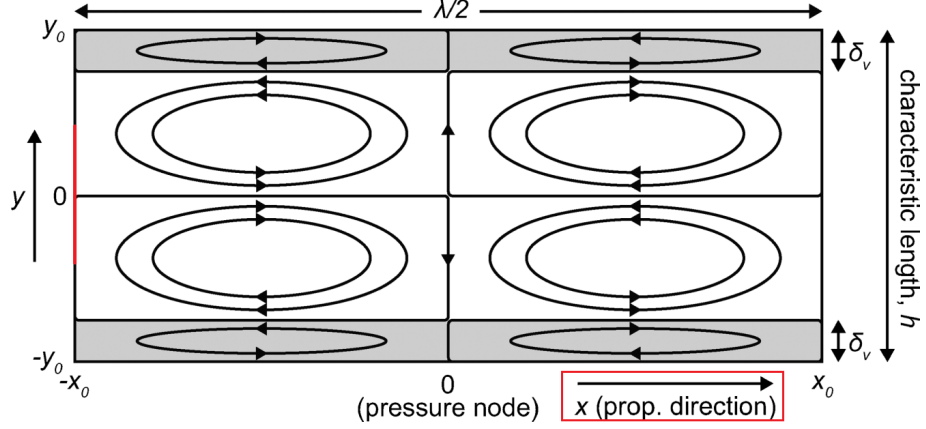
Figure 2.1: A schematic that conveys the inner vs outer fluid structure for counter-circulating flow between the inner Schlichting (white areas) streaming and outer Rayleigh streaming near the solid boundary (grey areas) [10] Transducer source is marked in red on the wall of the left hand side of the domain and the propagation direction in the x direction is indicated and highlighted in red at the bottom right.

to have the highest streaming velocity. The two Schlichting vortices appear inside the boundary layer with a thickness δ:

$$2\delta = 2\sqrt{\frac{2\mu}{\rho_0\omega}} \tag{2.7}$$

Wang and Kuznetsov [60] on the other hand found that acoustic streaming velocity created four circulatory loops within each wave length for a height of 1.5 mm and a wavelength of 20 mm.

From this, it is clear that the literature points to an even number of circulation regions. Fand and Kaye [61] agrees with Wang and Kuznetsov [60], identifying four loops specifically in an experiment using smoke for streaming in a heated cylinder. Increasing acoustic intensity was found to increase circulation size and thus the subsequent heat enhancing effects of acoustic streaming although they noted that there came a critical point where circulation size seized to have any further effect on heat transfer enhancement. It should be noted for the purposes of this thesis that the acoustic intensity is expressed by the Gaussian function[62]. The volumetric heat supply associated with both the acoustic beam and for the bulk fluid is given by [62]

$$q_f = 2\alpha_f I \tag{2.8}$$

$$q_s = 2\alpha_s I \tag{2.9}$$

The subscript for f and s represent values for the fluid and solid respectively. $I = |I|$ is the acoustic intensity magnitude.

Lei et al. [63] also confirmed such behaviour. Through experimental investigations they were able to confirm a number of conditions as shown in Figure 2.2. When $h/l_c \leq 1/20$ they found that transducer plain streaming occurred, as confirmed also by Bahrani et al. [64] who was able to show Rayleigh like streaming behaviour in a millichannel fed by two fluids coupled to a piezoelectric transducer. The investigation aimed to show enhanced mixing and its effects on improving average temperature, in particular, through the formation of vortices.
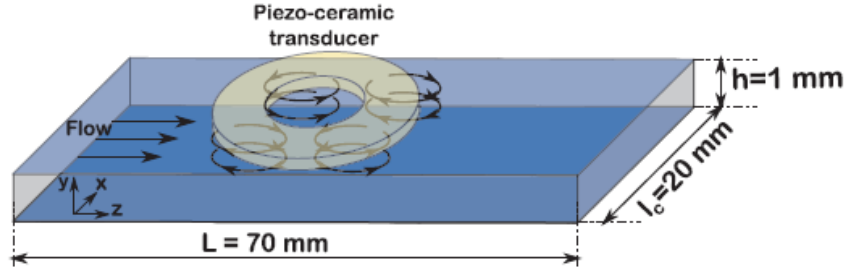
Figure 2.2: A schematic showing Rayleigh like conditions based on a condition identified by Lei et al. [63] where $h/l_c \leq 1/20$.

2.3 Acoustic Streaming: Effects on Circulation and Mixing

Section 4.1 provides information on how heat transfer is enhanced through mixing and subsequent heat transport. We should refer back to Figure 1.2 which provides an overview of thermal boundary layer mixing from a molecular point of view through thermal boundary layer resistance. According to Ghani et al. [7] this leads to a reduction in thermal resistance and an increase in microturbulence. According to Guo and Sun [65], the forced convection that creates this mixing carries heat away from the thermal boundary layer thus breaking down the fluid structure. Thus in the context of mixing for this section, mixing refers to this very dynamic (the mixing of hot and cold fluid). Molecular mixing will also be discussed. The first example talks about the mixing of two similar fluids with different temperatures. The greater the circulation, the greater the mixing of two individual fluids. Work on the effects of acoustic streaming on circulation was conducted by Zhang [66], again making use of microchannel and low frequency transducers. The study was interesting in that it looked at the influence of a sharp structure on streaming flow. Mixing performance was observed for different tip angles. Counter rotating symmetrical vortices were observed when the flow rate was zero and the symmetry was found to be broken when the flow rate was turned on. It was also found that with the flow rate diverted into the direction of propagation the characteristic flow structure broke down. This is shown in Figure 2.3c for reference. It was found that stronger streaming could be induced by sharper tips thus achieving better mixing. This is clearly indicated by the higher velocity ranges between Figures 2.3a and 2.3b.

In other work, mixing at a molecular level was also found to be influenced by other factors. In particular, aspects of the fluid structure itself such as streaming
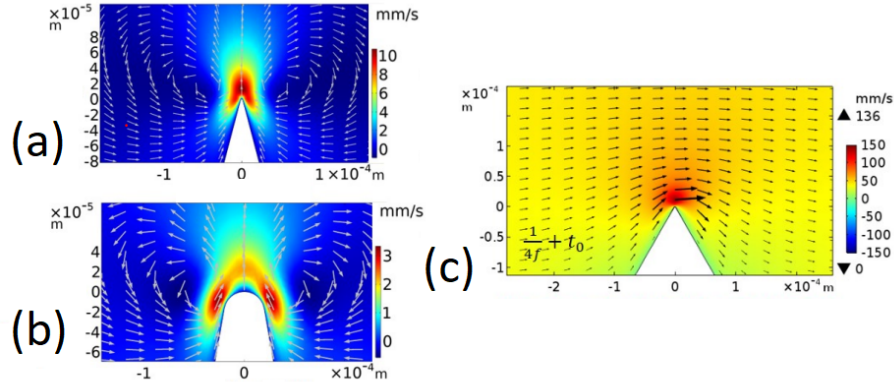
Figure 2.3: Velocity plots for (a) a sharp-edged tip, (b) a blunt edged tip (c) a sharp edged tip with a flow rate [66].

velocity. Setareh et al. [67], for example studied the mixing effect in a microfluidic device between two side-by-side fluids; Water and fluorescent die solution. He found that mixing efficiency is a second order function of the applied voltage across an acoustic transducer. This is because the velocity of acoustic streaming is proportional to the square of the applied voltage. The work was carried out using a Surface-Acoustic-Wave micromixer. As explained by Nyborg [25] , one must obtain an initial first-order and then second-order solution for acoustic streaming where second-order denotes the mean global streaming flow and takes the second order derivative of the Navier-Stokes equations. Since second-order velocity for the mean global streaming flow is linked to mixing, it was deduced that mixing efficiency is also a second order function of applied voltage. The terms first and second order will thus be utilized throughout this section and should thus be considered as such. The perturbation method, which will be outlined in Chapter 3 makes use of these first and second order terms. Where a Newtonian fluid is formed from derivatives from the sum of all first order stress tensors, the term "second order fluid" as defined by Rivlin and Ericksen [68], is a fluid where the stress tensor is the sum of all tensors that can be formed from the velocity field with up to two derivatives. Wan and Kuznetsov [60] were able to compute a first-order harmonic velocity field which was then used as known data for a steady-state solution for acoustic streaming. Here, a comparison was made between a numerical analysis and an experimental setup of a heat source giving off a constant heat flux, between two flexural plates as shown in Figure 2.4. They also modelled the same setup but for a heat source with a constant temperature

In the experiment, they found that acoustic streaming decreased the average temperature of the upper beam by 1.35 K for a constant heat flux. The results are presented in Figure 2.5.

Setereh at al [69] found that enhanced mixing reduced the thickness of the thermal and hydrodynamic boundary layers (as explained in Section 1.2. As in the case of Zhang [66], their setup also involved the study of mixing between hot and cold fluids. In this case, the setup was in the form of a double pipe heat exchanger as
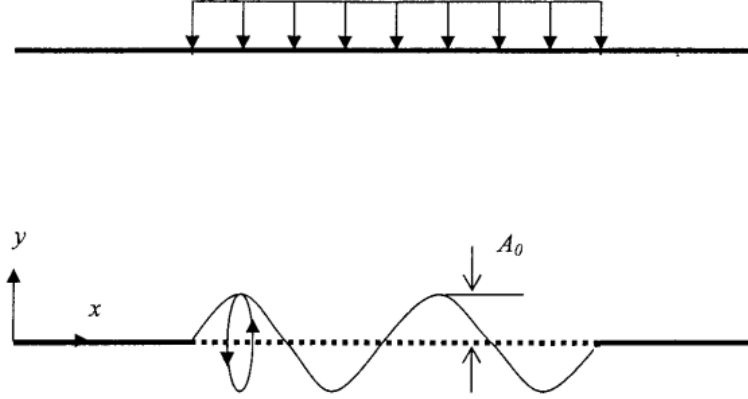
Figure 2.4: two flexural plates with the a constant heat flux set to the top plate [60].

presented in Figure 2.6.

Stronger circulations were found to have generated at higher acoustic pressure and that the magnitude of second-order velocity into the circulations near the wall of the inner pipe become larger as presented in Figure 2.7.

Again, second-order velocity must be considered as the second order derivative of the Navier Stokes as defined by Nyborg [25].

2.4 Acoustic Streaming: Effects on Maximum Velocity

The streaming velocity is defined as the velocity of the fluid undergoing acoustic streaming. The maximum streaming velocity is defined as the maximum velocity of the fluid in acoustic streaming, often found in the circulatory cells of the fluid structure. Marshall and Wu [62] identified two components to acoustic streaming; A fluid velocity field consisting of an oscillating flow (U_{ac}) and a second none-oscillatory flow induced by thermal buoyancy. These components come together to form the overall streaming velocity. The importance of such a fluid system (particularly that of Figure 2.1) can be found in established research into microfluidics. Nguyen and White [70] for example studied the flexural wave propagation in a thin membrane. The micromachined device consisted of a rectangular flow channel that has a thin membrane on the bottom. Significant cooling effects were observed with wave amplitudes of $100nm$. Maximum velocity was noted to have stayed constant with a channel height that is greater than the evanescent decay length of the acoustic wave in the fluid thus they conclude that optimizing channel height only makes sense with values less than this quantity which in this case was measured to be 20 μm. Catarino et al. [14] highlighted the importance of microsystem technologies for diagnosis applications. The acoustic streaming phenomenon was successfully modelled based on the schematic of a polymeric piezoelectric transducer. Two solid trends in the sim-
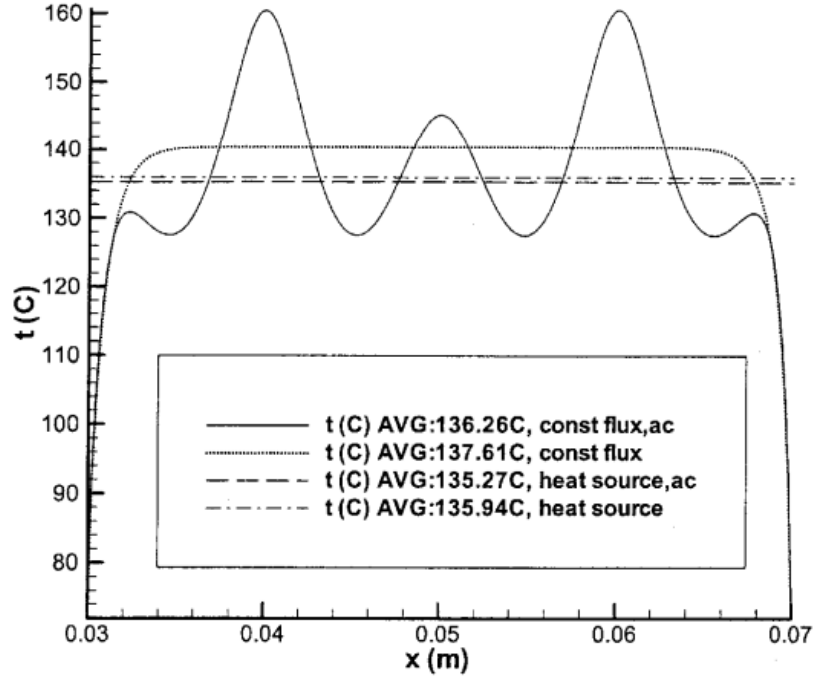
Figure 2.5: Temperature distribution across the upper beam [60].
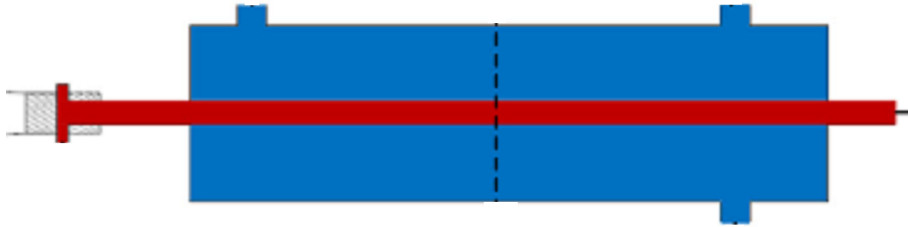
Figure 2.6: Double heat pipe exchanger schematic between hot fluid (in red) and cold fluid (in blue) [69].

ulations were found. The first, based on Eckhart streaming as outlined previously, was that amplitude decreases with distance from the acoustic source and that increasing viscosity was the primary contributing factor to acoustic attenuation. They were able to reproduce circulatory flow centred on the centre of the mivrocuvette domain. The investigation was crucial in showing that a circulatory system could be resolved in mean global flow through a set of first and second order equations. As outlined in a mathematical overview by Wiklund et al. [10], Framton, Frampton et al. [71] were able to take this one step further by looking at changes to enclosure size thus testing the validation of the fluid structure presented in Figure 2.1. By reducing the size of the fluid enclosure, the inner Schlichting streaming (within the viscous boundary layer) was confirmed to have gained prominence in relation to overall streaming but with a reduction in the combined streaming velocity. An increase in streaming velocity was also found to have resulted from an increase in
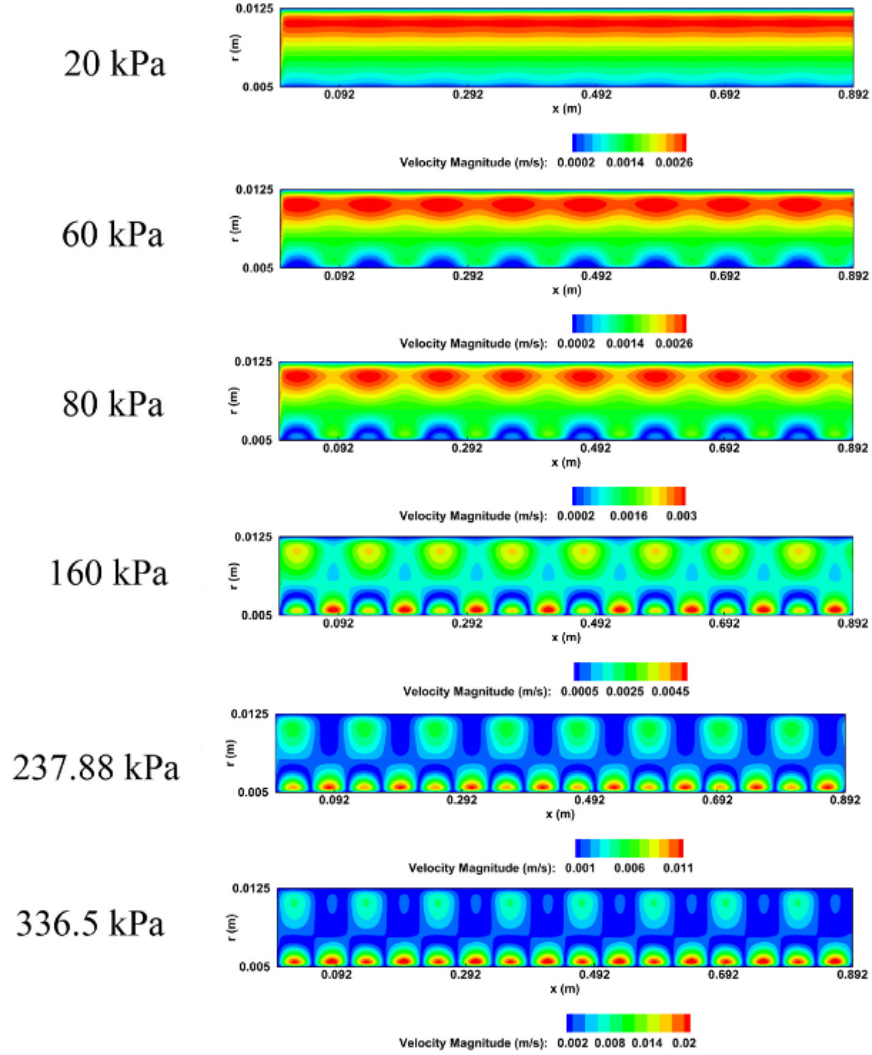
Figure 2.7: Velocity magnitude of the inner pipe [69].

acoustic frequency. Hyun et al. [72] on the other hand found the opposite, finding that the maximum streaming velocity actually decreased with increasing excitation frequency. Muller and Bruus [73] found that reducing channel height resulted in a significantly lower streaming velocity. With smaller sized channel heights, their results deviated from the single-wall analysis conducted by Rednikov and Sadhal.

Within the context of maximum streaming velocity, the literature contains numerous investigations that outline the effects of the fluid domain on such a parameter. In particular, work carried out by sajjadi et al. [74], where a reduction in volume was found to lead to a larger pressure amplitude and a subsequent net increase in average maximum velocity. Such an increase was found to result in an increase in the heat transfer coefficient. These findings also agree with that of Tajik et al. [58]. Here, CFD simulations were ran albeit without a heat source and a similar comparison made between acoustic pressures and maximum velocity. An increase in enclosure radius was also found to have led to an increase in instantaneous velocity

of the flow. Hyun et al. [72] were also able to further clarify on this area for their experimental setup, a fluid was enclosed by an upper and a lower aluminium plate. Their conclusions indicated a considerable increase in maximum acoustic velocities for corresponding increase in vibration amplitude. Mozurkewich [75] identified that Nusselt number was proportional to the square root of the Reynold's number at larger vibration amplitudes and that increasing the frequency moved the transition regime to a larger Reynold's number. Referring back to Zhang et al. [28], the importance of amplitude was also acknowledged, with a correlation having been identified between edge sharpness and vibration amplitude. sajjadi et al. [74] on the other hand, identified that increasing the amplitude of the vibrating plate reduced the maximum temperature. Again the pressure amplitude was found to play a part in this along with the gradient of the acoustic pressure. Both quantities were found to increase the instantaneous and average mass transport acoustic pressure. More importantly, by doubling the amplitude of oscillations, the heat transfer was observed to increase by 88 %.

Further work and maximum velocity was conducted by Talebi et al. [76] for a two-dimensional setup representing an enclosure filled with air. A correlation was identified between the maximum velocity and the vortex intensity which created better mixing of the fluid and thus a more adequate disturbance of the thermal boundary layer. Referring back to Setareh et al. [69], one observation from their investigation was that maximum velocity magnitude increased as acoustic pressure increased at specified Reynold's number due to the strength of near-wall circulation. The temperature distribution was also noted to have exhibited peaks and troughs as a direct result of the acoustic streaming thus identifying a way in which heat transfer was enhanced by the transfer of more heat from the hot fluid to the cold fluid.

2.5   Effects of Viscosity

Zhang [66] highlighted independence of viscosity for Rayleigh-Schlichting acoustic streaming, providing that that the size of the overall flow domain was much larger than the viscous boundary layer. For Eckhart streaming, based on such a fluid domain, Riaud et al. [77] noted the balance between attenuation and shear such that the streaming flow doesn't vanish in the limit of vanishing streaming velocity. Piercy and Lamb [78] noted that the coefficient of viscosity influences the velocity of streaming only through its relationship to the coefficient of sound absorption. They found that measurements of streaming velocity did not yield information about the coefficient of viscosity other than from direct measurements of sound absorption. Bruus [79] highlighted the fact that streaming in an Eckhart regime is primarily driven by bulk absorption and not boundary layer stresses and therefore any Direct Numerical Methods to resolve these stresses would results in unnecessary computational memory costs. Therefore the effects of viscosity have long been ignored in acoustic experimentation.

A study does however exist for an investigation into the influences of sharp edged geometries on acoustic streaming by Zhang [66] who found that viscosity did in fact

have a consierable effect on the behaviour. The domain in question represented a
microchannel with length and width respectivly of 1.5 mm and 0.5 mm. Figure 2.8
shows this in detail.
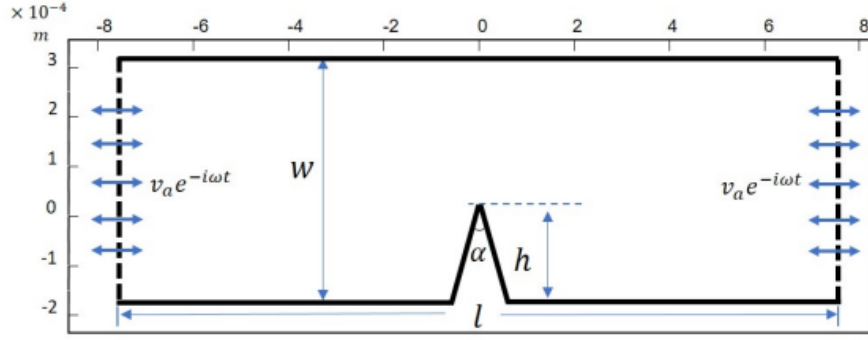
Figure 2.8: Geometry of the domain of study from Zhang [66].

Within their work they defined a quantity θ that represented a fitting coefficient
between the streaming velocity and the acoustic vibration velocity. This quantity θ
was seen to decrease with viscosity along a log-law axis (Figure 2.9). r_c is the radius
of curviture of the tip.
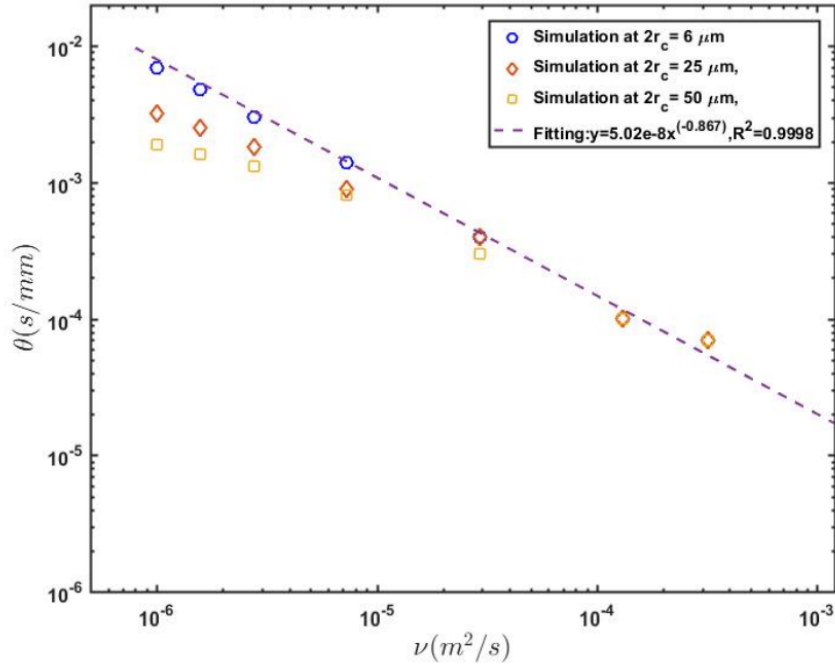
Figure 2.9: Coefficient θ versus kinematic viscosity ν from Zhang [66].

It was found that the the influence of the sharp edge was significant for the extent
that acoustic streaming was effected by viscosity. For example for $2r_c = 25~\mu m$ and
$2r_c = 50~\mu m$, it was found that the decrease of θ was less prominent compared to

higher values and θ dependence was not captured by the power law. On the other hand, for high viscosity ranges, θ was found to be independent of r_c (when $2r_c/\delta$).

2.6 Biomedical Applications

As well as the effects identified in Section 4.5 on fluid structures, ultrasound has been documented for its very well-known uses in medicine. It is non-invasive to animal tissue due to its none-ionising nature thus at high frequencies in the scale of megahertz can perform non-invasive functions in contrast to surgery, such as heating, tissue ablation, and clot dissolution. High Focused Ultrasound (HIFU) is currently being investigated for modifying or destroying diseased tissues inside the body such as tumours without the need to make any incisions in the outer skin. Diagnostic ultrasounds find its uses in the most well-known area of image generation where beams of sound waves are reflected back from their respective transducer by tissue boundaries to generate electric signals that are sent to the ultrasound scanner. More recently, publications in microfluidics have shown considerable interest in the use of ultrasonically induced acoustic streaming for micro-machined flexural plate wave devices. This has further enhanced the already extensive research into ultrasonic research by contributing to applications in fluid pumping in microbiology and micro-chemical analysis along with aforementioned medical applications in areas such ablation and further still, to cleaning, and endontics. Within the biomedical category, the research undertaken has had an impact on all medical areas such as ablation, cleaning and oncology. Zhang et al. [80] obtained positive results from Histotripsy, a non-invasive therapeutic technique that uses ultrasound to induce controlled cavitation of a specifically targeted tissue. 14 pigs received treatment for Thrombosis. This is presented in Figure 2.10
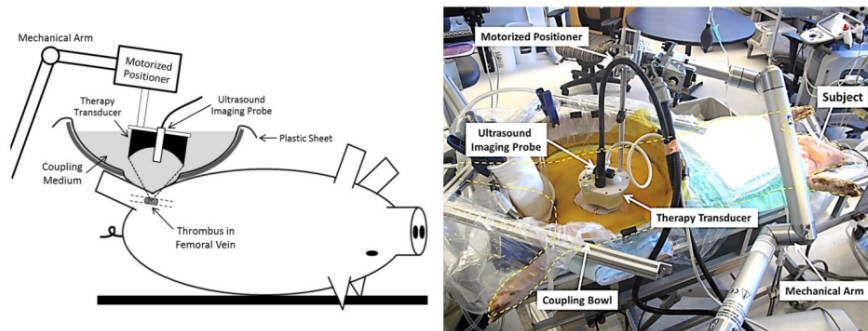
Figure 2.10: Schematic experimental setup (Left) and a picture of the actual setup during one thrombolysis treatment (Right) [80].

The flow channels were found to have successfully reopened for 13 out of the 14 pigs with blood vessel diameter increasing up to 64%. Seo and Kim [81] highlighted the importance of said cavitation for tissue treatment in their review of the most recent advances of ultrasound. They adequately summarised the general trajectory of ultrasonic research in this area, however of particular note is their outline of the fundamental physics behind how cavitation not only induces tissue ablation, but

also assists in the vital medical process of spatially targeted drug delivery. An explanation is given, that with the time varying nature of the acoustic pressure field resulting from its propagation comes the rapid formation and collapse of microbubbles. If this cavitation activity occurs near a biological boundary, then the barrier function of that boundary is temporally disrupted thus allowing for drug delivery through the disturbed boundary. A further review Yu et al. [82] was conducted on the most recent advances in low-level ultrasonic research for cancer therapy. The review provides information on the various bio effects of ultrasound. They are frequency and intensity dependant with high intensity benefiting heat production and a lower frequency favouring the occurrence of cavitation.

Solovchuk et al. [83] investigated further targeted tissue techniques. They studied the influence of blood vessels on temperature distribution during high-intensity focused ultrasound propagation of a liver tumour. Here, a computational model was validated using experimental results produced by Huang et al. [84] as demonstrated in Figure 2.11
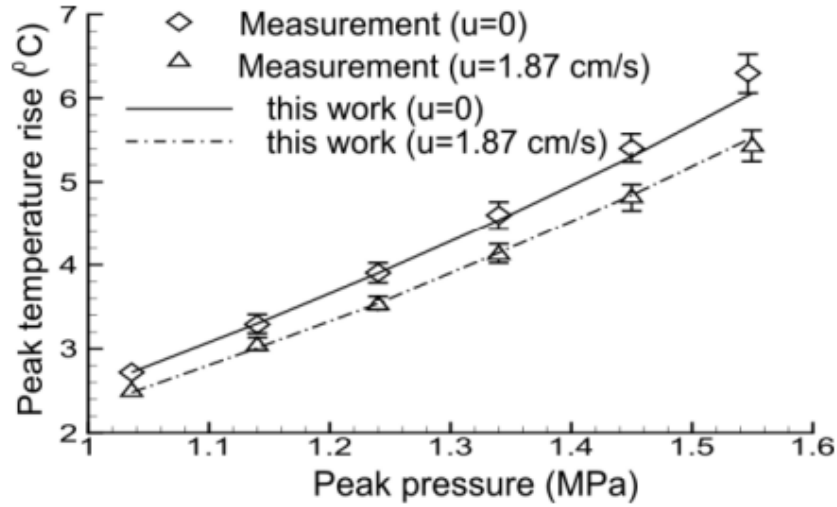
Figure 2.11: Validation of the computational model from Solovchuk et al. [83] with Huang et al. [84]

.

They found that convective cooling effects in large blood vessels was enhanced by the effects of acoustic streaming. The temperature rise was subsequently reduced at the surfaces of large blood vessels as demonstrated in Figure 2.12 thus giving rise to more enhanced effects on reducing lesion size and shape.

Wessapan and Rattanadecho [85] carried out a further ablative study. Again, a numerical investigation was conducted in which a conventional bioheat based heat transfer model was compared to a porous media based heat transfer model. The bioheat model used was The Pennes' model [86] and is one of the earliest to be compiled for the standard modelling of biological tissue due to its simplicity and minimal data requirements as shown in Figure 2.13.
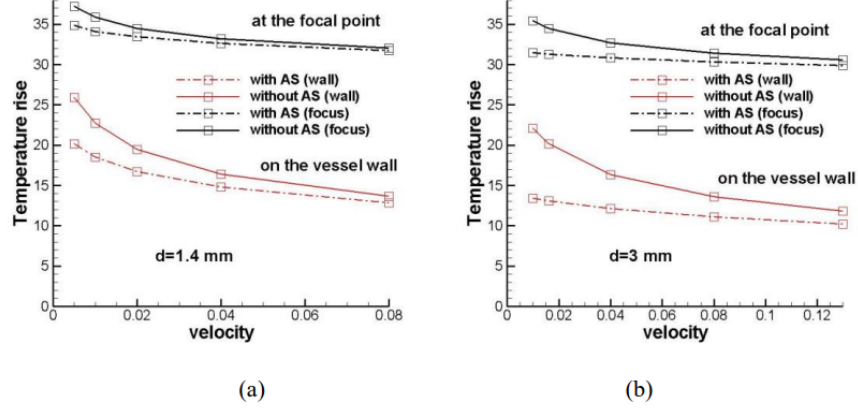
Figure 2.12: The predicted temperatures as the function of inlet average velocity (m/s) for the cases with and without acoustic streaming effect at the focal point and on the blood vessel wall (d/2, 0, 0.12), t = 8 s, gap=0.5 mm. (a) d=1.4 mm; (b) d=3 mm [84] .

For this model,Penn measured tissues and brachial arterial blood to evaluate the applicability of heat flow theory in terms of local rate of tissue heat production and volume flow of blood thus determining a cutaneous topography of temperature in the upper extremity for a forearm. This allowed Wessapan and Rattanadecho [85] to consider heat transport through the tissue through heat conduction, blood perfusion and metabolic heat generation. Heat transfer characteristics of the tissue were based on the classical Fourier's law. The porous media model was a standardised tissue model that took into account the effects of heat transfer, tissue permeability and exposure time on fluid flow and temperature distribution with the porous medium specifically representing a fluid-saturated tissue. It was coupled with an acoustic wave pressure equation that describes the acoustic propagation characteristics in any medium. The study was unique in that it was one of the few investigations to take into account tissue permeability. Like Solovchuk et al. [83], comparisons were made with Huang et al. [84]. In particular, good agreement was obtained for cooling over a period of 5 seconds (in which the temperature increase was measured at every half second) as presented in Figure 2.14.

Overall instantaneous temperature distributions were found to be different however with the peak temperature from the porous media model found to be slightly lower than that of the conventional bio heat model. This was attributed to the acoustic aspects of the model, which induced a dominant acoustic streaming flow at a higher temperature gradient thus decreasing heat accumulation in the high-temperature region.

A review carried out by Mozo et al. [87] summarises the most recent findings in the use of ultrasonic instrumentation for endontics. They concluded that the use of ultrasound results in improved canal cleanliness, better irragant transfer to the canal system, soft tissue debridement and removal of smear layer and bacteria. Overall,

29
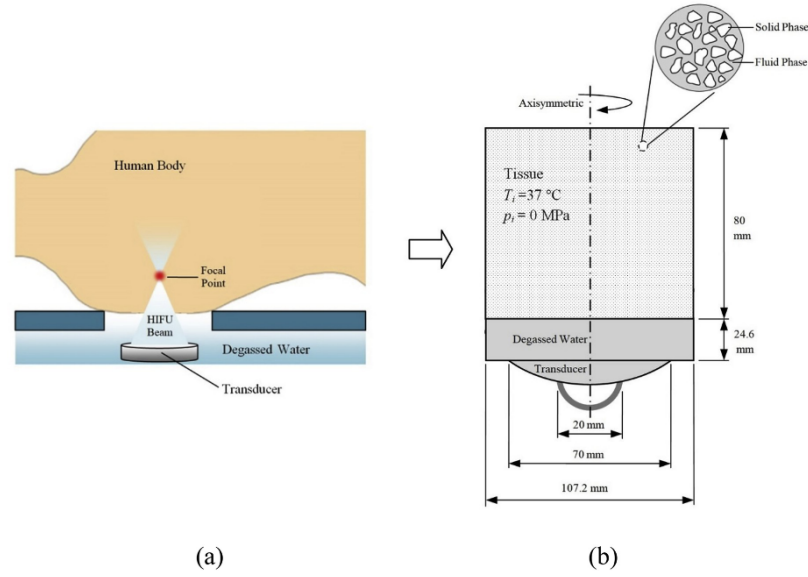
Figure 2.13: Physical model of the problem from Wessapan and Rattanadecho [85]: (a) Schematic diagram of HIFU treatment, (b) Model details.

treatment quality was found to improve in several aspects; access to root canal entry holes, cleaning, shaping and filling canals, eliminating obstructions and intra-canal materials and endontic surgery. The review also highlighted the importance of acoustic streaming in the continuous movement of irrigant fluid around the root canal to enhance cleaning. Verhaagen et al. [88] investigated the use of acoustic streaming in a two-dimensional representation of a root canal for endodontic cleaning as demonstrated in Figure 2.15.

In both their numerical and experimental investigations the presence of an oscillatory component was confirmed near the file and a steady component further away, seen in Figure 2.16 thus being in agreement with Marshall and Wu [62].

2.7 Acoustic Streaming applications for Industrial Cleaning

The role of megasonics in the semiconductor industry is of particular importance. Particle residue is of major concern in integrated circuits and therefore limits the product performance and manufacturing of semiconductors [89]. Thanu et al. [90] noted that particle contamination is a major form of yield loss in the fabrication of integrated circuits. The size of these devices means any nanosized contaminants in small scaled devices such as these means a considerable degradation in performance. Acoustic Streaming has been demonstrated to contribute to particle removal in sonic baths. The reduction in the substrate boundary layer thickness and the resulting large velocity gradients and viscous stresses thus aiding in the removal of surface contaminants according to Gale and Busnaina [91]. Busnaina and Elsawy [92] obtained results for the removal of silica slurry using megasonic cleaning. They found that the higher the peak pressures associated with acoustic streaming, the
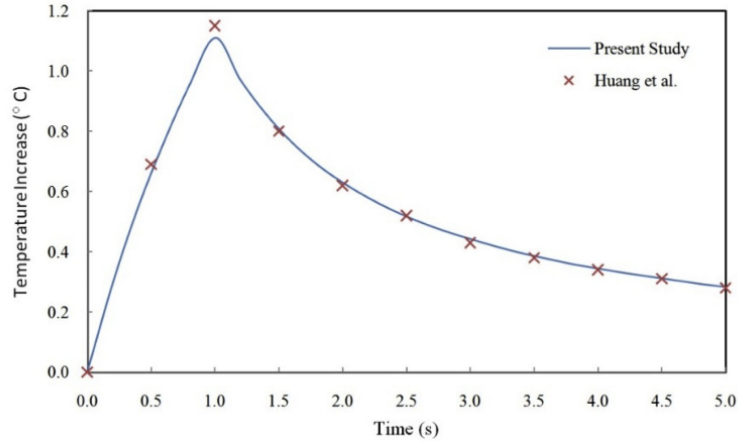
Figure 2.14: Comparison between temperature increase-time profiles obtained from this numerical study and obtained by Huang et al. [84].

most effective the particle removal. In particular, they identified optimum acoustic streaming conditions to achieve the most effective slurry removal. These were a power outage of 400 to $500W$, a water temperature of 30 to 35^oC and a time of 13 to 17 minutes. It was also noted that different removal efficiencies were exbhibited for different compounds. Examples included polystyrene latex, silica and silican nitride particles. [93]. Chun-Lin and Te-Yun L. [89] also identified megasonic cleaning through acoustic streaming was fast becoming an efficient method of cleaning noting an optimum temperature of 60^oC for a particle solution of an Ammonium Hydroxide solution. Surface cleaning of a solid substrate by a 20 MhZ acoustic wave was demonstrated by Yifan et al. [94] where they were actually able to redirect the deposition of precipiate impurity mass into a nearby inert substrate as demonstrated in Figure 2.17. The substances in question were polymethl methacrylate for its respective precipitate on the adjacent lithium niobate.

They noticed an increase in the deposition of precipitate with application of acoustic waves compared to without. Kapila et al. [95] highlighted further importance of acoustic streaming and megasonic cleaning for photomasks, also involving the removal of contaminant particles in appllications for EUV lithography,a technology used in machine fabricators for aforementioned integrated circuits. In their investigation, they used a continuum model to determine the interaction between megasonic waves and a substrate. They were able to determine the acoustic forces from the resulting formation of Schlichting streaming in a narrow acoustic boundary layer at the substrate-fluid interface. It was found that the resulting drag forces resulting from Schlichting steaming gave rise to sufficiently strong drag forces. These drag forces then induced rolling moments which were found to subsequently enhance the removal of particles via sliding and rolling mechanisms. Bakhtari et al. [96] further elaborates on this, going into detail about how it was found that once a nanoparticle was detached from the respective substrate, it undergoes oscillatory motion which and redeposition which results in an increased amount of time for full particle removal. It was noted that a this time was lower (at 4 minutes) for deionised
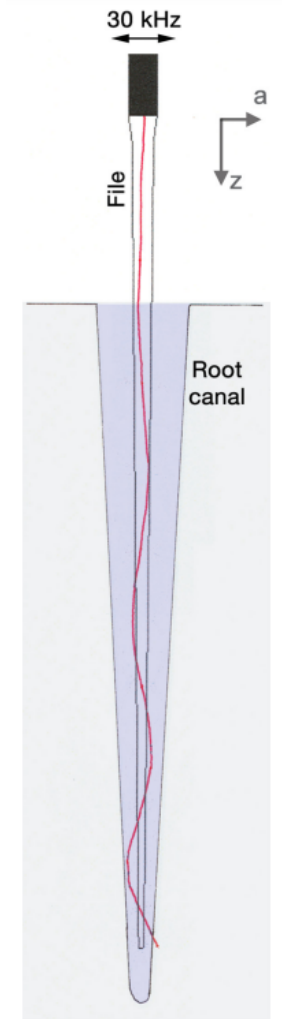
Figure 2.15: Sketch of a file oscillating inside a (much simplified) root canal. The solid line indicates a typical oscillation pattern, exaggerated in amplitude [88].

water compared to ionised water (at 6 minutes). He provides a detailed schematic (Figure 2.18) of the forces and moments on a particle from acoustic streaming flow. In this case δ is the particles deformation height. a is the contact radius between the deformed particle and the surface. R is the sphereical radius of the particle. $F_{elec.doublelayer}$ is the double layer force resulting from an equal and oppositely charged layer in the adjacent liquid that balances the charge of the immerged subtrate on the surface. $F_{adhesion}$ is the combination of the Van der Waal and the electrostatic adhesion forces. The smaller the particle, the harder these forces are to overcome.

2.8 Flow Physics and Control

Chapter 2 introduces the importance of acoustic streaming for its cooling effects and literature from researchers such as Trujillo [15]. In particular, Guo and Sun [65] provide a detailed overview of how acoustic streaming induces cooling. Figure 2.19
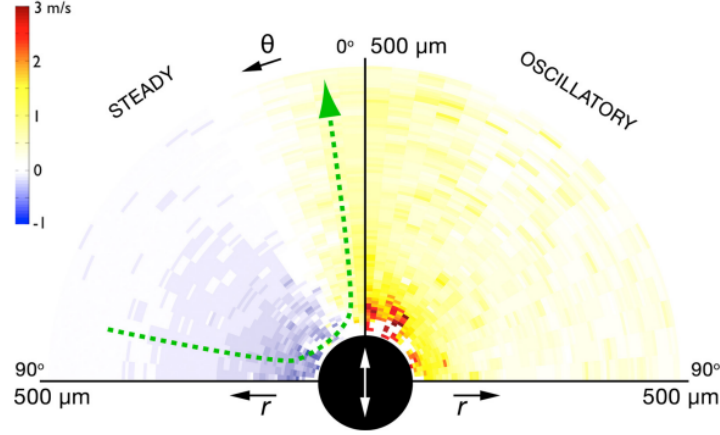
Figure 2.16:) Steady (left) and oscillatory (right) components of the measured radial flow velocities around an oscillating endodontic file, averaged over three measurements. A typical steady particle trajectory is indicated with a green arrow [88].

presents a schematic of a microfluidic device, an example where acoustic streaming is utilized in microelectronics to enhance the cooling of high-power consuming systems.

The device consists of a microchannel and a microcavity and is filled with water. A piezeo-electric (PZT) plate is placed at the bottom. When an AC voltage is applied across this plate, an acoustic field is generated and induces convection currents in the fluid inside the device. These currents disrupt any resulting thermal boundary layers from a heat source and essentially carry the heat away from the heat source with a constant rate of internal energy generation. A cross section of this system is provided in Figure 2.20 to show this in detail.

Heat flux and vibration conditions are applied to the upper and lower wall of the microchannel as indicated by $q^{"}$.

Rahimi et al. [97]] highlight its importance in industrial processes such as mixing and yield optimization through its improved effects on breaking chemical bonds. Trujillo [15] were able to obtain good agreement between experimental and computational results. Both Trujillo [15] and Rahimi et al. [97] used specific mathematical approximations to predict the velocity profile on their respective horn tip inlets. Trujillo made comparisons between two approaches. The Gaussian jet velocity distribution as provided by Lighthill [12] where velocity is calculated using:

$$u = \left[\frac{2K}{\pi S^2}\right]^{\frac{1}{2}} e^{\left[-\frac{r}{S}\right]} \tag{2.10}$$

and Schlichtings Turbulent circular jet solution [98] was used to estimate the velocity profile:

$$u = \frac{1}{4}\sqrt{\frac{3}{\pi}}\frac{\sqrt{K}}{x}\frac{\eta - \frac{1}{4}\eta^3}{\left[\eta + \frac{1}{4}\eta^2\right]} \tag{2.11}$$
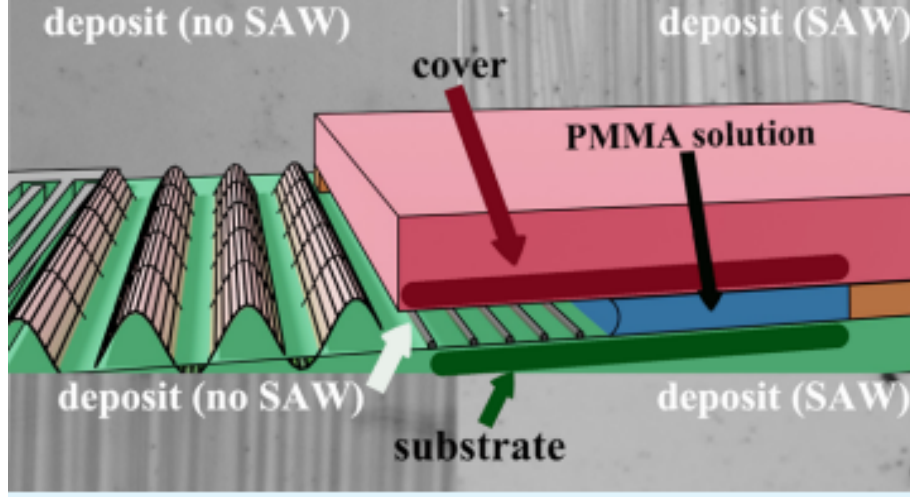
Figure 2.17: Detailed setup for Precipitate Disposition from Yifan et al. [94].

Noting that $\eta = \frac{1}{4}\sqrt{\frac{3}{\pi}}\frac{\sqrt{K}}{\mu_t}\frac{r}{x}$, both distributions satisfy the conservation of momentum

$$\rho \int_0^\infty u^2 2\pi dr = F_N \qquad (2.12)$$

Both models showed good agreement with the experimental results. Trujillo however highlighted that Lighthill's Gaussian distribution approach would be the preferred method from a theoretical point of view as its utilization can be extended to cases of lower "effective" attenuation where sound rays should be followed from the source to calculate its intensity attenuation and subsequent increase of kinetic momentum K and turbulent viscosity.

Rahimi et al. [97] modelled the displacement of the horn tip using a sinusoidal movement with a periodic frequency f with an expression that was a function of both time and position (r) using the radius (R). Differentiating Equation 2.13 gave a velocity magnitude and radiating surface of the ultrasonic horn reactor (UHR):

$$\xi(r,t) = \xi_{max}\left[1 - \left[\frac{r}{R}\right]^2 + 2\left[\frac{r}{R}\right]^2 \ln\frac{r+\delta}{R}\right]\sin(2\pi ft) \qquad (2.13)$$

$$u_{UHR}(r,t) = \xi_{max}2\pi f\left[1 - \left[\frac{r}{R}\right]^2 + 2\left[\frac{r}{R}\right]^2 \ln\frac{r+\delta}{R}\right]\cos(2\pi ft) \qquad (2.14)$$

Good agreement was obtained with experimental PIV data. Figure 2.22 provides an example of this for an axial velocity distribution for different heights from the horn tip.

Within the acoustic jet, it was found that the average velocity magnitude of the injected tracer below the horn tip, at the axis pivot was greater than the velocity at the line 3 mm from the axis pivot for all power inputs as shown in Figure 2.22(Top) for reference.
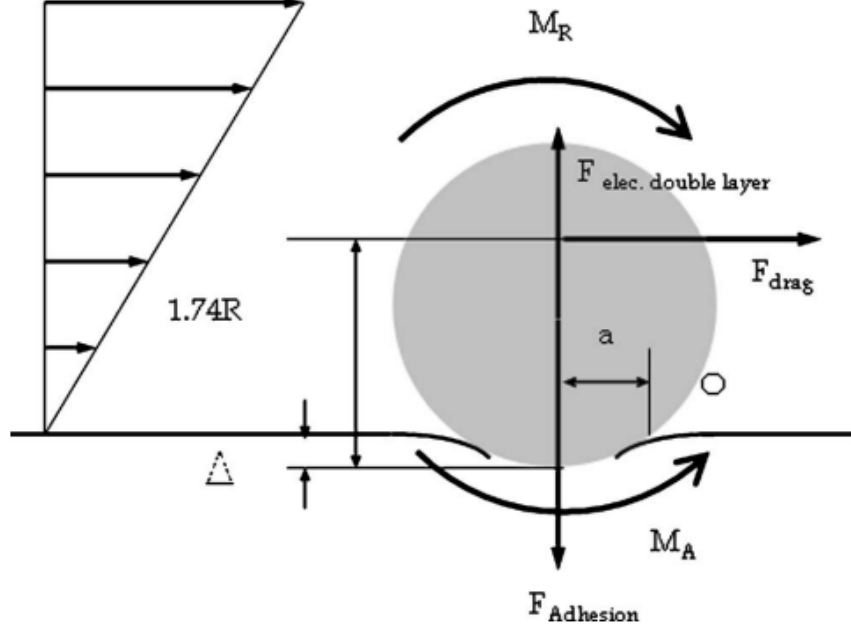
Figure 2.18: Forces and moment on a particle from acoustic streaming [96].

Further work on jets was carried out by Moudjed et al. [99] through the derivation of the governing equations under the form of a nonlinear hydrodynamics problem coupled with an acoustic propagation problem based on a timescale discrimination approach. This involved splitting each variable into an acoustic component that varied rapidly and a streaming motion component, which varied slowly in comparison. The example is one of many where the flow components are split into oscillatory and none-oscillatory constituents and form the basis for the methodology outlined in Section 3. The example is as follows; the variable decomposition are subsequently introduced into the Navier-Stokes equations and their averages computed over one period of time. Linear terms will therefore disappear when they are reconstituted with an acoustic variable or will be substituted with an instantaneous value when they feature a streaming flow variable. The Navier-Stokes therefore become:

$$\frac{\partial \rho_s}{\partial t} + \nabla \cdot (\overline{\rho_{ac}\vec{u}_s}) + \nabla \cdot (\rho_s \vec{u}_s) = 0 \tag{2.15}$$

$$\rho_s \frac{d\bar{u}_s}{dt} = -\vec{\nabla} p_s + \nabla^2 \vec{u}_s + (\eta + \mu)\vec{\nabla}(\nabla \cdot \vec{u}_s) + \vec{f}_{ac} \tag{2.16}$$

with subscript ac denoting the acoustic component and s denoting the streaming component. η represents the bulk velocity and μ in this case represented the dynamic viscosity. The last term in the above equation $\vec{f}_{ac}$ represents the acoustic streaming force term whose ith component in a Cartesian work-frame is:

$$\vec{f}_{ac,i} = \nabla \cdot (\overline{\rho_{ac}\vec{u}_{s,i}\vec{u}_{ac}} + \overline{\rho_{ac}u_{ac,i}\vec{u}_s} + \overline{\rho_{ac}u_{ac,i}\vec{u}_{ac}} + \overline{\rho u_{ac}u_{ac,i}\vec{u}_{ac}}) \tag{2.17}$$
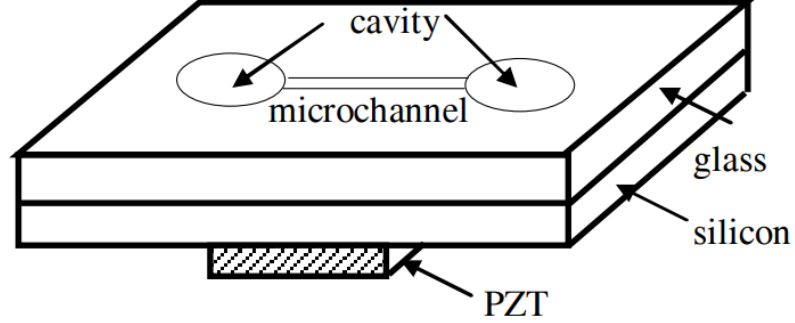
Figure 2.19: Microfluic device for cooling [65].
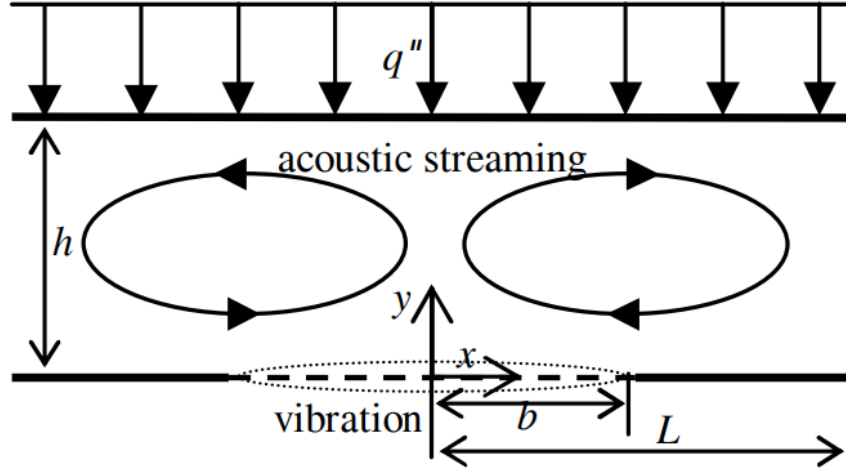
Figure 2.20: Cross-section of microchannel [65].

$i = 1, 2$ or 3

Assuming that terms proportional to ρ_{ac} can be neglected with respect to terms proportional to ρ_s, along with considering that the obtained streaming flow velocities are always far smaller than the sound velocity therefore allowing for the fluid to be considered low Mach and incompressible (thus neglecting time and space variations of ρ_s), the set of equations become:

$$f_{ac,i} = -\rho_s \nabla \cdot \left(\overline{u_{ac,i}\vec{u}_{ac}}\right) \tag{2.18}$$

$$\nabla \cdot \vec{u}_s = 0 \tag{2.19}$$

$$\rho_s \frac{d\vec{u}_s}{dt} = -\vec{\nabla} p_s + \mu \nabla^2 \vec{u}_s + \vec{f}_{ac} \tag{2.20}$$

Moudjed et al. [99] also made velocity comparisons using a plane transducer in water, investigating the shape of the acoustic field in relation to the velocity
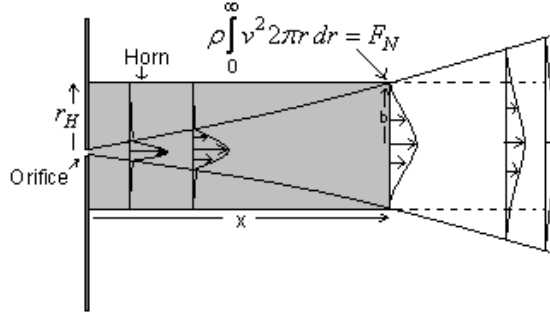
Figure 2.21: A Schematic diagram of jet flow velocity profile superimposed in the horn from Trujillo [15].

field. They highlighted that diffraction was a key factor in the problem, which generally had not been accounted for in previous literature and that small acoustic powers can yield relatively high Reynold's numbers and velocity levels. Although full similarity between two experiments of different fluids was not possible. Consequentially, they conducted a scaling analysis, leading to two scaling laws for the typical velocity level in acoustic streaming free jets. For these two laws, a steady laminar acoustic streaming jet in a semi-infinite medium was considered. The first being an inertia dominated regime near the origin of the jet and the second being a viscosity-dominated regime far from the origin of the jet.

For the inertia dominated regime, balancing the inertial terms and the acoustic force results in the following relation for a typical velocity u at a distance x from the origin of the jet with acoustic beam radius R_{beam} and acoustic power P_{ac}:

$$u \propto \sqrt{\frac{2\alpha}{\rho c} \frac{P_{ac}}{\pi R_{beam}^2} x} \qquad (2.21)$$

For the inertia dominated regime, balancing the inertial terms and the acoustic force results in the following relation for a typical velocity u at a distance x from the origin of the jet with acoustic beam radius R_{beam} and acoustic power P_{ac}:

$$u \propto 2\frac{\alpha P_{ac}}{\pi \mu c} \qquad (2.22)$$

Using the radial enlargement law for a laminar jet by viscous diffusion with δ being some scale factor, which is in the form of a scaling law $\frac{\delta R_{diffraction}}{x} = \sqrt{\frac{v}{u(x)x} + Re_x^{-1/2}}$, a relation can be obtained which finds the distance beyond which the jet is governed by diffraction:

$$\frac{x_{lim}}{L_f} = \frac{8\pi}{1.22^2} \frac{\mu^2 f}{\alpha \rho P_{ac}} \qquad (2.23)$$

x in this case is the distance from the origin of the jet, taken as the distance from the upstream in the experiment.
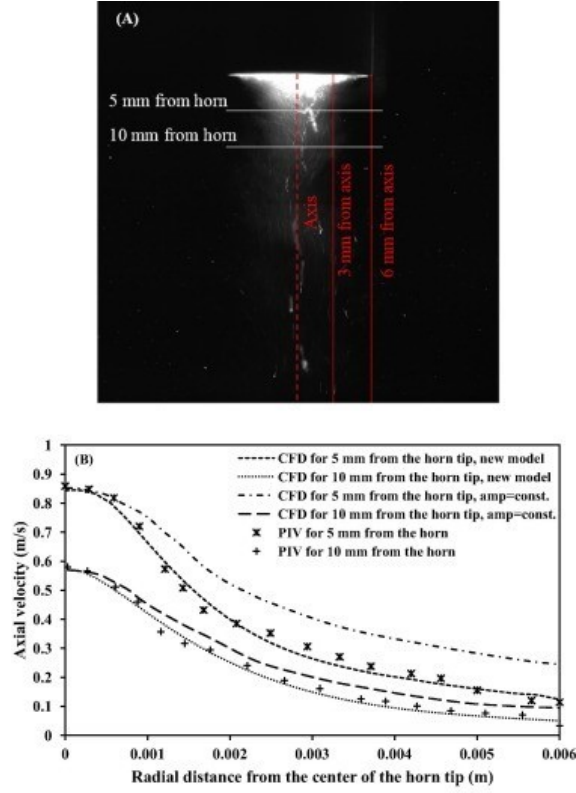
Figure 2.22: (Top) photographic image of the jet induced below the horn tip and (Bottom) axial velocity magnitude distribution below the horn tip to the bottom wall for 40 mm and flow time = 0.588 s from Rahimi et al. [97].

It is clear that the increasing acoustic power leads to a decrease in x_{lim}. Therefore, the above expression gives a significant indication of the size and length of the domain investigation from the order magnitude provided by Equation (2.23)

Eisener et al. [100] made streaming velocity measurements of an emerging jet flow subject to acoustic propagation beyond 100 MHz. At such high frequencies it was found that the dissipation length of the acoustic waves shrank considerably. The Eckart streaming fluid structure as elaborated in Section 2.3. Breaks down and the first example in the literature of Stuart-Lighthill streaming is observed. Recall that the momentum transfer along the path of propagation of a weakly damped travelling sound wave fundamentally drives Eckhart streaming and the momentum transfer of a highly damped but rapidly decaying wave drives Stuart-Lighthill. In this case the acoustic streaming effects were characterised by ink front tracking and particle tracking velocimetry.

2.9 Heat Transfer Applications

Within engineering applications, Wan and Kuznetsov [60] mentioned previously, highlighted how their experimental setup could be applied to the cooling of computer chips thus stressing the importance of understanding the fluid dynamics in

thermoacoustic devices. Such a device is studied by Bailliet et al. [101]. He was able to derive analytical expressions for the time-independent second-order velocity, pressure gradient and time-averaged mass flux for a fluid subject to a temperature gradient and confined between two parallel solid boundaries. Firstly, it was concluded that amplitude played a significant role in the strength of streaming, with an increase in streaming showing a corresponding increase in second-order velocity. It was also shown that the expression for second order particle velocity is less significant for small ratios of radius (distance from the center-line to the solid boundary) to displacement thickness of the stokes boundary layer as shown in Figure 2.1 for reference. The behaviour of streaming in this investigation is significant to the streaming criteria mentioned in section . . . on the structure of acoustic streaming as outlined in Figure 2.1 . It was found that the calculation of streaming in the device built at the National Center of Physical Acoustics did not give comparable results to those of the experimental, thus indicating that the large steady component of the measured particle velocity in this case was not due to Rayleigh streaming as outlined in Figure 2.1. Penelet et al. [102] highlighted additional applications for micro-mechanical systems, emphasising that the ability to demonstrate acoustic streaming in devices like micro-pumps or micro-mixers would have important applications for heat extraction in electronic components. In their investigation they also conducted studies of the nonlinear effects of surface acoustic waves on heat transport through a microchannel, specifically on a solid-fluid interface. Three distinct mechanisms of heat transfer were estimated analytically based on a simple geometry representation of a fluid-solid interface as presented in Figure 2.23:
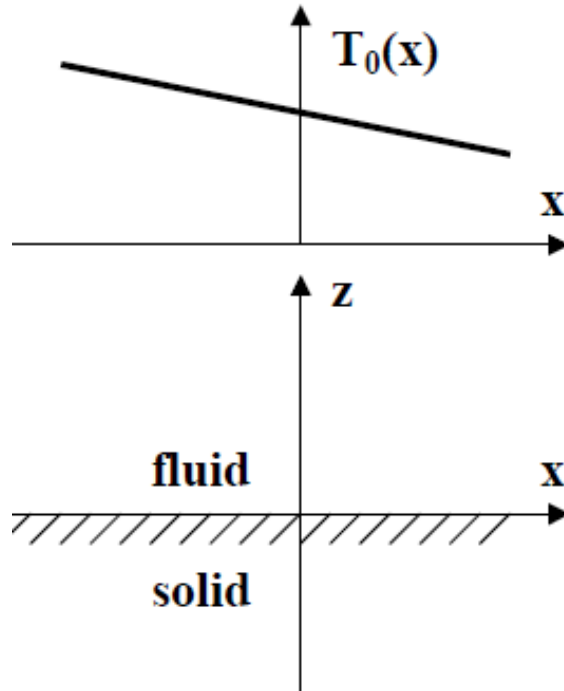
Figure 2.23: Schematic representation of the problem presented by Penelet et al. [102].

The geometry is subject to a longitudinal temperature gradient where 1st-order oscillations in the z-direction give rise to 2nd-order none-oscillating heat flux. The first of the three mechanisms considered was steady streaming due to dependence of viscosity on temperature as seen in Figure 2.24. In this case, excitation's of vibrations induce oscillation of fluid in the viscous boundary layer due to mean temperature variations. This subsequently leads to a second order mean flow in the fluid. They derived a second order velocity of steady streaming in the form seen in Figure 2.24.
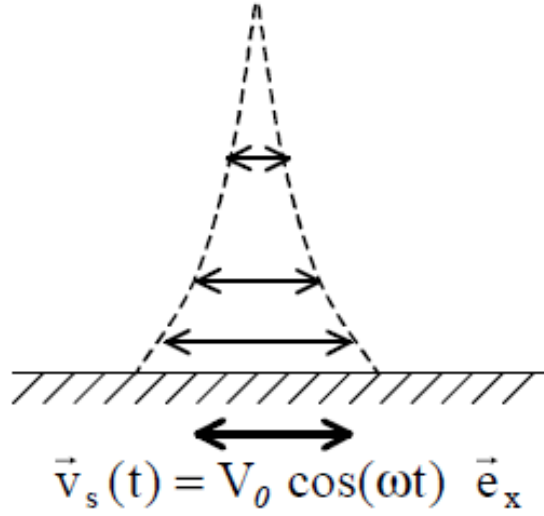
Figure 2.24: Schematic representation of vibration of the solid along the x axis which drives a second order mean flow with heat flux due to dependence of viscosity on temperature [102].

In this case, excitations of vibrations induce oscillation of fluid in the viscous boundary layer due to mean temperature variations. This subsequently leads to a second order mean flow in the fluid. They derived a second order velocity of steady streaming in the form:

$$\epsilon^2 \langle u_2 \rangle = \epsilon d_x \eta_1 \frac{V_0^2}{4\eta_0 \omega} e^{-2k_0 x}(e^{k_0 z} cos(k_0 z) - k_0 z - 1) \tag{2.24}$$

where ϵ^2 denotes the 2nd order component of velocity. η is the shear viscosity and k is denoted by $k = [\frac{\omega}{2v}]^{\frac{1}{2}}$ with kinematic viscosity v represented by $\frac{\eta}{\rho_0}$. Note as per the convention in this thesis, the subscript 0 denotes the zeroth order of the respective quantity.

Based on this relation, the streaming velocity reaches its maximum at an approximate distance of $2\delta_{v0}$ where $\delta_{v0} = k_0^{-1}$ denotes the viscous boundary layer thickness and rapidly decreases far from the solid wall.

The second mechanism is Thermo-acoustic heat pumping in the vicinity of the solid wall resulting from the interaction between acoustic and thermal waves in the vicinity of the solid-fluid interface as shown in Figure 2.25.
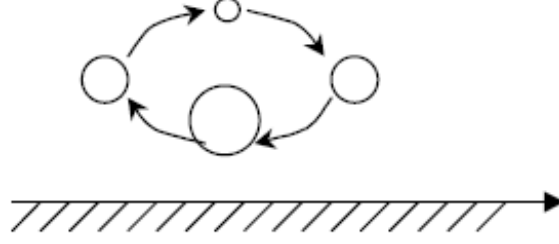
Figure 2.25: Schematic representation of the propagation of a plane acoustic wave in the fluid, giving rise to thermo-acoustic heat transport in the vicinity of the wall [102].

Temperature fluctuations results from the oscillation of the far-field fluid at a specific acoustic frequency. This is due to both adiabatic compression and expansion accompanying acoustic pressure fluctuations and the local initial temperature T_0. However a time delay occurs from the thermal contact between the oscillating fluid and the solid. The results is a none-zero time-averaged heat flux. The well documented effect can be attributed to fundamental linear acoustic theory [103]. From both the momentum conservation and heat transfer equations, the amplitude of the acoustic wave velocity $\tilde{u}_1(x, z)$ along with that of the temperature $\tilde{T}_1(x, z)$ oscillations are obtained. They are then substituted into the 2nd order time averaged thermo-acoustic heat flux along x per unit area given by:

$$\langle q_2 \rangle = \frac{1}{2}\rho_0 T_0 Re(\tilde{T}_1 \tilde{u}_1^*) - \frac{1}{2}T_0\beta Re(\tilde{p}_1 \tilde{u}_1^*) \tag{2.25}$$

$*$ denotes the complex conjugate and β represents the thermal expansion coefficient of fluid. After substitution, the resulting linear heat flux $\langle Q_2 \rangle$ is calculated from $\langle Q_2 \rangle = \int_0^\infty \langle q_2 \rangle .dz$ which becomes:

$$\langle Q_2 \rangle = -\frac{\delta_k}{4}\frac{1}{1+\sigma}\frac{|\tilde{P}_1|^2}{\rho_0 c_0}\left\{(1 - \sqrt{\sigma})T_0\beta + \frac{C_p}{\omega c_0}\frac{1 + \sqrt{\sigma} + \sigma}{1 + \sqrt{\sigma}}d_x T_0\right\} \tag{2.26}$$

σ and C_p are the Prandtl number and isobaric heat capacity per unit mass of fluid.

The final mechanism is steady streaming due to oscillating boundaries where none-linear effects in the fluid flow are caused by the propagation of travelling surface waves in the solid in the presence of a mean temperature gradient. For their analytical description of this mechanism, Penelet et al. [102] simplified the case to assume small vibration amplitudes, no temperature gradients, an incompressible fluid and purely transverse oscillations of boundaries as shown in Figure 2.26. Boundary conditions due to vibrating wall are denoted by:

$$\vec{v}(x, z = \epsilon k^{-1}\cos\omega t - kx, t) = (0 - \epsilon k^{-1}\sin(\omega t - kx)) \tag{2.27}$$

Scaling this expression for convenience, length (by k^{-1}), time (by ω^{-1}) and velocities (by $\epsilon\omega k^{-1}$) along with pressure (by $\epsilon\eta\omega$) and defining the non-dimensional parameter

$$\vec{v}_s(x,t) = \varepsilon \frac{\omega}{k} \sin(\omega t - kx) \, \vec{e}_z$$
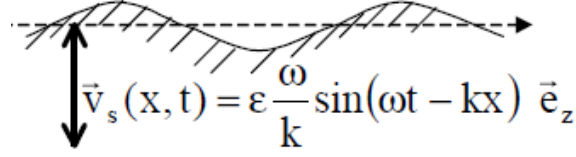
Figure 2.26: Schematic representation of transverse oscillations propagating along x-axis on the interface which leads to 2nd-order streaming in the fluid [102].

α by $\alpha^2 = \rho_0 \omega \eta^{-1} k^{-2}$. The third is the steady streaming due to oscillating boundaries where the propagation of a travelling surface wave leads to a mean fluid flow through nonlinear effects. This takes place in the presence of a mean temperature gradient.

Lebon et al. [104], who conducted a numerical study into the effects of acoustic streaming on direct-chill casting found that acoustic streaming resulted in greater grain refinement. This was attributed to the stronger streaming velocities, deeper penetration into the slurry region- thus facilitating fragmentation and transport of fragments- and the higher cooling rates which facilitate structure refinement. Yamamoto et al. [105] conducted a similar study of the ultrasonic treatment of molten metals. They noted that the stronger ultrasonic attenuation was found in in an aluminium melt compared to water. This resulted in steeper ultrasonic pressure gradients just below the sonotrode tip and therefore a more intense induction of acoustic streaming although acoustic streaming velocities for both mediums were the same. Similar findings were also made for amplitude. They found that increasing the amplitude resulted in next to no change in frequency and therefore velocity, thus establishing the streaming velocity's independence from amplitude. They attributed this to the effects of cavitation bubble shielding due to the large amplitude of the sonotrode oscillations. This results in a rapid attenuation in ultrasound pressure in the immediate vicinity of the sonotrode trip. The ultrasonic pressure distribution then becomes independent of the oscillation amplitude. The design of sono-chemical reactors has historically encountered numerous problems due to the lack of understanding of fluid structures and the distribution conditions of ultrasonic waves. Parvizian et al. [106] studied the mixing rate in a sonoreactor using 1.7 MHz waves. Four piezoelectric transducers were used. Two were placed along the reactor length, and the other two on the sides. Recall that it was discussed that Frampton et al. [71] found that an increase in acoustic frequency resulted from an increase in streaming velocity. In this case however, it was found that the mere addition of forced convection from acoustic streaming were actually reduced. A postulation was therefore made that separate steaming structures created by transducers on opposing sides weakened each other by effectively cancelling each other out.

2.10 Modelling Approaches to Acoustic Streaming

The following section of literature is important as it forms the fundamental building blocks to the methodology in chapter 3. For this we should refer to Sadhal's [107]

for separating the components between undisturbed flow in the absence of acoustic propagation and a fluid flow in a perturbed state. Bringing together quiescent terms under subscript o and perturbed terms under superscript $'$ we can say:

$$p = p_o + p'$$ (2.28)

$$\rho = \rho_o + \rho'$$ (2.29)

We should consider that $p' << p_o$ and $\rho' << \rho_o$ and assuming that the flow is not rotational, u' can be expressed as a potential:

$$u' = \nabla\phi$$ (2.30)

Therefore, the momentum equation in perturbed state becomes

$$\nabla\left[p' + \rho_o\frac{\partial\phi}{\partial t}\right] = 0$$ (2.31)

which can then be integrated to:

$$p' = -\rho_o\frac{\partial\phi}{\partial t}$$ (2.32)

Sadhal [107] was then able to derive the wave equation by assuming both adiabatic compression and rarefaction, allowing for a linear relationship between pressure and density as follows:

$$p' = \left[\frac{\partial p}{\partial \rho}\right]_s$$ (2.33)

$$\rho' = c^2\rho'$$ (2.34)

The subscript s denotes an isentropic process and c represents the speed of sound. He then subbed these last three equations into the wave equation to obtain:

$$\frac{1}{c^2}\frac{\delta^2\phi}{\partial t^2} = \nabla^2\phi$$ (2.35)

Sadhal [107] was then able to apply the perturbation method to a quartz wind case using principles from both Nyborg[25] and Lighthill [12] by taking the continuity and momentum equation in quiescent state for a one-dimensional beam with frequency ω. Lighthills [12] principle for streaming velocity must be recapped as seen in the following equation:

$$\rho_o = \left[\bar{u}_i\frac{\partial\bar{u}_i}{\partial x_j}\right] = F_j - \frac{\partial\bar{P}}{\partial x_j} + \mu\nabla^2\bar{u}_j$$ (2.36)

None-dimensioning with respect to time in the form ω^{-1} and length c/ω, continuity and momentum equations become:

$$\frac{\partial u}{\partial t} + \epsilon u \frac{\partial u}{\delta x} = -\frac{1}{\epsilon}\frac{\partial p}{\partial x} + \frac{4}{3}\alpha\frac{\partial u}{\partial x} \tag{2.37}$$

$$\frac{\partial p}{\partial t} + \epsilon\frac{\partial u}{\partial x} \tag{2.38}$$

where it should be noted that ϵ is $\frac{U_o}{c} << 1$ and $\frac{4}{3}\alpha = \frac{\omega(\beta' + \frac{4}{3}\mu)}{\rho_o c^2} << 1$

We should refer back to the Gaussian function, used for jet velocity. Previous work indicates that it is also used for expressing amplitudes of both electric and magnetic fields. For this we should refer to Equation (2.8) and (2.9). In the context of acoustic intensity and circulation, investigated Wang and Kuznetsov [60]. Nyborg [25] defines the acoustic forcing term as:

$$F = -\rho_{of} < (u_{ac}.\nabla)u_{ac} + u_{ac}(\nabla.u_{ac}) > \tag{2.39}$$

The heat equation of a fluid is governed by:

$$\frac{\partial T}{\partial t} + u \cdot \nabla T = \eta_F \nabla^2 T + \frac{q_f}{\rho_{oF}\lambda_F} \tag{2.40}$$

η_F is the thermal diffusivity term and is expressed by $\frac{\lambda_F}{\rho_{oF}\lambda_F}$. Equation (2.40) can be combined with the linear expressions from Equation (2.36) and (2.37) to obtain:

$$\frac{\partial^2 u}{\partial t^2} - \frac{\partial^2 u}{\partial x^2} - \frac{4}{3}\alpha\frac{\partial^3 u}{\partial x^2 \partial t} = -\epsilon\frac{\partial}{\partial t}\left[u\frac{\partial u}{\partial x}\right] \tag{2.41}$$

Taylor expansion can then be used to expand $u(x,t)$ in powers of ϵ:

$$u(x,t) = u_o(x,t) + \epsilon u_1(x,t) + \epsilon^2 u_2(x,t) + ... \tag{2.42}$$

Lighthill's final expression for streaming velocity can be deduced as:

$$\frac{\partial^2 u_o}{\partial t} - \frac{4}{3}\alpha\frac{\partial^3 u_o}{\partial x^2 \partial t} = 0 \tag{2.43}$$

For a beam originating at $x = 0$ it has the following solution:

$$u_o(x,t) = e^{-2\alpha x/3}\cos(x-t) \tag{2.44}$$

Muller and Bruus [73] in their work on acoustic streaming in micro channels expands on Sadhal [107] and Eckhart's analysis. He was able to express these solutions in a frequency domain as well as a time domain using complex notation, the following expression is formed:

$$g_1(r,t) = Re[g_1(r)e^{-i\omega t}] \tag{2.45}$$

$$-i\omega\rho_1 = -\rho_o\nabla \cdot u_1 \tag{2.46}$$

Assumptions made here are that the boundary conditions constitute an adiabatic thermodynamic process and single frequency vibrations.

To derive the second order solution, the same principles are used. Referring back to Equations 1.24 and 1.25 for state and continuity, and retaining second order terms, the expansions from 1.28 and 1.29 can be reinserted thus expressing second-order perturbations of each variable:

$$\rho_o \frac{\partial u_2}{\partial t} + \rho_1 \frac{\partial u_1}{\partial t} + \rho_o (u_1 \cdot \nabla) u_1 = -c_s^1 \nabla \rho_2 + \mu \nabla^2 u_2 \tag{2.47}$$

Again, recapping Marshall and Wu [62], the essential building blocks of acoustic streaming is constituted by a steady component and an oscillatory component, thus the second-order steady state variables should be broken down accordingly. Muller and Bruus [73] explicitly state that the oscillatory component oscillates at 2ω. From trigonometry we know that:

$$\sin(\omega t) \sin(\omega t) = \frac{1}{2} - \frac{1}{2} \cos(2\omega t) \tag{2.48}$$

Thus, for a general field where subscript o denotes the steady component of acoustic streaming and the second order component is denoted by 2ω the following expressions, a temporal Fourier decomposition, is true:

$$g_2(r,t) = (g_2(r,t))^o + (g_2(r,t))^{2\omega} = < g_2(r,t) + Re[g_2^{2\omega}(r)e^{i2\omega t}] \tag{2.49}$$

This expression is only valid for steady periodic state, thus referring back to Riley's [55] definition of quartz wind type case as a steady flow.

Time averaging over one oscillation period $t_o = \frac{2\pi}{\omega}$ denoted by $< g_2$ is equal to the zero-order temporal fourier component in the form:

$$[g_2(r,t)]^o = < g_2(r,t) > = \frac{1}{t_o} \int_{t-\frac{t_o}{2}}^{t+\frac{t_o}{2}} g_2(r,t')dt' \tag{2.50}$$

The complex amplitude of the second order oscillatory mode is denoted by $g_2^{2\omega}(r)$ expressed by the following second order Fourier component:

$$g_2^{2\omega}(r) = \frac{1}{t_o} \int_{t-\frac{t_o}{2}}^{t+\frac{t_o}{2}} g_2(r,t')e^{-i2\omega t'}dt^t \tag{2.51}$$

Thus in order to derive a set of equations from second order that govern the steady component and one that govern the oscillatory component we use complex number mathematics to break down a set of terms A and B as follows:

It is known that the real part of any complex number Z can be written as $Re[Z] = \frac{1}{2}(Z + Z^*)$ where superscript $*$ denotes complex conjugation. Hence the produce $A(r,t)$ and $B(r,t)$ of two oscillating fields $A(r,t) = Re[Ae^{-i\omega t}]$ and $B(r,t) = Re[Be^{-i\omega t}]$ can be decomposed into a steady component and an oscillating component

$$A(t)B(t) = \frac{1}{2}(Ae^{-i\omega t} + A * e^{i\omega t})\frac{1}{2}(Be^{-i\omega t} + B * e^{i\omega t}) \tag{2.52}$$

which in turn is equal to the following:

$$\frac{1}{2}Re[A*B] + \frac{1}{2}Re[ABe^{-i2\omega t}] \tag{2.53}$$

From this expression we can introduce the following expression:

$$< AB >= \frac{1}{2}Re[A*B] \tag{2.54}$$

$$(AB)^{2\omega} = \frac{1}{2}AB \tag{2.55}$$

where A and B could be in any first order fields. Thus, we have our terms for the respective oscillatory and steady component of the flow.

Continuity: For the steady component.

$$0 = -\rho_o\nabla\cdot < u_2 > -\nabla\cdot < \rho_1 u_1 > \tag{2.56}$$

and the oscillatory component we have:

$$-i2\omega\rho_2^{2\omega} = -\rho_o\nabla \cdot u_2^{2\omega} - \nabla \cdot (\rho_1 u_1)^{2\omega} \tag{2.57}$$

Here we have set $\frac{\partial g_2}{\partial t}$ to be 0 for a general steady-state state second-order field as with $\frac{\partial g_2^{2\omega}}{\partial t} = -2\omega\rho_2^{2\omega}$

Momentum: The second order equation separates into a steady and an oscillatory component respectively.

$$< \rho_1(-i\omega u_1) > +\rho_o < (u_1\cdot)u_1 >= -c_s^2\nabla < \rho_s > +\mu\nabla^2 < U_2 > \tag{2.58}$$

$$i2\omega\rho_o u_2^{2\omega} + (\rho_1(-i\omega u_1))^{2\omega} + \rho_o((u_1 \cdot \nabla))^{2\omega} = -c_S^2\nabla\rho_2^{2\omega} + \mu\nabla^2 u_2^{2\omega} \tag{2.59}$$

The above two equations constitute a steady-state second order acoustic problem for a set of boundary conditions, assuming adiabatic thermodynamics and single frequency vibrations of the selected acoustic boundary.

Catarino et al. [14] were able to elaborate further on this method. By differentiating between first and second order, he stipulated that the outcome of first-order calculations was a time-averaged driving force, derived by integrating the driving force term over one wave period once stabilization of the periodic solution has taken place.

Thus, it is the time average force which can be used as the fundamental source term, described in our aims and objectives to incorporate a coupled solver. Included in the term are also the mass and body forces as well. The source term is then used to solve the second order set of equations with the solution for first-order being used as known data. Thus, after solving the second-order set of equations, the time

averaged values computed allow for analysis of the acoustic streaming effects over large time scales. Therefore, , the mean global flow is calculated.

Catarino [14] essentially breaks this down into a calculation methodology that can be used for a computational solver. Putting continuity and momentum equations into the following form:

$$\rho_o \frac{\partial u_1}{\partial t} - \nabla \cdot \Sigma = 0 \tag{2.60}$$

$$\frac{\partial \rho_1}{\partial t} + \rho_o \nabla \cdot u_1 = 0 \tag{2.61}$$

The term Σ denotes the expression:

$$-p_1 I + \mu(\nabla u_1 + (\nabla u_1^T) - \left(\frac{2\mu}{3} - k\right)(\nabla \cdot u_1)I \tag{2.62}$$

thus, for second order:

$$\rho_o \frac{\partial u_2}{\partial t} - \nabla \cdot \Sigma_2 = < -\rho_1 \frac{\partial u_1}{\partial t} - \rho_o(\nabla u_1 u_1) > \tag{2.63}$$

$$\frac{\partial \rho_2}{\partial t} + \rho_o \nabla \cdot u_2 = < -\nabla \cdot (\rho_1 u_1) > \tag{2.64}$$

The term in brackets $<>$ represents the time average over a cycle. Equation 2.64 denotes our none-linear driving force term. In conclusion, firm grounding has been achieved to build a robust methodology to model acoustic flow. The groundwork is laid for a concise outline that is elaborated upon in chapter 3 for the methodology of this research.

2.11 Summary

In summary, the understandings achieved in the literature can be divided into the following categories: Mathematical modelling, flow structure and geometrical effects.

Lighthill [12] establishes fundamental expressions for acoustic forces per length (F_l) and total (F_t). From this he was able to obtain the streaming velocity U_s as outline in Equation (2.36). In terms of approaches for the mathematical methodology, the literature outlines three distinct mathematical approaches; As mentioned previously, Trujillo's [15] comparison study for Gaussian jet velocity distribution (derived from lighthill) versus the turbulent circular jet solution (from Schlichting [98]) which both showed good agreement with experimental results. The findings have their limitations however, as the validation is only restricted to very low amplitudes.

The most robust appears to be the timescale discrimination approach as utilized by Moudjed et al. [99]. Recall that the method involved splitting each variable into their respective acoustic streaming components. A methodology along the same lines is utilized by Catarino et al. [14] through the distinction between first and second

order quantities. Here, expansion of variables of the Navier-Stokes equations took place into zeroth, first and second order. Equilibrium values corresponding to order zero represented constants in time and space in the absence of acoustic excitation. First order variables formed the damped propagation of the acoustic wave, providing a window into the instantaneous acoustic flow whilst second order represented the net global acoustic streaming effects. Wan and Kuznetsov as outlined in Section 2.3 use a similar approach. Recall that they also computed first order harmonic velocity field using this as known data for a steady state solution. In the context of the methodology in chapter 3, the literature review presents the fundamental building blocks to build a robust acoustic solver. Most notably, the gist of the research suggests that breaking the variables down into the fundamental acoustic and net average components is the most logical step in approaching the flow modelling. This will be outlined in chapter 3.

The overall consensus, in the context of flow structure is the presence of stationary re-circulation for an acoustically driven flow. All findings in the literature have established this. This is important as it establishes both steady state and dynamic behaviour of the flow in terms of the bulk fluid structure. Furthermore, all findings point towards and even number of circulatory loops for all investigations. However, gaps in the knowledge exist in the precise distribution of aspects such as temperature. We know from examples such as Setareh et al. [69], that thermal mixing induced by acoustic flow reduces boundary layer thickness, however previous work does not include detailed studies of the effects on thermal boundary layers from acoustically driven flows in a dynamic point of view. Whilst we know that stationary re-circulation occurs, no detailed modelling exists of the precise changes in temperature distribution across entire fluid domains subject to acoustic propagation with time. This aspect is important as it provides a fundamental window into the optimum methods of using ultrasound for enhanced heat transfer as we can gauge the temperature behaviour over a given period. It also provides the borderline between quantities exhibiting stationary stead-state variation verses quantities that exhibit dynamic variation with time.

Furthermore, the research lacks detailed parameterisation studies using quantities such as frequency or amplitude. From a geometrical point of view, all findings agree that a reduction in domain volume leads to an increase in pressure amplitude. We see this for findings from sajjadi et al. [74] and Tajik et al. [58]. In general, the literature also concludes that the increase in frequency correlates with the increase in maximum velocity but again the work lacks detailed parameterisation studies across a range of frequencies to determine how the velocity varies with incremental changes in velocity. Furthermore, in the context of flow structure, whilst it has been established that acoustically driven flow consistently demonstrates an even number of stationary circulatory cells, the quantity and structure of these cells as specific geometrical parameters are adjusted have not been covered in the literature. This aspect is important for parameterisation studies for engineering design, and utilizing the optimum parameters to achieve the most robust heat-transfer enhancement techniques possible.

CHAPTER 3

METHODOLOGY AND VALIDATION

The primary challenges associated with incorporating acoustic flow is the compressibility aspect of the flow domain. The fluids in this study and in previous studies in the literature are low speed incompressible flows. However, with the introduction of pressure perturbations from ultrasonic propagation, the fluid must undergo a compressible change in density (Viscous dissapation on the other hand is neglected due to the low-speed regime of the flow meaning the flow isn't turbulent). Thus a form of coupling must take place between incompressible and compressible flow to introduce the compressibility aspect to the flow. This is a significant challenge for the research and one that has been met with a number of approaches in previous work. Section 2.10 for acoustic modelling in the literature review refers to several methods for modelling acoustic propagation. Recall that several approaches are referenced; Gaussian jet velocity for example, the continuous wave approach being another but the overall theme points to the idea of splitting the respective variables of an acoustic flow into distinct components. Three methods are used to analyse Acoustic streaming; direct method, perturbation method and expansion of equilibrium [14] [107] [108] . Nevertheless Section 2.10 of the literature provides a breakdown of the mathematical approach from which we can build upon. The following chapter outlines Expansion of Equilibrium as the adopted approach for this investigation. Its robustness and easy adaptability into the CFD source code makes it an adequate approach to model acoustic flow.

Expansion of equilibrium essentially breaks the flow problem down into zeroth, first and 2nd order for individual fluid parameters such as velocity, density and pressure. For this we should refer back to Catarino's [14] derivations in Equation 2.60 through to Equation 2.64 in Section 2.10 of the literature. Thus we have:

$$u = u_1 + u_2 + u_3 \tag{3.1}$$

$$\rho = \rho_1 + \rho_2 + \rho_3 \tag{3.2}$$

Zeroth order in this case represents the fluid in a quiescent or undisturbed state. That is to say that it has been undisturbed and is absent of any ultrasonic propagation. The acoustic model can therefore be broken down into first and second-order components for the flow as outlined as highlighted previously.

The fundamental parameter, considered the unknown, which needs to be calculated, is the acoustic force. Recall from the literature that Lighthill [12] derived an expression for the force per unit length, thus culminating in Equation 2.1. Section 3.1 of this chapter delves into the fundamentals behind the derivation for this expression, however for the purpose of this section we should consider that a force, averaged from an instantaneous run time is calculated for one wave period. This is achieved through solving for the aforementioned first order quantities in the continuity and state equation. Note that the continuity equation is based on the principle of mass conservation for describing the transport of mass. The state equations describe the mathematical conservation of momentum and arise from Newton's 2nd law for fluid motion:

$$\frac{\partial \rho_1}{\partial t} + \rho_o \nabla \cdot (u_1) = 0 \tag{3.3}$$

$$\rho_o \frac{\partial u_1}{\partial t} = -\nabla c^2 \rho_1 + \mu \nabla^2 u_1 \tag{3.4}$$

The acoustic forcing term is calculated from this set of equation and can be subsequently considered as known data that can be applied to the second order system. The subsequent source term is as follows:

$$< -\rho_1 \frac{\partial u_1}{\partial t} - \rho_o (u_1 \cdot \nabla) u_1 > \tag{3.5}$$

Equation 3.5 represents the none-linear driving force term and as mentioned previously, can be inserted into second order system of equations. This system includes expressions for the mass and body force terms. They can thus be used to show the mean global flow for an instantaneous calculation for acoustic force from a set run time:

Section 2.10 of the literature review contextualises these equations so that they can be observed in both time and the frequency domain as seen in Equation 2.46 to Equation 2.59.

$$\frac{\partial \rho_1}{\partial t} + \rho_o \nabla \cdot (u_2) = < -\nabla \cdot (\rho_1 u_1) > \tag{3.6}$$

$$\rho_o \frac{\partial u_2}{\partial t} = -\nabla \cdot (c^2 \rho_2) + < -\rho_1 \frac{\partial u_1}{\partial t} - \rho_o (u_1 \cdot \nabla) u_1 > \tag{3.7}$$

Thus, Equation 3.6 and Equation 3.7 represent a second order system that can be solved by subbing in the forcing terms (in brackets) derived from the first order set of equations. Thus an overall global solution for an instantaneous run time is solved. Section 2.3 of the literature review contextualises these equations so that they can be observed in both time and the frequency domain as presented in Equation 2.46 to Equation 2.59.

3.1 Derivation of Equations for Expansion of Equilibrium

The following section outlines the principle behind Equation 3.1 and Equation 3.2. Here we outline how both compressibility and incompressibility are coupled to account for density changes due to perturbation in the flow. For the outlined methodology to be true we must consider the following: Referring back to Equation 3.4 we assume that pressure p is a function of ρ only:

$$\nabla p = c^2 \nabla \rho \tag{3.8}$$

c is the function of ρ which has units of velocity. We also assume that the motion is isentropic.

If we are to assume that X is a unit of length in cm, with T being a unit of time and U as the velocity in cms^{-1}, then we can write the governing equations, continuity and Navier-Stokes with homogeneity in ρ:

$$\left[\frac{\partial \rho}{\partial t}\right] + N\nabla \cdot (\rho u) = 0 \tag{3.9}$$

$$\left[\frac{\partial(\rho u)}{\partial t}\right] + N[\rho u \cdot \nabla u + u\nabla \cdot (\rho u)] = -\left[\frac{NC^2}{U^2}\right]\nabla \rho \tag{3.10}$$

where $N = \frac{UT}{X}$, thus ensuring the system of units serve its purposes. X and T are chosen so that $\frac{\partial f}{\partial t}$ and $\frac{\partial f}{\partial x}$ are of the same order of magnitude (with f denoting a function of ρ, u etc. U is chosen in any number of ways so that $N = 1$ or $\frac{c}{U}$ 1 or $\frac{u}{U}$ 1. Once these systems of units are defined, the acoustics can be defined as a hydrodynamic problem where $N << 1$ and $\frac{Nc}{U}$.

Let us introduce the quantity $C(\rho) = \frac{Nc(\rho)}{U}$

Therefore Equation 3.10 becomes $N\left[\frac{\partial(\rho u)}{\partial t}\right] + N^2[\rho u \cdot \nabla u + u\nabla \cdot (\rho u)] = -c^2\nabla \rho$

N is now treated as a perturbation parameter, thus giving us an aforementioned method for modelling acoustic steaming, expansion of equilibrium, as presented in Equation 3.1 and Equation 3.2.

$$\rho = \rho_o + N\rho_1 + N^2\rho_2 + ... \tag{3.11}$$

$$u = u_o + Nu_1 + N^2u_2... \tag{3.12}$$

3.2 Coupling to Simplify First and Second Order Equations

As mentioned previously, zero order with subscript o represents the fluid in an undisturbed state. Thus we can represent the zero-order equation as:

$$\left[\frac{\partial \rho}{\partial t}\right] = 0 \tag{3.13}$$

$$c^2 \nabla \rho = 0 \tag{3.14}$$

where $c_o = c(\rho_o) \therefore \rho_o = const$

The coupling of the different fluid states is achieved through the simplification of the first and second order equations. Thus we have for first order:

$$\frac{\partial \rho_1}{\partial t} + \rho_o \nabla u_o = 0 \tag{3.15}$$

$$\rho_o \left[\frac{\partial u_o}{\partial t} \right] = -c^2 \nabla \rho_1 \tag{3.16}$$

and for second order:

$$\left[\frac{\partial \rho_2}{\partial t} \right] + \rho_o \nabla_o \cdot (\rho_1 u_o) = 0 \tag{3.17}$$

$$\rho_o \left[\frac{\partial u_1}{\partial t} \right] + \left[\frac{\partial}{\partial t} \right] [\rho_1 u_o] + \rho_o (u_o \cdot u_o) = -c_o^2 \nabla \rho_2 + c_o + \left[\frac{dc_o}{d\rho_o} \right] \nabla \rho_1^2 \tag{3.18}$$

As part of the data for this thesis, the results will incorporate vorticity magnitude calculations to measure the circulatory currents in the flow. The vorticity(Ω) function within OpenFOAM is defined as:

$$\Omega = \nabla \times u \tag{3.19}$$

3.3 Validation of the Chosen Methodology

Figure 3.1 presents the problem posed for this validation exercise. The aim is to study the characteristic effects of acoustic streaming within a closed container. Recall that it was discussed in the literature review that Marshall and Wu [62] identified that the two fundamental components for acoustic streaming were a pair of oscillatory regions of flow coupled with the overall global flow dominated by buoyancy. They were able to provide a schematic of this, presented in Figure 3.1. The associated vorticity magnitude plot presented is a result obtained for this section and provides an example of the characteristic flow structure for acoustic streaming. It is a plot taken from the validation study which will be covered in this section. It represents a platinum wire submerged in a tank and is based on an experimental investigation carried out by Dehbani et al. [13]. They wanted to study the effects of ultrasonic cooling on a platinum wire. The liquid in the domain is water. A heat flux of $144 kwm^{-2}$ was applied across this wire. The vorticity contour plot in Figure 3.1 presents vorticity contours generated in OpenFOAM based on the setup from Dehbani et al. [13] when a heat flux of $144 kwm^{-2}$ was applied across the wire. Refer to Figure 3.2 for the location of the transducer. Wave propagation is in the y-direction. Further details are presented as follows. The heat flux boundary condition was set by applying a boundary condition specific to the OpenFOAM library called "Fixed

Gradient". This means that the normal gradient at the patch or surface boundary is fixed. It is an implicit boundary condition meaning it will be dependant on a variable-inside said patch which is going to change. We can therefore say for a fixed gradient g that $\frac{\partial \phi}{\partial n} = g$ for a specified boundary (in this case, the wire surface). The value for this boundary condition was then assigned based on $\frac{Q}{K}$ where Q is the specified heat flux and K is the thermal conductivity of the boundary. The temperature was then measured using a mean function in Python that was applied to the entire wire surface to generate an average temperature value. For the transducer inlet that made use of a $A_o sin\omega t$ function, the transducer displacement A_o was set to 2.5×10^{-7} m.
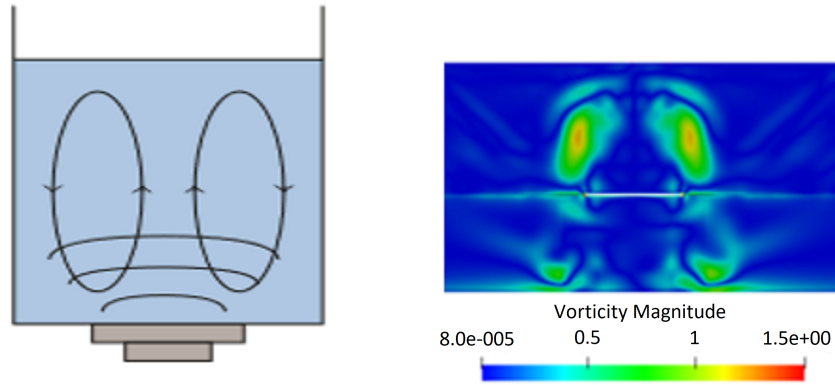
Figure 3.1: A schematic drawing of the classic acoustic streaming flow structure from Marshall and Wu [62] (left) showing a pair of circulatory regions of flow compared with a solution obtained from the code for this paper showing vorticity magnitude for the problem geometry in question (right).
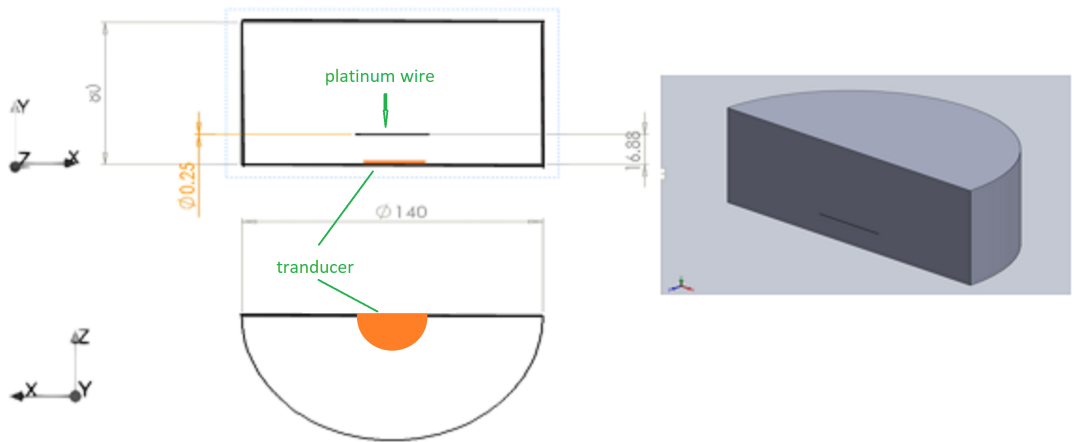
Figure 3.2: Problem Geometries.

Figure 3.2 presents a schematic of the problem geometry. It represents a three-

dimensional setup for a submerged platinum wire in a steel tank with a symmetry plane. The problem is a simplification of the experimental setup from Dehbani et al. [13].

The transducer is placed at the bottom face of the problem geometry as indicated in Figure 3.2, with a velocity inlet function of $V = A_o \sin(\omega t)$.

The operating temperature of the domain was set to $280.5K$. The experimental rig contained an ice bath in which the entire perimeter of the icebath was housed. The surrounding wall boundary conditions were therefore set at $273K$ to simulate these conditions. A pressure outlet was set at the free surface of the water and a symmetry plane was selected for the cross-sectional face.

For validation, five different heat fluxes were applied at the wire surface using a structured hex-dominant mesh. The first step was to validate a basic convection model in OpenFOAM with no acoustic oscillations. Acoustic streaming was then modelled using outlined methodology in the previous section.

3.4 Results of the Validation

Figure 3.4 presents the temperature distribution across the symmetry plane for a heat flux of $144kwm^{-2}$.
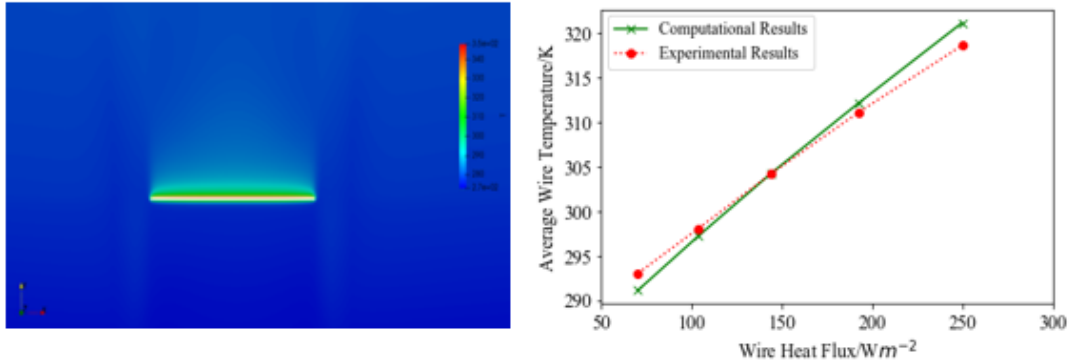
Figure 3.3: (left) Temperature distribution for a steady state convection solution when a 144 kWm-2 heatflux is applied at the wire and (right) average temperature measured at the wire surface for five different heat fluxes.

The Thermal boundary layer structure across the wire surface has been well resolved. Measurements of the average temperature distribution were also made for each heat flux and compared to the experimental values as seen in Figure 3.4. Results show good agreement thus indicating that the chosen numerical method for convection can be used to build the solver for acoustic streaming resolution as outlined in Section 3.1.

The instantaneous acoustic flow is therefore presented in the solution for first-order. Figure 6 presents the pressure distribution for a first-order solution where the instantaneous perturbations due to acoustic flow are shown. A frequency of 1.7

MHz at a run time of 5.5×10^{-5} was used to calculate the resulting solution and to ensure periodic stabilization.
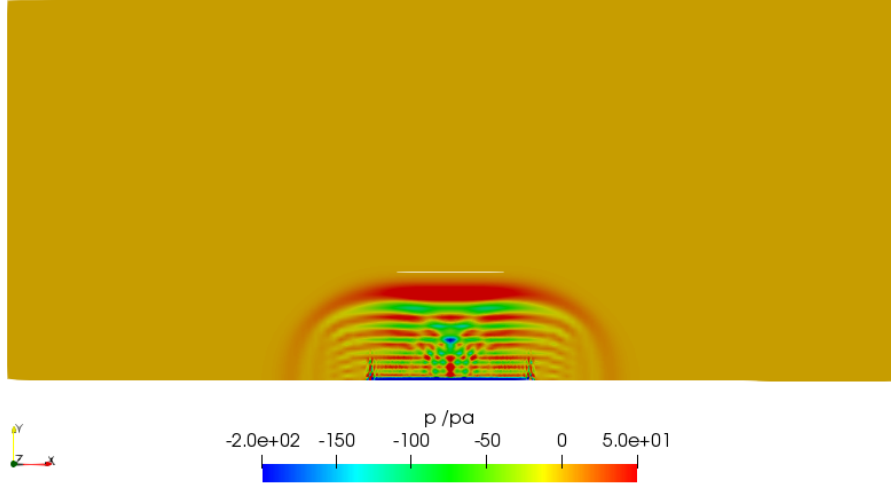
Figure 3.4: Instantaneous pressure distribution due to acoustic disturbances with a frequency of 1.7 MHz at $1 \times 10^{-5}s$.

As mentioned in Section 2.10, the above solution provides the instantaneous driving force by integrating the driving force over one wave period. The outlined set of second-order equations uses this solution as known data to provide information on the acoustic streaming effects on larger time scales. Figure 3.5 provides information on the acoustic streaming effects on a global scale once the second order equations have been solved thus demonstrating the classic flow structure seen in acoustic streaming with both a circulatory component and a mean global component.
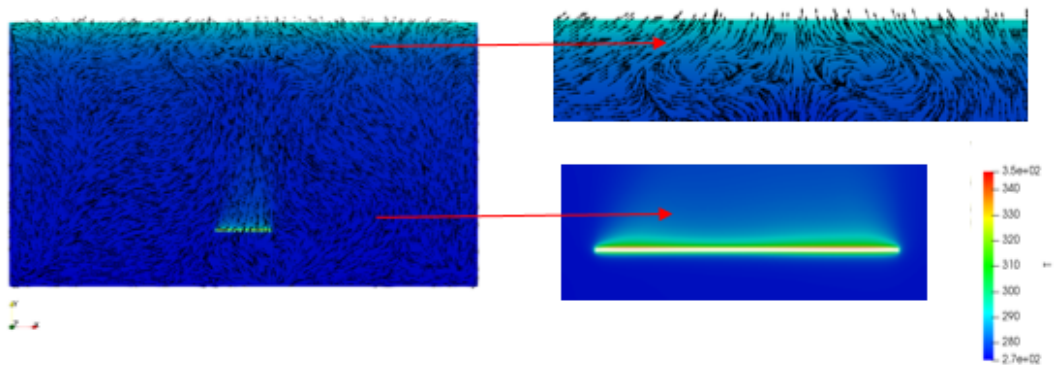
Figure 3.5: Velocity vector plots: showing the classic circulatory flow associated with acoustic streaming and the resulting thermal boundary layer disturbance for a heatflux of $249.6kWm^{-2}$.

The effects on heat transfer are measured once again by ascertaining the average

temperature distribution of the wire and comparing them with the results in Figure 3.4.
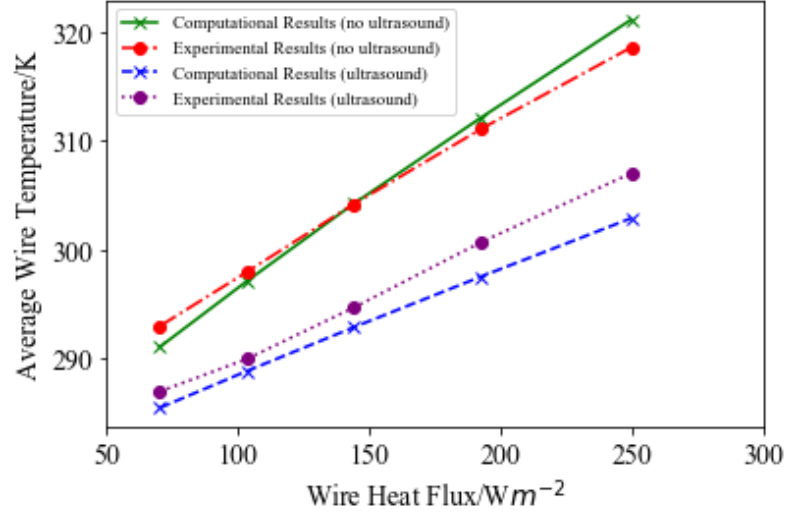
Figure 3.6: A graph to show the acoustically induced heat transfer effects by showing the temperature distribution across the wire surface.

The effects of an acoustically induced flow are clear. The computational model can demonstrate that ultrasonically induced flow is able to enhance heat transfer with reasonably good agreement with experimental results. Heat transfer Coefficients were calculated for each heat flux and a heat transfer enhancement percentage was calculated using the formula $\frac{Nu_{us}-Nu_0}{Nu_0} \times 100$ where Nu_0 and Nu_{us} were Nusselt numbers for none-acoustic and acoustically induced flow respectively.

Here Figure 3.7 demonstrates that the model is able to reproduce the asymptotic trend with reasonable approximation although the computational model does overpredict the heat transfer enhancement.

3.5   Summary

In conclusion, the methodology has demonstrated adequate grounding in being able to model acoustic flow against experimental results. The results show that, coupling, achieved through the method of splitting the components down into respective degrees of order provides adequate resolution of the overall bulk global flow. Furthermore, already, the effects on heat transfer can be observed before even covering the main bulk of the work in this thesis. The effects of heat transfer enhancement in Figure 3.7 is evident with ultrasound propagation clearly having the more positive effect. The asymptotic trend mentioned previously also provides us with a window into the effects of heat flux on overall temperature for a heat source. Chapter 6 cover this setup in more depth with a more concise study of the geometry associated with the current findings. Nevertheless, in the context of research, the methodology has established an adequate coupling method that shows good agreement with experimentation. Furthermore, the model is able to predict flow structures within the
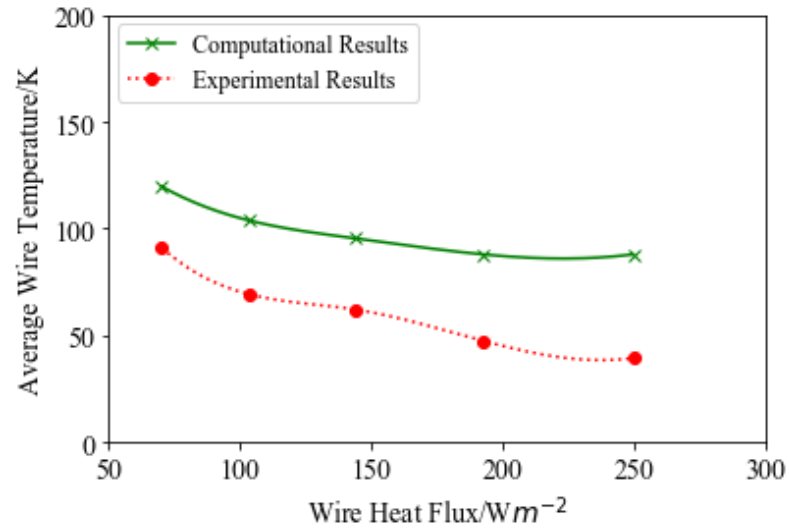
Figure 3.7: A graph to show the heat transfer enhancement for the corresponding wire heat fluxes.

classical remit of counter rotating circulation that has been observed so frequently in the literature and provides fundamental grounding to the likes of Lighthill, Sajjadi and Nyborg. In doing so, we can now study the effects of ultrasound in a much greater scope. Again we should refer back to Section 2.11 in which it was concluded that the literature study lacked detailed parameterisation studies of charecteristics such as ultrasonic frequency. We thus move to Chapter 4, which takes this study to the next step in observing the effects of ultrasound on fluid flow.

CHAPTER 4

THE EFFECTS OF FREQUENCY OF ULTRASOUND ON THE THERMAL BOUNDARY LAYER OF ACOUSTICALLY DRIVEN FLOWS

The mechanism of cooling is explained in Section 2.8 through the example of a microfluidic device provided by Guo and Sun [65] and outlined in Figure 2.19 through idea of acoustically forced convection currents that carry heat way from the resulting thermal boundary layer thus breaking down the thermal boundary layer structure. The importance of identifying the fluid structure for acoustic streaming as highlighted in Section 3.5 of the previous chapter cannot be understated. The purpose of Chapter 4 is to ascertain the effects of ultrasonic parameters, specifically frequency on said thermal boundary layer using Rahimi et al. [97] as a geometry reference and developing observations based on the behaviour outlined by Guo and Sun [65]. Section 4.5 outlines the fundamental flow structure, divided into the inner Schlichting Streaming located in the bulk of the fluid and the Rayleigh streaming located in the Stokes boundary layer. Referring back to the conclusions drawn from the literature review, a significant gap exists in the literature relating to detailed parameterisation studies of quantities such as frequency. The purpose of this chapter is to identify the changes to thermal boundary layer structures in relation to flow circulation and flow vorticity, defined as the curl of the velocity distribution and thus gain a better understanding of the mechanism behind cooling.

4.1   Motivation

For the purpose of this chapter, we refer back to Section 2.9 of the literature review. Understanding the mechanisms in microfluidics for applications such as cooling chips and medicinal cleaning is paramount to be able to ascertain the optimum design. As mentioned previously [65], acoustic streaming is known to encourage fluid mixing from forced convection currents that transport the heat away from the thermal boundary layer, leading to the provision of additional liquid to a heat transfer sur-

face. The study of a thermal boundary layer can be utilized in this regard. By studying the changes to the temperature gradient within the boundary layer, the quantitative effects of acoustic streaming on mixing can be studied and as a consequence, its effects on cooling. This can be effectively achieved by studying the variation with frequency at detailed incremental steps for a vast range along with net effects on quantaties like temperature. Rahbari and Pniagua [109] noted that the interaction between the so-called stokes boundary layer and the viscous sub-layer is significantly influenced by the frequency of oscillations. The literature review outlines links between frequency and numerous streaming aspects such as amplitude and streaming velocity. Recall for example, Parvizian et al. [106] who found a direct correlation between acoustic frequency and streaming correlation when studying the mixing rate in a sonoreactor. Yamamoto et al. [105] found that amplitude and frequency are completely independent of each other in their study for treatment of molten metals. Thus the purpose of this chapter is two-fold: Understanding of the cooling mechanism in relation to boundary layer structures when a fluid undergoes acoustically forced mixing and to build on the parameterisation links that influence acoustic streaming in frequency. This is incredibly important due to the problems encountered in the design of engineering components such as sonoreactors for mixing and cleaning. Rashwan et al. [110] noted that a full knowledge of the best working conditions for a sonoreactor is insufficient within the acoustic field. They noted in their findings that a maximum negative pressure corresponds with a higher frequency and amplitude. Navarro-Brull et al. [111] identified that the frequent challenges associated with the design of these devices included frequent clogging, non-uniform distribution of multiphase flows and poor solid handling.

4.2 The Thermal Boundary Layer

In many ways, the nature and development of a thermal boundary layer mirrors that of a velocity boundary layer. Consider for example, a fluid flowing with temperature T over a cladding surface; The flat plate model, as presented in Figure 4.1.
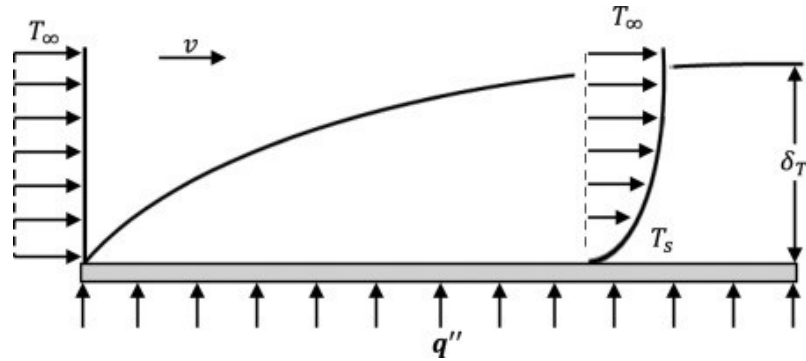
Figure 4.1: Development of a thermal boundary layer [112].

As the fluid traverses the plate, the development of the boundary layer is such that it eventually forms as above with thickness δ as defined by δ_T. According Ghosh

and Saha [113], higher flow rates reduce the thickness of a thermal boundary layer. Xu et al. [114] noted that the interruption of a thermal boundary layer formation had positive effects for heat transfer. They were able to develop a new silicon microchannel heat sink in which the development of the thermal boundary layer was controlled by dividing the parallel micro-channels both longitudinally into several independent zones. This redevelopment of the boundary layer was shown to greatly enhance heat transfer. In this respect, the acoustic effects on the thermal boundary layer will not only help increase our understanding of the overall phenomenon, but could have major applications for areas in micro cooling by developing further understanding of boundary layer behaviour.

Several methods are known for inducing a thermal boundary layer structure. Li and Nalim [115] note that changes to its structure can be induced by imposing a heatflux across a wall surface or by imposing a temperature boundary condition. They modelled a transient temperature profile for a step change in fluid temperature where there is no initial thermal boundary layer. They noted the occurrence of a steep temperature gradient in the middle range of the developed thermal boundary layer as presented in the figure below:
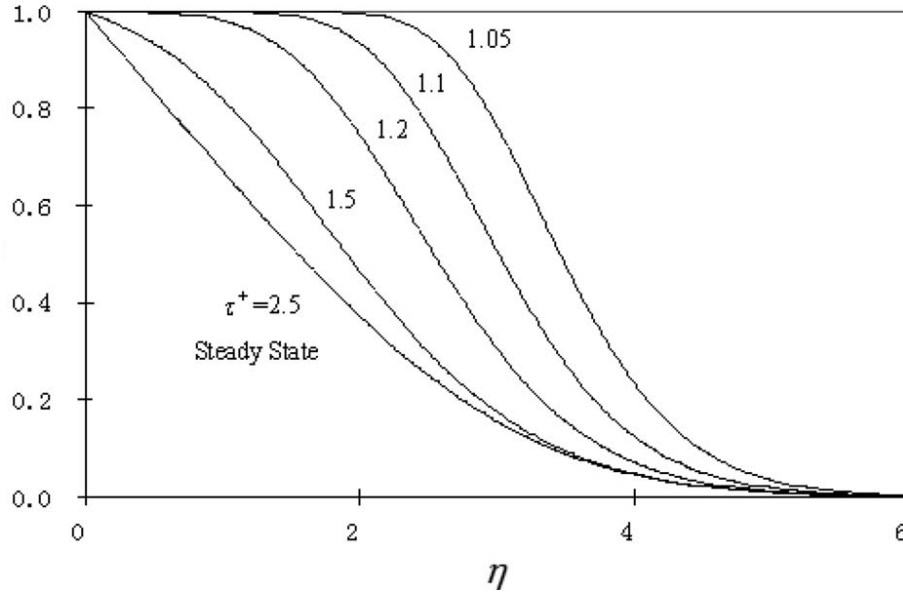
Figure 4.2: Temperature response to step change in incoming fluid temperature with no initial thermal boundary layer [115] The y-axis represents normalised temperature distributions.

η in this case represents the distance travelled by the contact surface from the leading edge relative to the distance x of any location of interest. τ^+ represents the sheer stress relative to x, I.E $\tau^x = \frac{\tau}{X} = \frac{U_\infty t}{x}$. . Recall that x is the stream wise distance. They highlighted the fact that the temperature gradient at the wall did not change until after τ^+ exceeded 1.2.

Within the context of this chapter, the geometry is analogous to a confined liquid in a closed boundary. . M. Kolar [116] at the Lewis Research centre for

NASA investigated a similar setup for a thermal boundary layer in a confined liquid. A constant heat flux was applied and parameters were developed to indicate the presence of both a quasi-steady state and boundary layer flow. The geometry is presented below:
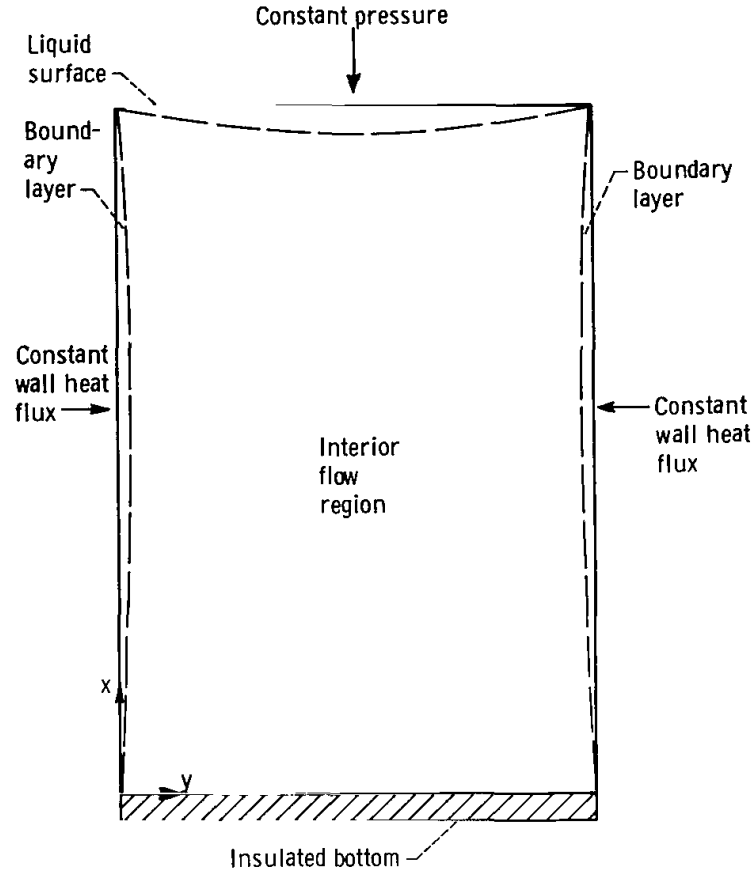
Figure 4.3: Model setup from Kolar [116] for an enclosed liquid subjected to constant wall heat flux.

Temperature profiles near the wall were taken at 0.00254 cm increments away from the wall at the central tank axis.

A more concise distribution that shows the change in boundary layer thickness across the axis of symmetry is presented as follows:

It can be seen that as the value of x increases, the effects of stratification and the liquid surface become dominant. The experimental boundary layer thickness becomes zero near the liquid surface. Heat is subsequently transferred from the walls to the interior of the fluid.

They make note of a couple of characteristics however. The condition for quasi-steady state is Rayleigh number dependant. Incorporated into this dependency is the difference between the wall and the exterior height. They noted that after $180s$, this temperature difference was found to be nearly constant. I.E, the wall and
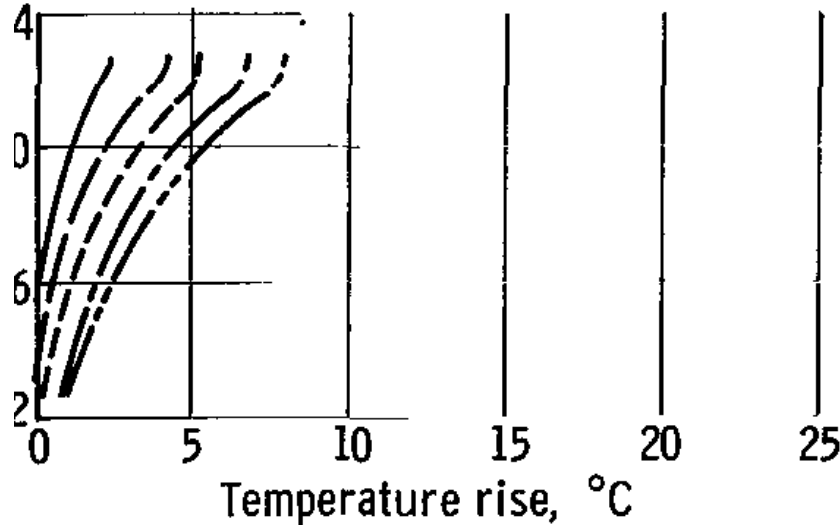
Figure 4.4: fluid temperature across central tank axis for a wall heat flux of 5.5 Watts per Square decimetre [116].

interior temperatures rose at approximately the same rate.

Thus, linking thermal boundary layer thickness within this context back to the flat plate model as outlined in Figure 4.1, it is important to consider the following. Kolar [116] identified distinct regions where the boundary layer in terms of its temperature profile showed correlation with the predicted model. In particular, it was found that a region existed within the laminar boundary layer were predicted fairly well by the flat plate model. Furthermore there is a region near the liquid surface in which surface effects destroy similarity characteristics and reduce boundary layer thickness. Thus, within the context of this chapter, if we were to consider a completely closed domain of liquid without a free surface then the flat model is a viable approximation.

We must further consider specific aspects of the methodology as laid down in Chapter 3. In particular, the meshing strategy should be considered along with OpenFOAM's ability to accurately model convection (as laid out in Chapter 3, the mathematics is built upon a base convection model in OpenFOAM's source code). Overall, the model has already been validated in Section 3.3, but to add further grounding to the results, it is important to demonstrate that OpenFOAM is able to resolve a boundary layer with considerable accuracy. For this exercise, we can use the work of [116] as a reference. Referring back to Figure 4.3, a geometry can be constructed which accurately represents the schematic through a simplified medium (Figure 4.6).

As per Figure 4.4, the heat fluxes applied across the side walls for the experiment were set at 5.5 Watts per square decimetre. The schematic in Figure 4.6(III) presents the outline of the boundary conditions set to represent this. Note that the fixed gradient condition is an in-built boundary condition in OpenFOAM that represents a heat flux across a boundary. Table 4.1 presents the respective boundary conditions for each region labelled in Figure 4.6(III).
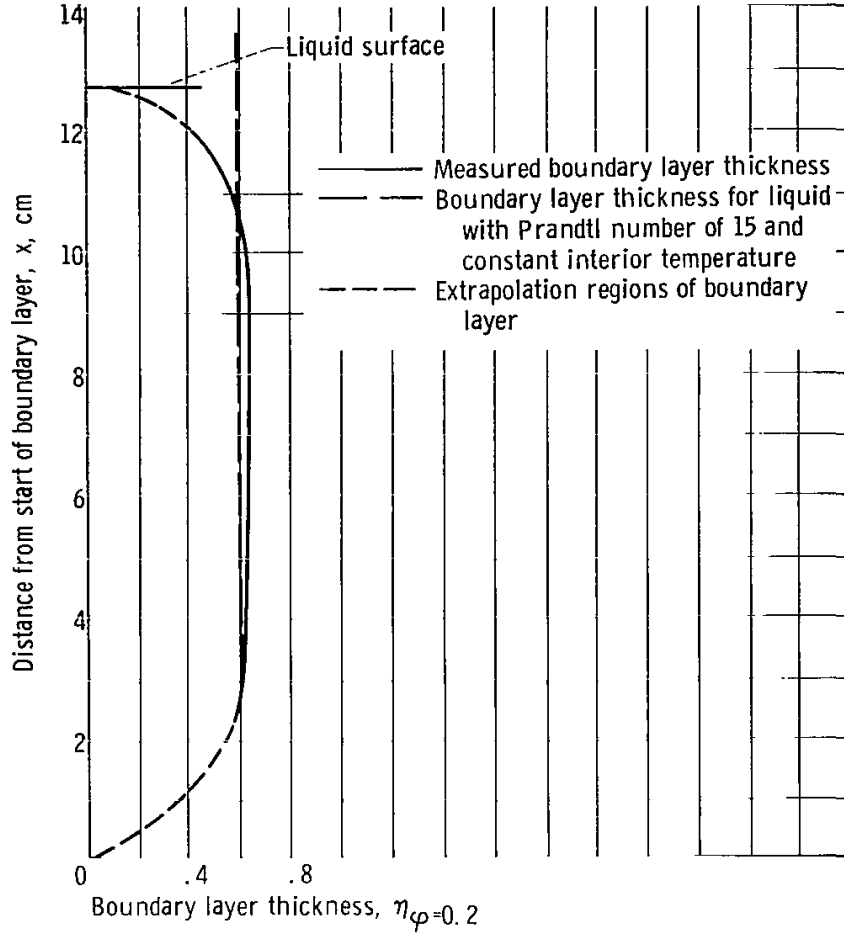
Figure 4.5: Fluid temperature across central tank axis for a wall heat flux of 5.5 Watts per Square decimetre [116].

Inflation layers (layers that formed a gradually decreasing sizing that corresponded to wall proximity) were added in the mesh at the sidewalls to accurately resolve the heat dispersion as a result of the heat fluxes applied (Figure 4.6(II)).

The mesh consisted of the following properties, with the smallest cell sizing representing the smallest layer in the inflation region as seen in Table 4.2.

A steady state plot of the temperature distribution is presented in Figure 4.7a. Results could then be compared by measuring the temperature profile along the axis of symmetry and comparing this to the experimental data presented in Figure 4.7b. Recall that each curve represented a measurement at a specific time after heating. The comparisons are presented in Figure 4.7b.

As per Section 4.5 of the literature review, Landau and Lifshitz [56] outline the fundamental fluid structure for a fluid domain undergoing acoustic propagation as depicted in Figure 2.1. The so called "Stokes Boundary Layer" is the wall boundary layer that lies in the region. In this region, Rayleigh streaming takes place, defined by circulation in the vicinity of the solid boundary. Within the bulk of the
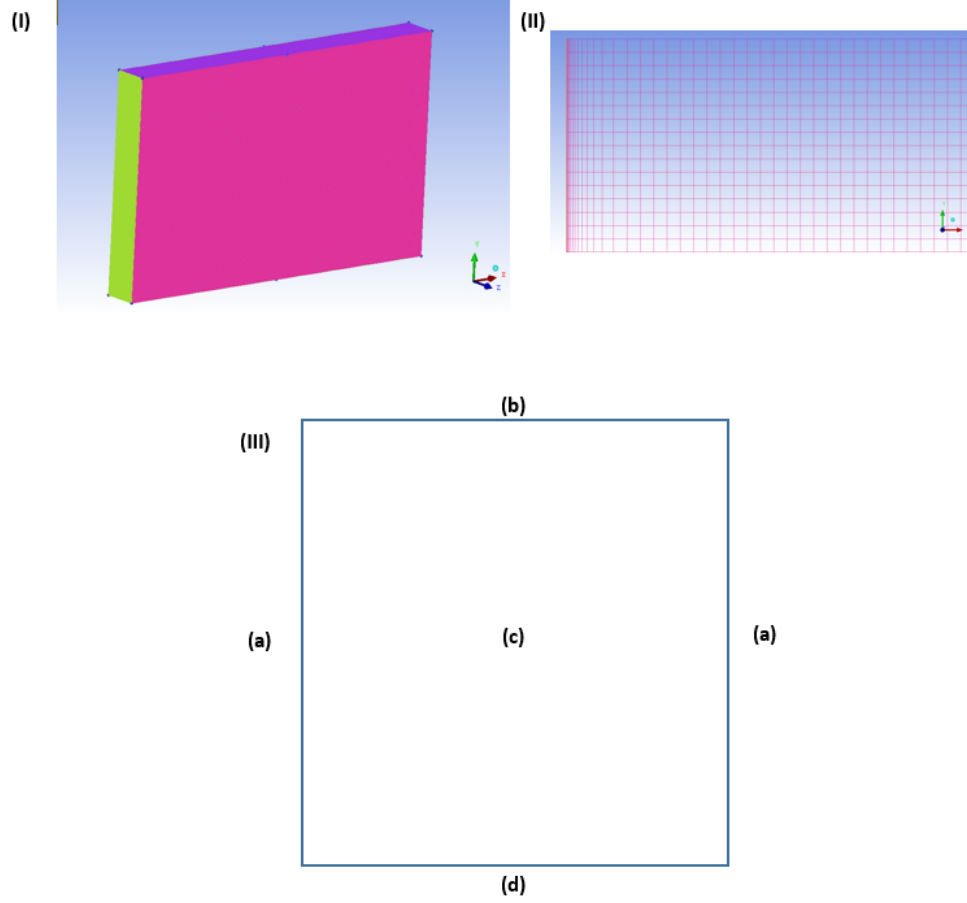
Figure 4.6: Various views of the meshed geometry used for OpenFOAM to model the data presented by Kolar [116] to show an isometric view (I), the near-wall meshing strategy (II) and the labelled boundary conditions (III) which are outlined in detail in Table 4.1.

fluid, circulatory region that are counter-rotating take place, denoted by the term Schlichting streaming. As noted by Rahbari and Paniagua [109], the contribution of the frequency of oscillations is such that at high frequencies, the edge of the stokes boundary layer falls within the viscous sublayer- a fluid state known as "quasi-laminar". Lower frequencies lead to a so-called "quasi-steady regime" where the stokes boundary layer thickness goes beyond the laminar sub-layer. These terms are fundamental in understanding the basic premise for acoustic streaming in a closed domain. Within the context of this chapter, the aim is to approximate this model using the CFD methodology and study the flow behaviour in specified regions, more specifically, in the Stokes. Furthermore based on the correlation demonstrated in Figure 4.7, the appropriate meshing strategy can therefore be used for the modelling in this thesis. That is to say, that parameters in Table 4.2 will be utilized for this thesis based on the CFD comparison work carried out.

64

Table 4.1: Boundary Conditions for OpenFOAM as presented in the schematic for the computational domain based on Kolar [116] presented in Figure 4.6(III).

boundary	OpenFOAM boundary condition	value
a	wall (no-slip)	fixed gradient (5.5 Wm^{-2})
b	pressure outlet	293K
c	internal	293K
d	wall (no-slip)	293K

Table 4.2: Mesh sizing characteristics for OpenFOAM modelling.

type	cell number/million	average cell spacing/m	smallest cell spacing/m
hexagonal	12.6	3.6×10^{-4}	3.6×10^{-4}

4.3 Geometry and Boundary Conditions

A simple three-dimensional geometry with a depth of 21 mm and based on Rahimi et al. [97] was constructed based on the meshing parameters presented in Section 4.1 All sides of the domain were assigned as walls with no-slip conditions. A velocity inlet with condition $A_o \sin(\omega t)$ was assigned to a representative transducer location allocated as the source of acoustic propagation.

4.4 Physical Problem and the Geometry

The literature covers flow structures for acoustic streaming at geometry sizes significantly smaller than the wavelength. However a knowledge gap exists for scales of geometries larger than the acoustic wavelength. Characteristics such as the number of streaming vortices, the effect of circulation on Rayleigh streaming in the stokes boundary layer and the subsequent thermal boundary layer mixing are all such areas where there are gaps as outlined in the conclusion section in Chapter 2. The problem addresses a simple setup whereby temperatures are assigned to the wall in a convective model. Figure 4.9 presents these boundary conditions along with the corresponding temperature plot showing convective flow within the domain and the resulting boundary layers formed on the top and bottom wall. The temperature for the internal field of the flow domain was set to $280.5K$.

Unforced convection results in the temperature distribution seen above. In this case, there is no external force such as acoustic flow being applied and the resulting steady-state solution is as a result of unforced convection.

With the application of acoustic flow, eighteen frequencies ranging from 150 kHz to a maximum of 500 kHz were studied. To put these frequency values into context, according to Yao et al. [22], a typical high-power ultrasonic transducer with a range between 16 and 100 kHz used 0.1 Wcm^2 of energy. Asakura et al. [117] developed transducers with a working frequency of 500 kHz with a total effective power of 620 W.
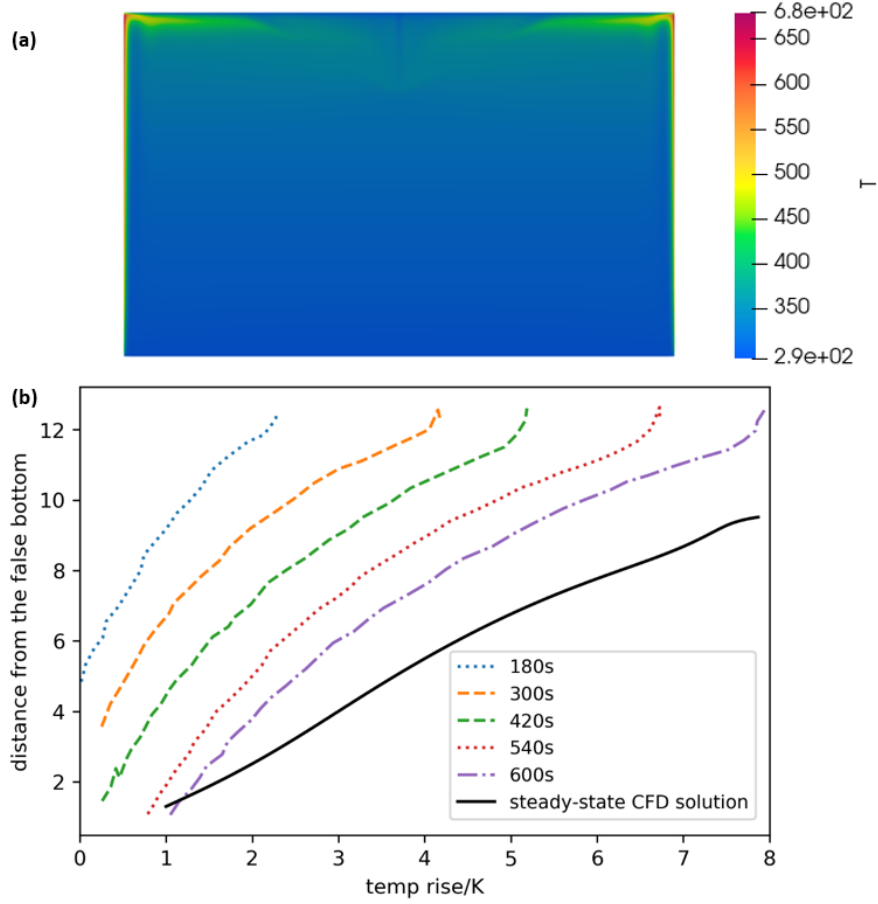
Figure 4.7: (a) Temperature distribution for the geometry based on Kolar [116], modelling in OpenFOAM (b) Comparisons between experimental data presented by Kolar [116] and a steady-state CFD solution obtained from OpenFOAM.

A velocity boundary condition of $A_o \sin(\omega t)$ was applied where the amplitude A_o was set at 6.55×10^{-7}.

4.5   Results and Discussion

Figure 4.10 presents the pressure wave propagation and the temperature distribution at a frequency of 150 kHz.

The resulting change in wavelength with frequency is presented in Figure 4.11. Here, an exponential decrease with frequency can be seen as can be expected for the standard inverse relationship between frequency and wavelength:

Figure 4.10 highlights the resulting disruption of the thermal boundary layer as a result of the flow circulation in the Schlichting region. This is highlighted by red circles in the figure that highlight the boundary layer disruption. An alternative view of this disruption can also be been in 4.12, comparing the results of acoustic flow with a frequency of 150 kHz with thermal boundary layer for an unforced convection case where natural convection is the dominant flow mechanism. We notice that the
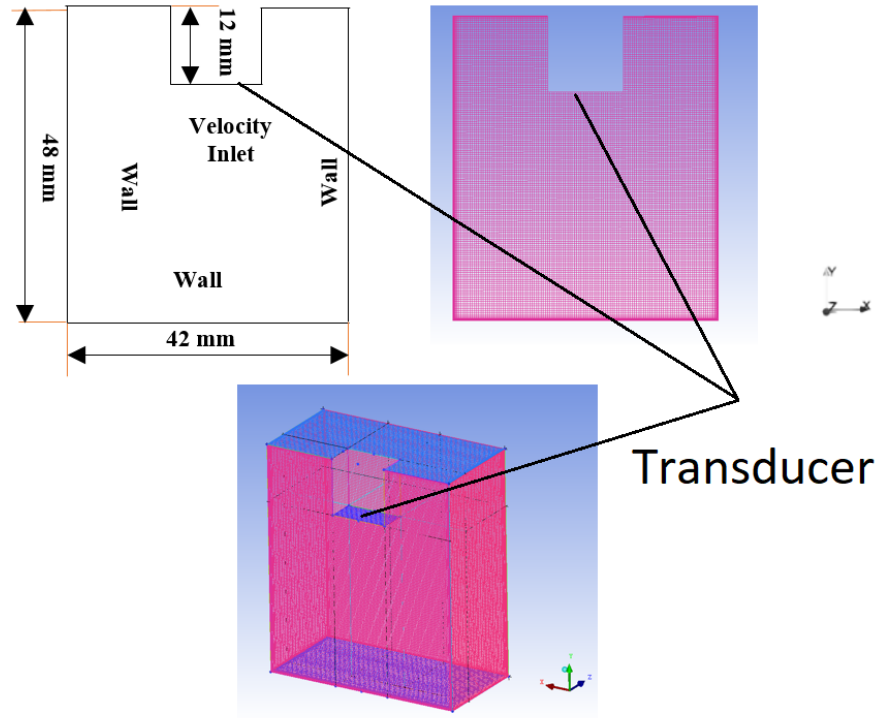
Figure 4.8: (top left) Computational Geometry and boundary conditions, (top right) the mesh constructed across the symmetry plane with refined layers at the wall to resolve the thermal boundary layers, and (bottom) isometric view of the geometry.

thermal boundary layer undergoes a significant change in shape when subject to forced convection from acoustic flow. Its thickness has essentially reduced. For this, we can refer back to Section 2.8 in which a microfluidic device from Guo and Sun [65] is used to explain how the dispersion of heat aids in cooling. The currents induced from acoustically forced convection carry the heat away from the wall (the heat source) with a constant rate of internal heat generation, thus the resulting observational change is a change in shape of the thermal boundary layer eminating from said heat source, as displayed in Figure 4.12.

Here, a more quantifiable effect can be seen in the changes in structure to the thermal boundary layer, taken with a line probe in the region of Rayleigh streaming, when subject to a 150 kHz wave propagation. The finding correlates well with Setareh et al. [69] (see See Section 2.3 of Chapter 2) who noted that enhanced mixing reduced thickness by carrying heat away from the vicinity of the source as outlined by Guo and Sun [65]. In this case, the resulting thickness of the boundary layer has been significantly altered. The temperature gradient reaches freestream conditions at a closer distance to the wall. Moreover the effects of cooling are seen through fluid mixing as the free stream temperature for acoustic flow is lower than unforced convection thus giving us an indication of the overall effects of acoustic streaming
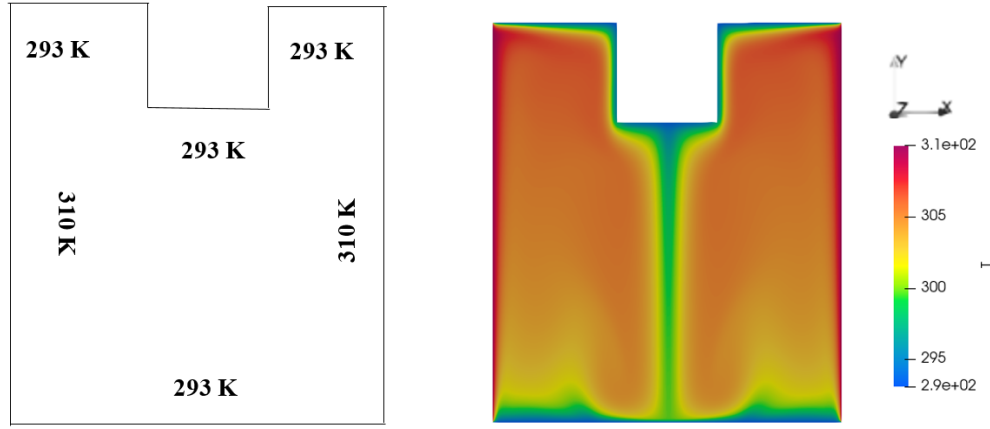
Figure 4.9: (left) Assigned boundary conditions for temperature and (right) the resulting temperature plot for convective flow, note the shapes of the thermal boundary layers on the top and the bottom wall.
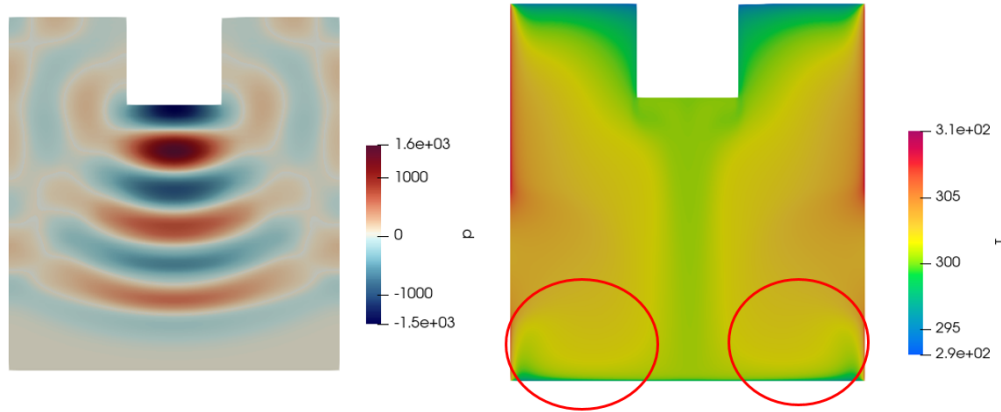
Figure 4.10: (left) Pressure perturbations and (right) temperature contour distributions for a 150 kHz wave.

on temperature distribution and subsequently heat transfer as the forced convection currents have transferred heat away from the near-wall vicinity. The cause of this disruption due to the flow circulation can therefore be quantified with a velocity magnitude plot as presented in Figure 4.13. Note the graphical distribution on the bottom right that takes a line probe across the circulatory region, measuring the resulting vorticity magnitude:

The plot presents clear and distinct regions of circulation. Four distinct circulatory loops can be seen in this plot, with two major regions in the bulk of the fluid (or the Schlichting region) and two smaller loops closer to the acoustic source that counter rotate to the larger pair. Findings appear to be in agreement with sources in the literature that suggest that an even number of loops is present. In terms of circulation, Figure 4.15 compares the circulation from vorticity plots for 175 kHz and 325 kHz. Of interest is the simularity in fluid structure between the
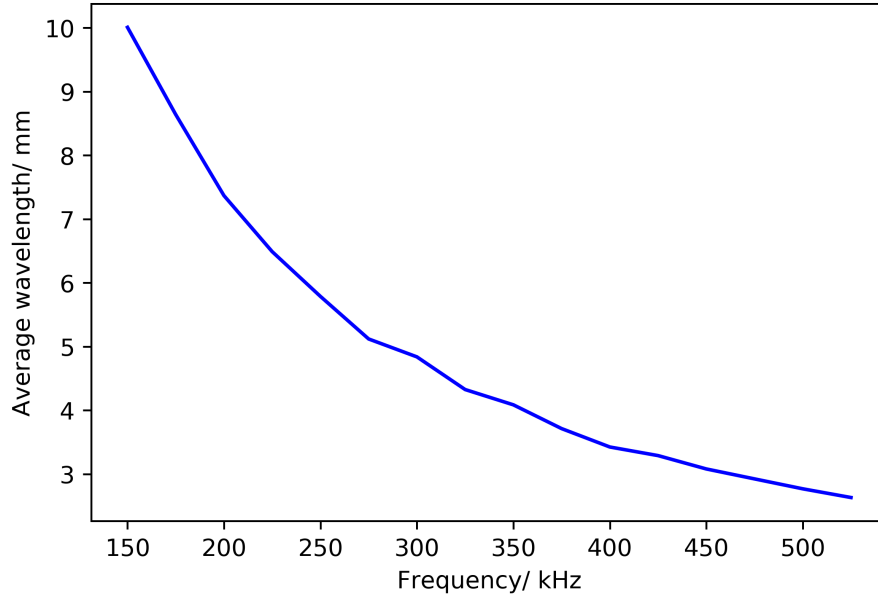
Figure 4.11: Changes in wavelength with frequency.

vorticity plot for 175 kHz and streamline comparison provided by Rahimi et al. [97].
A close-up of the circulatory regions is presented in Figure 4.14. The fluid structure
in terms of vorticity can explain the disruption to the thermal boundary layer as
observed in Figure 4.14.

The surface bound Rayleigh streaming can be clearly be seen, circled in black, in
conjunction with the inner Schlichting streaming marked in red. It can be conjec-
tured that surface bound streaming plays a part in the intermixing of layer within
the thermal boundary layer. In turn, circulation in the Schlichting region can ex-
plain the resulting reduction in free stream temperature within the bulk of the fluid.
Notice that the intensity of the circulation around the Rayleigh region far outweighs
that of the Schlichting layer.

The development of this circulation can be changed for the entire range of fre-
quencies as presented in Figure 4.16 and Figure 4.19. The data falls into two distinct
regions within the vorticity range. Up to 425 kHz, the flow structure is comprised of
two distinct circulatory Schlichting regions. There is a clear indication of an increase
vorticity magnitude across the spectrum for each plot. The flow structure is clearly
evident of the distinct structure of acoustic streaming and fits well with streamline
plots presented by Rahimi et al. [97].

The overall fluid structure between the two frequencies agree well with literature
findings; two major circulatory loops that are observed in similar regions of the
geometry. However, a further two loops have been resolved around the transducer
region for the 175 kHz wave. We also further benefit from a view of how frequency
effects this fundamental flow structure. Here we see that aswell as clear increase in
downward velocity originating from the transducer, an increase from 175 to 325 kHz
also results in the number of major circulatory regions reducing from 4 to 2. Taking
into account Figure 4.11 for wavelength, the following characteristics are presented
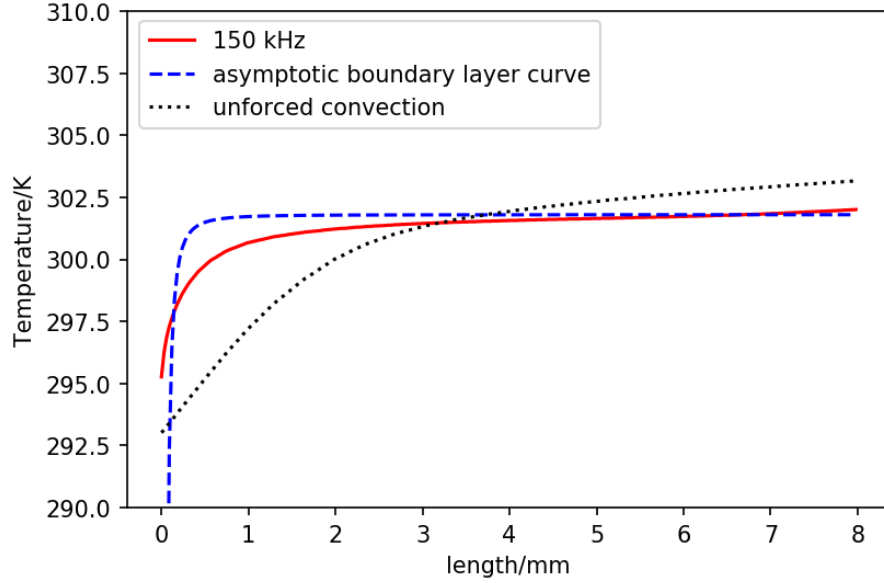
Figure 4.12: Comparisons of the thermal gradient in the bottom wall boundary layer for the base convection case and acoustic streaming at 150 kHz.

in Table 4.3.

Table 4.3: Characteristics of the vortex structure for consecutive wavelengths taken from Figure 4.11.

Frequency (kHz)	Wavelength (mm)	Number of vortical loops
175	8.64	4
325	4.32	2

For these findings, the general consensus of the literature in Section for Chapter 2, along with Figure 2.1 , as previously mentioned is that the change in wavelength influences the number vortical loops in the domain. Specifically, for a domain with a height within the same magnitude of scale of the wavelength, the quantity of loops halves for every time the wavelength also halves. This specific geometry is of much larger scale, and consequentially, the opposite is observed. As per the trend in Figure 4.11, the increase in frequency reduces the wavelength, but what Table 4.3 presents is the reduction in loops as opposed to an increase when the frequency is ramped up from 175 kHz to 325 kHz. Thus, the primary point deduced is the sizable difference in trends between small and large-scale geometries, although both geometry types exhibit the same net effects associated with acoustically driven flow.

At these frequencies, the characteristics of the propagating wave agree with the findings of Tajik et al. [58] for vortical loops. With the ability utilize CFD tools in parallel, several batch simulations can produce data across a wide range of frequencies. Primarily, we can ascertain if at all values across the spectrum, an even quantity of loops is present. We notice that this is the case for additional frequencies as seen in more detail in Figure 4.16. X-component velocity plots are presented
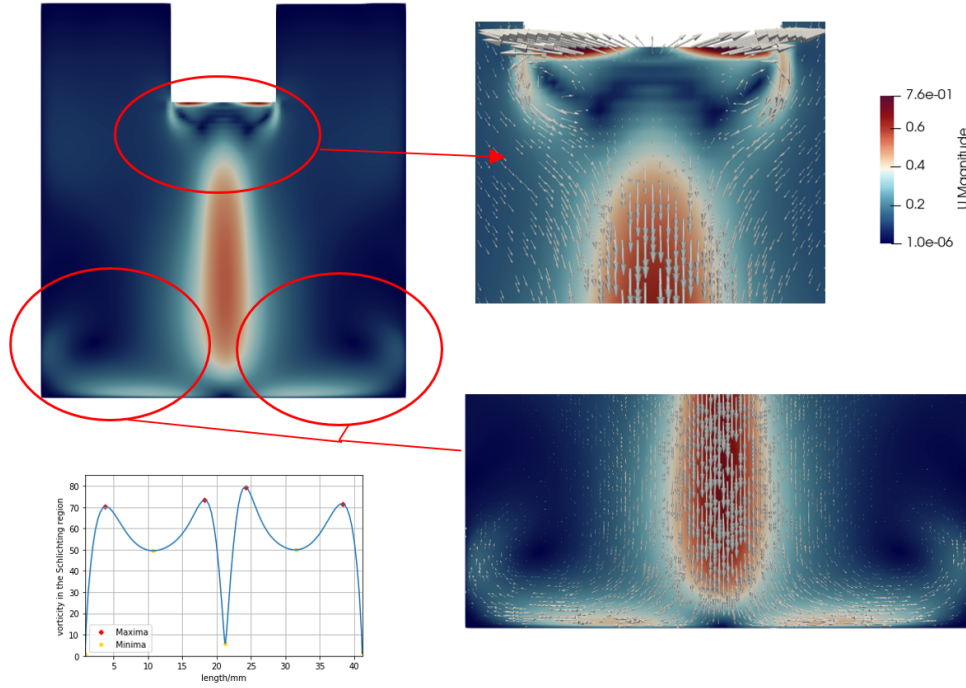
Figure 4.13: (top left) Velocity magnitude contours with data taken horizontally for the resulting vorticity magnitude across the centre of the two regions of circulation for a frequency of 150 kH with close-ups of the vector plots showing the fluid flow direction in two specific areas and (bottom left) the resulting vorticity across the two areas of circulation.

for three frequencies. The vorticity magnitude distribution was subsequently calculated from these as presented in the proceeding figures. The intensity of Rayleigh streaming significantly outweighs that of the inner Schlichting streaming.

The increase in vorticity as seen in Figure 4.17 is evident of the increased intensity of circulation. Corresponding y-velocity component contour plots show increased levels of downwash from frequency to frequency. Nevertheless, the flow structure demonstrates the distinctive behaviour of acoustic streaming, with counter rotating regions of flow and a gradually increasing circulation intensity as the frequency is ramped up. The findings are in agreement with the literature. Recall that Talebi et al. [76] established correlation between velocity and vortex intensity. They also noted that with this increase came a greater degree of thermal mixing. Again we can correlate this by presenting the effect on temperature distribution in Figure 4.18.

The increase in frequency results in a net cooling across the entire domain. The wall-bounded thermal boundary layers observed in Figure 4.18a appear to break down across the temperature plots thus clarifying that the thermal mixing results in a net cooling effect and further backs the findings by Talebi et al. [76]. Moreover, velocity magnitudes in Figure 4.16, particularly for x-component velocity increase with frequency thus indicating greater circulation intensity. This trend correlates well with the disintegration of the thermal boundary layer in Figure 4.18 thus in-
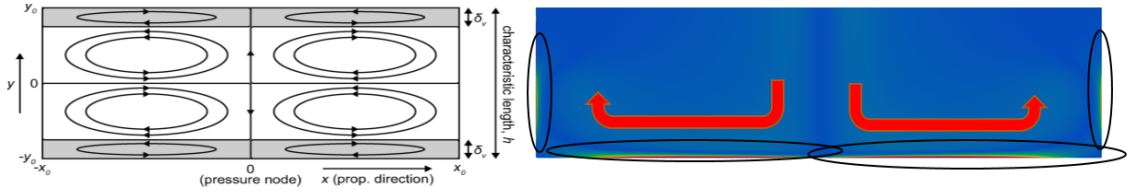
Figure 4.14: A closeup of the flow structure showing outer Rayleigh streaming in the Stokes boundary layer and inner Schlichting streaming in the bulk of the fluid.

dicating that the intensity of circulation has a net profound effect on boundary thickness.

Beyond 425 kHz, the flow structure changes significantly. Figure 4.16 demonstrates a gradual recession of the downward component of fluid movement as seen in the plots for y-component velocity. Overall, what is shown in actuality is that the flow breaks down into four vortical loops that are counter-rotating. The resulting vorticity data corresponds well with this, with much of the vorticity concentrated around the acoustic source as demonstrated in Figure 4.19.

For this, we must refer back to discussions made for Figure 4.17. Recall that it was discussed that the trend for larger scale geometries in the context of loop number and wavelength was the opposite of what was observed for smaller scale geometries as presented in the literature for authors such as Tajik et al. [58]. Figure 4.20 only confirms this observation with the increase in vortical loops across the frequency range. Of further note is the decline in intensity of the Schlichting loops, with Rayleigh bounded streaming appearing to disintegrate completely after the 425 kHz mark.

These loops appear to recede, with gradually reduced distance to the surface of the acoustic source as frequency further increases to the point where 500 kHz is reached and the flow structure is reduced to significant vorticity around the circulation of the transducer and forming several distinctive vertical loops at this point. All the while, it is evident that overall vorticity magnitude increases. It is also worth noting the increasing regions of vorticity across the acoustic transducer surface corresponding to the maximum pressure amplitude closest to this region, indicating the importance of pressure amplitude on circulation. Again section 2.3 of Chapter 2 highlights findings by Setareh et al. [69] showing correlations between stronger circulations and acoustic pressure.

With this in mind, the maximum vorticity was measured across the streaming fluid structure for each frequency. Recap the graphical distribution in Figure 4.13. A code in python was written to deduce the maximum peaks across the line probe that was taken across the geometry. The maximum and minimum points were subsequently deduced as indicated in Figure 4.13. This was done for both Rayleigh Streaming and for Schlichting streaming. The maximum points were then used to calculate an average value for each frequency. The overall behaviour of the vorticity could then be quantified as indicated in Figure 4.21 and Figure 4.22.

General magnitude of vorticity in Rayleigh streaming is seen to be larger than
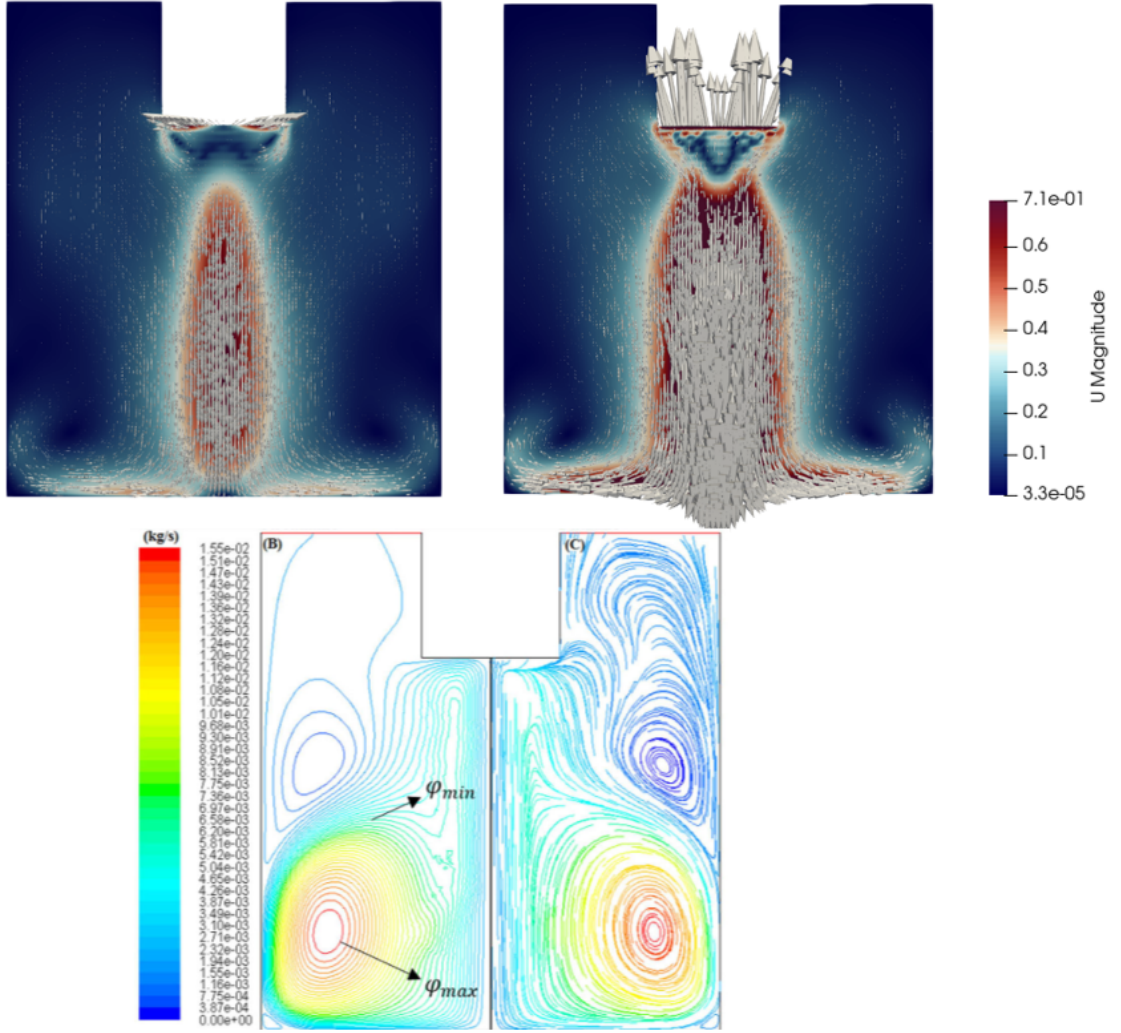
Figure 4.15: (above) velocity vector plots for (left) 175 kHz and (right) 325 kHz in comparison with streamline plots presented by Rahimi et al. [97] in units of mass flow rate.

that of Schlichting. Moreover, shape development between different frequencies is far more stable as seen in Figure 4.21a. Figure 4.22 corresponds to the contour plots in Figure 4.20 where past the 450 kHz mark, the uniform and symmetrical cohesion in the circulation profile breaks down. That being said, the change in vorticity within the Rayleigh region is far less uniform compared to that of the Schlichting region. Referring back to Figure 4.22, an exponential trend is seen. Furthermore, looking at the data points individually, the rapid increase in magnitude coincides with sudden change in fluid structure observed at 450 kHz. Prior to this, the change from frequency to frequency is uniform and proportional corresponding to the characteristic flow structure observed in Figure 4.17 and 4.20 where contour plots fit well with those in the literature. This is also evident in Figure 4.22 where the vorticity profiles are initially of a cohesive and parabolic profile before developing into random
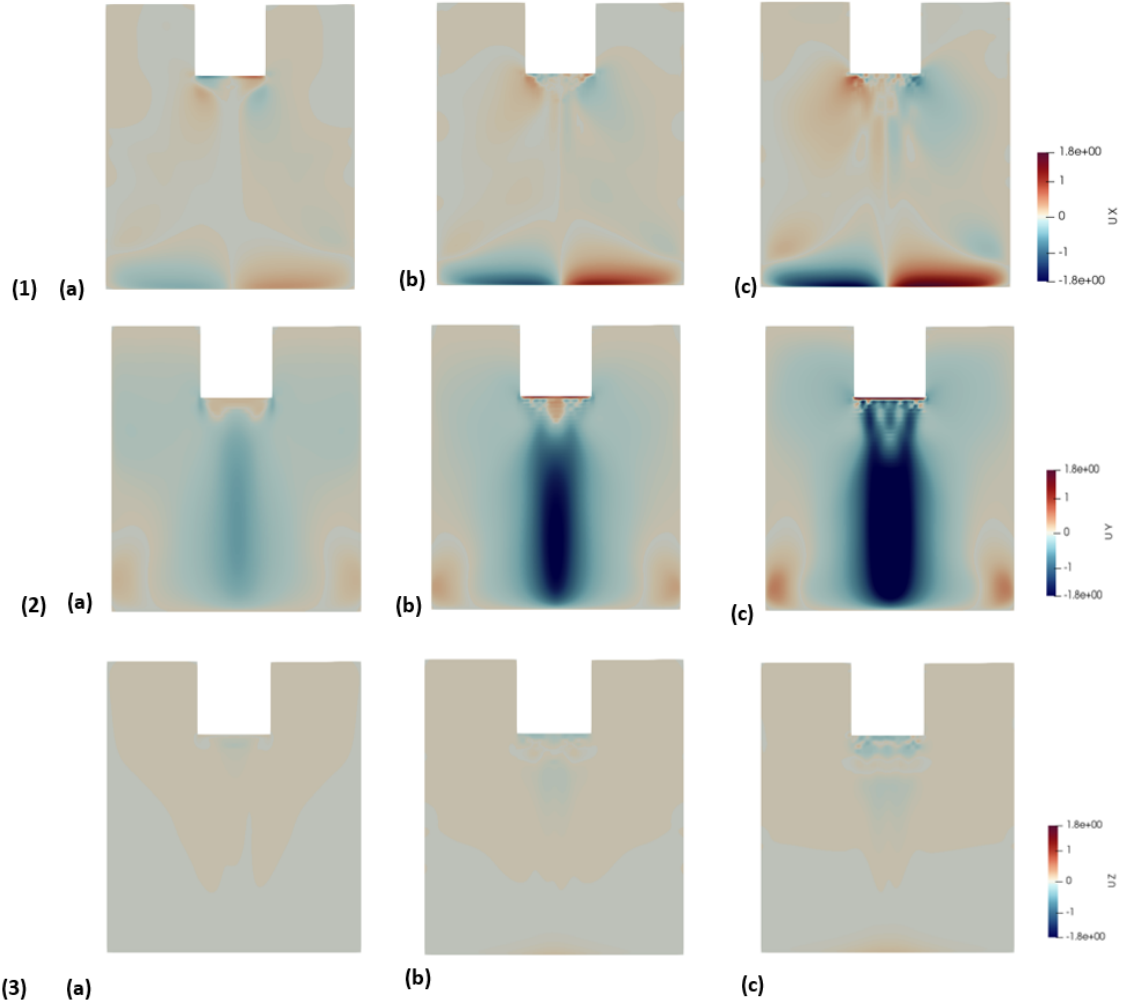
Figure 4.16: Velocity contours for (1) x-component, (2), y-component, and (3) z-component for (a) 175 kHz, (b) 325 kHz, and (c) 425 kHz.

fluctuating peaks. The explanation behind this behaviour is geometry dependant. A dramatic change in behaviour past 475 kHz is demonstrated in Figure 4.22. The explanation behind this change can be attributed to the wave behaviour. At a critical frequency, the extent of the wave dispersion is enough to induce reflection as the wave front makes contact with the domain wall boundaries. The resulting congregation of rays is enough to result in smaller and more localised eddies as demonstrated in Figure 4.22. The value of this critical frequency is geometry dependent. The larger the geometry domain, the larger the critical frequency due to the increased distance of propagation and subsequent reflection. There is room here for potential further work to study the effects of geometrical parameters on this critical frequency which will be outlined in Chapter 7.

The next logical stage was then to ascertain the effects on the thermal boundary layer. Recall that Figure 4.12 presents the temperature profile for a 150 kHz frequency. Figure 4.18 also provides us with a window into the changes in tempera-
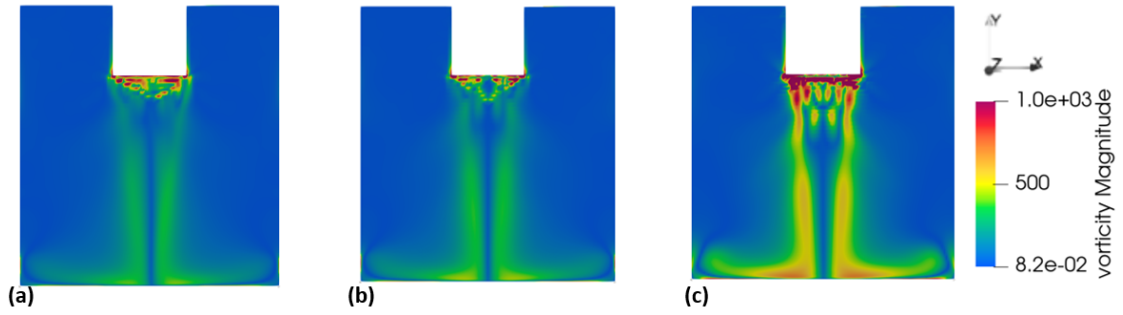
Figure 4.17: Vorticiy distributions showing the distinctive acoustic streaming and the resulting effects on vorticity magnitude for (a)175 kHz (b) 325 kHx (c) 425 kHz.
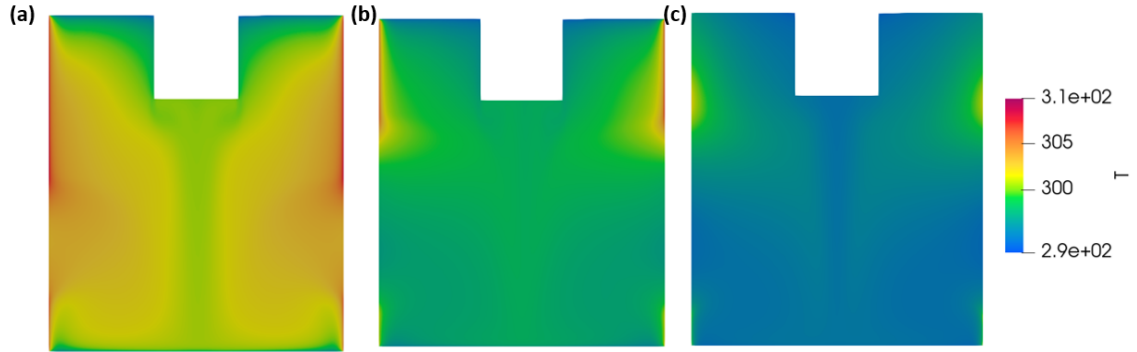
Figure 4.18: Temperature contours for (a) 175 kHz, (b) 225 kHz and (c) 325 kHz.

ture distribution across three different frequencies. However it does not provide us with any quantitative indications of the structural changes in the boundary layers present. Again, recall from Chapter 2 that there exists a significant gap of knowledge in the literature in this regard. Figure 4.23 presents an array of temperatures profiles for the entire frequency range compared to the base convection case.

The effect on the shape of the thermal boundary layer is evident. The distributions correspond well with Figure 4.22. There is clear correlation between the level of disruption in the boundary layer and the magnitude of maximum vorticity; with values of vorticity upwards of 400 kHz where the trend line undergoes a significant increase corresponding with complete disruption of the standardised temperature profiles. It is clear from Figure 4.23 that complete thermal mixing occurs around the 450 kHz mark. It is also worth noting the general reduction in average temperature across each thermal boundary layer profile as frequency increases thus providing an indication of the effects of frequency on heat transfer and further solidifying the findings made by Talebi et al. [76]. The near total collapse of the thermal boundary layer at 400 kHz corresponds well with Figure 4.22 where the rate of increase in max vorticity between frequencies begins to increase significantly. It is also worth noting that the following frequency at 450 kHz is where the acoustic streaming flow structure becomes drastically altered as identified from Figure's 4.19 to 4.20. Thus
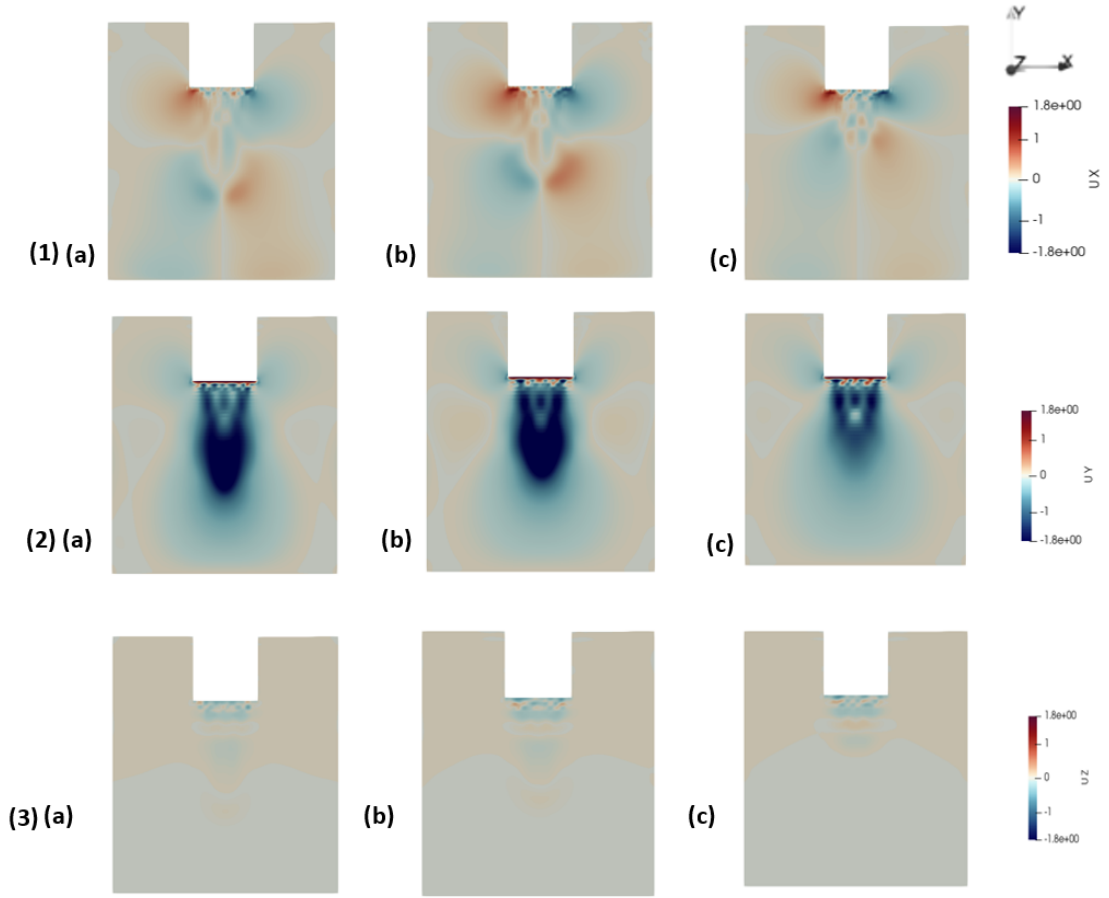
Figure 4.19: Velocity contours for (1) x-component, (2), y-component, and (3) z-component for (a) 450 kHz, (b) 491 kHz, and (c) 500 kHz.

the direct correlation between flow structure and circulation on thermal boundary layer development between frequencies can clearly be seen. The findings are thus in agreement with literature.

In order to quantify this, python, a programming language and tool was used to calculate a value that represented the level of mixing within the boundary layer by comparing the temperature curves of both the acoustic flow and the base convection for each frequency. This was done for all boundary layers up to 375 kHz before the resulting circulation induced a complete collapse of the temperature profiles from this point onwards. The value provided for each frequencies was calculated by the percentage difference of the magnitude between the integral values between both curves and provided a quantifiable way of assessing the degree of mixing in the thermal boundary layer for each frequency. To describe this, a temperature profile in acoustic flow verses a standard temperature profile in unforced convection for the same geometry and flow conditions should be considered as shown in Figure 4.24. The code measures the area under each curve by integrating across the profile bounds. A difference is then calculated and python subsequently outputs a magnitude value of that difference. Thus throughout this thesis, similar calculations are
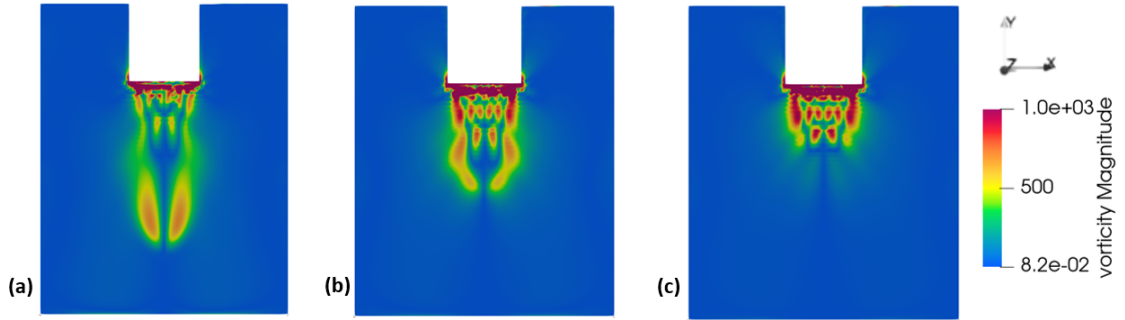
Figure 4.20: vorticity magnitude distributions showing the changes to the fluid structure beyond 450 kHz for (a) 450 kHz (b) 491 kHz and (c) 500 kHz.
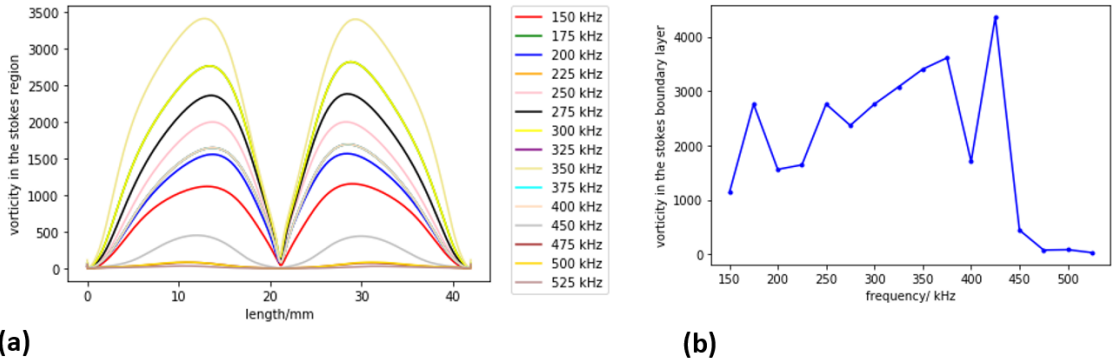
Figure 4.21: (a) vorticity magnitude distributions for the surface bound Rayleigh streaming on the bottom wall and (b) the respective peak vorticity calculated using python.

carried out in the following chapters. It should be noted that the terms intergral and curve area are used interchangeably however both denote the same calculation. The significant behind this calculation is due to the ability to quantify the effect that acoustic flow has on the boundary layer- the larger the magnitude value, the larger change in the temperature profile in an acoustic flow compared to standard unforced convection.

This is shown in Figure 4.25 and comparing this with Figure 4.22, the correlation is evident. A linear increase in mixing corresponds to the linear increase in maximum vorticity within the Schlichting region of the flow. The findings highlight how the magnitude of circulation plays a major role in structure of the thermal boundary layer.

The size of these boundary layers was subsequently measured by using an asymptotic calculation in python as demonstrated in Figure 4.26 for 200 kHz.

Here, python was able to deduce a rational polynomial function for the computational data and output a vertical asymptotic value for temperature, which was then looped to output a height value for which the temperature was associated. In this way we were able to obtain an effective value for thickness. This boundary layer
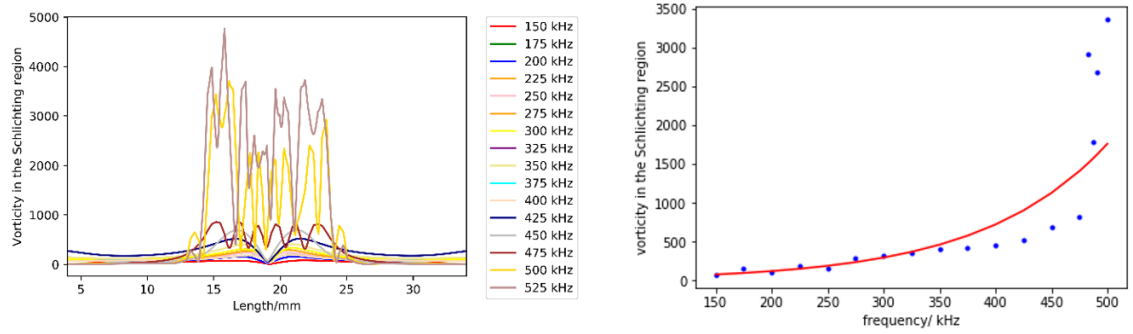
Figure 4.22: (left) vorticity magnitude distributions for the inner Schlichting streaming and (right) the respective peak vorticity calculated using python.
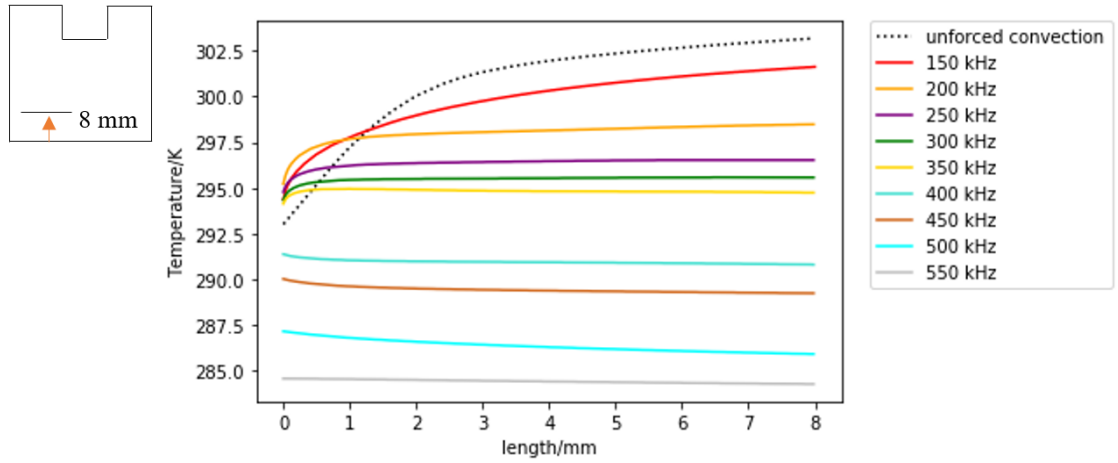
Figure 4.23: Temperature profiles from thermal boundary layers for all frequencies.

thickness distribution is presented in Figure 4.27.

It can be seen that the exponential decrease follows very closely with the changes in wavelength as seen in Figure 4.11. It can be seen that the effect of mixing has the effect of reducing the boundary layer thickness due to the intermixing of thermal layers between the fluids thus presenting the mechanism of how heat transfer is improved and adding further grounding to literature provided by Setareh et al. [69].

To ascertain a further view of boundary layer behaviour, a further horizontal line probe was taken 35 mm from the base. In effect, a boundary layer from the sidewall as opposed to bottom was measured as indicated from the schematic in Figure 4.28. The temperature gradients for each frequency are presented in Figure 4.28. It can be seen that the increase in frequency has the same effect on a boundary layer at a different location. The effect of mixing is seen to decrease temperatures seen in the bulk of the fluid.
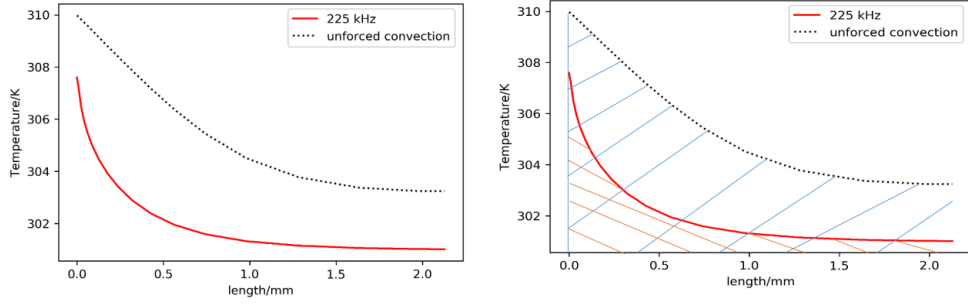
Figure 4.24: An explanation of the intergral calculation, the cross-hatching represent the area under each curve that is calculated by intergrating across it.
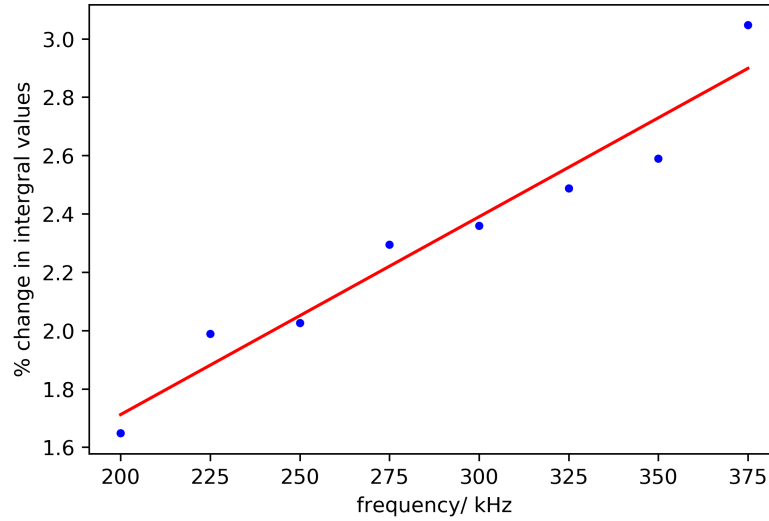
Figure 4.25: The effects of frequency on the level of mixing in the bottom boundary layer.

4.6   Summary

Chapter 2 concluded with the need to establish a more focused parameterisation study for changes in aspects of streaming such as temperature distribution and boundary layer thickness. Chapter 4 provides fundamental grounding for the findings in the literature. What has been established and clarified is that wavelength plays a fundamental part in a significant amount of studies conducted in this chapter. We should look to the likes of Figure's 4.11 and 4.27 for correlations that convey such a trend thus the findings agree with the likes of Landau and Lifshitz [56] in that wavelength plays a role in boundary layer thickness. Nevertheless, it is interesting to note the difference in effects between small-scale geometries (as noted in the literature review) and a large-scale geometry such as the domain in question for Chapter 3. Here, it is observed that the increase in frequency reduces the number of loops as opposed to increasing them. Furthermore, we are able to observe direct correlation between vorticity, velocity and circulation, thus clarifying findings from
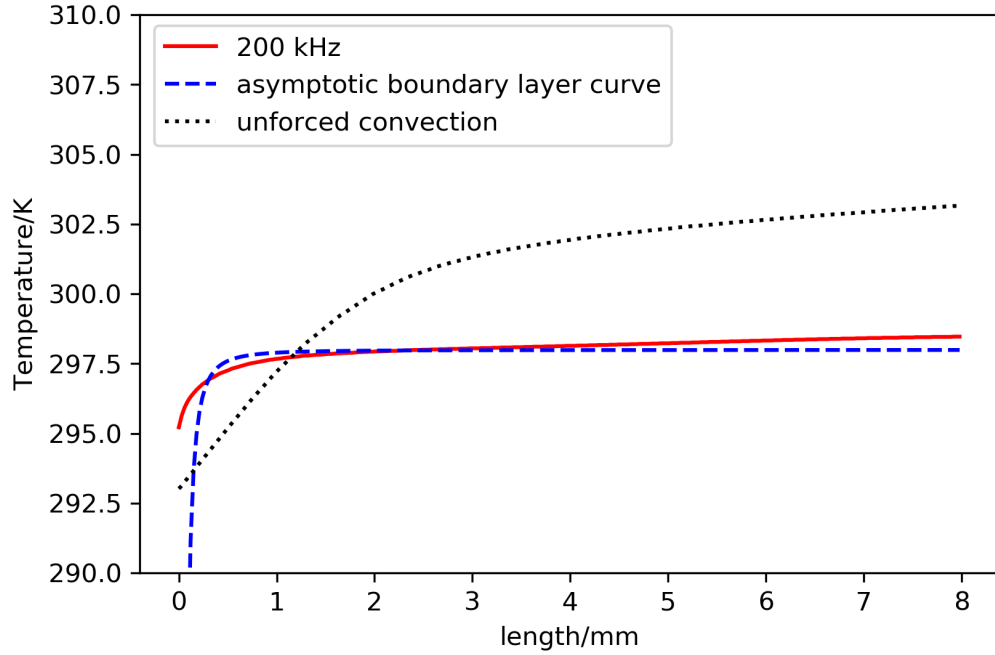
Figure 4.26: An example of how an asymptotic approximation on the thermal boundary layer distribution (200 kHz).

Talebi et al. [76].

Fundamentally however, the work adds significantly to the bulk literature by providing an incremental study of frequency over a significant range and the changes associated with it. Recall the model was successful in being able to resolve and break down the circulation components associated with wall-bounded Rayleigh Streaming, and also bulk streaming in the Schlichting layer as emphasised in Section 4.5 of the literature. Chapter 2 is able to build on this by providing an overview of the changes in the Schlichting vorticity across the frequency range. Through this, we gauge a clearer understanding of acoustic streaming by observing its behaviour across said range. In particular, referring back to Figure 4.22 for reference sake, the vorticity in the Schlichting layer is seen to initially undergo a proportionate increase with frequency. Additionally, the distribution is marked by a sudden increase at the 450 kHz mark that corresponds with contour observations that convey a breakdown in the symmetry of the flow structure at this point. For this, we should also refer back to Figure 4.23 to observe the development in temperature distribution. Here we notice that the boundary layer structure completely breaks down past the 450 kHz mark. Thus, it can be postulated that vorticity and thermal boundary layer structure possess correlations between each other. Of additional importance is the capability of the model to produce visualisations of the changes to the flow structure across the frequency range. Figure's 4.16 and 4.19 present this nicely. The general trend splits the behaviour across the two halves of the frequency range, with the lower end (100 to 325 kHz) showing streaming in the Schlichting layer. This layer lies primarily adjacent to the bottom wall and we observe that the circulation size increases with
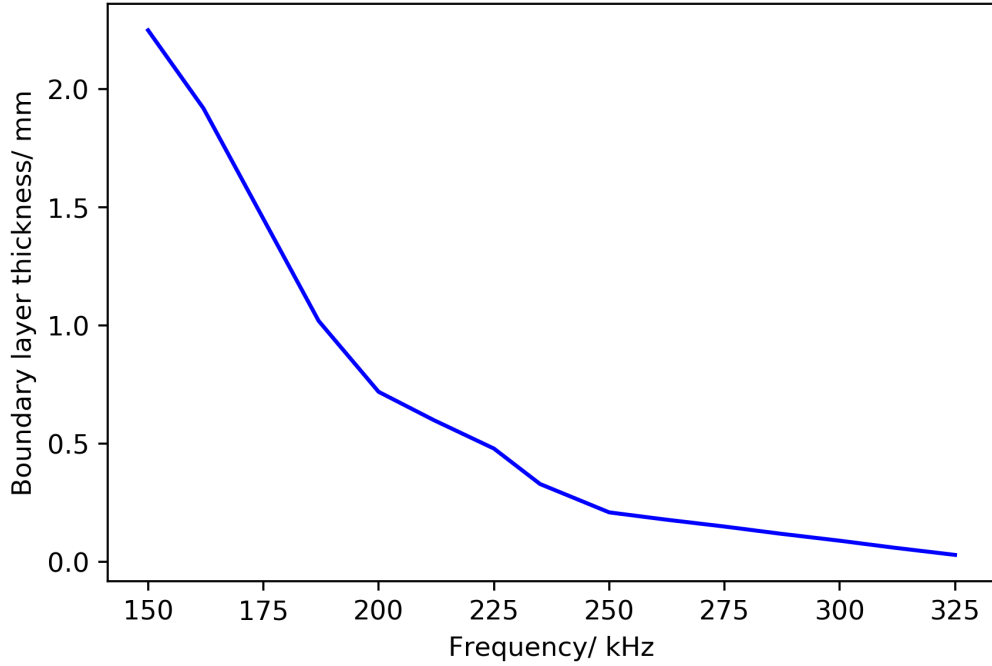
Figure 4.27: Boundary Layer thickness vs frequency.

frequency. Fand and Kaye [61] and Wan and Kuznetsov [60] noted correlations between acoustic intensity and circulation size- but up to a point. Relating this back to the current work, we notice that contour distribution for the second half of the frequency range present a completely different flow structure, with multiple loops. Furthermore, as with Wang and Kutnetsov [60] who identified a critical size where circulation size became independent of intensity, it appears that the increase in frequency bares little influence on the circulation size of the loops in Figure 4.19. What we do notice is that the vorticity still undergoes a sudden increase, thus it can be stipulated that vortex magnitude is not effected by circulation size.

There are areas that can be further developed within this scope. The thermal boundary layer thickness was the primary quantity of study. The question is whether this can be applied to a velocity boundary layer thickness. The reason why this was not studied was because the bulk of the fluid was essentially quiescent at initial conditions, thus the study of any velocity boundary layer would be extremely difficult to study unless a flow rate was applied. Again it is important to highlight findings by Zhang [66] who found that the circulation broke down with any resulting flow rate, therefore calibrating a flow rate whilst maintaining the circulatory structure itself would be a challenging and computationally expensive task. Nevertheless, as will be discussed in Chapter 7, the potential findings could be important for microfluidics if flow rates were seen to improve cooling effects for electronics.

To conclude the chapter, the results agree with the literature in that velocity and vorticity are key components in the effect on boundary layer thickness. Moreover, the magnitude of frequency has clear effects on the positioning of circulation, and to an extent on its size. Moreover, in the context of heat transfer enhancement,
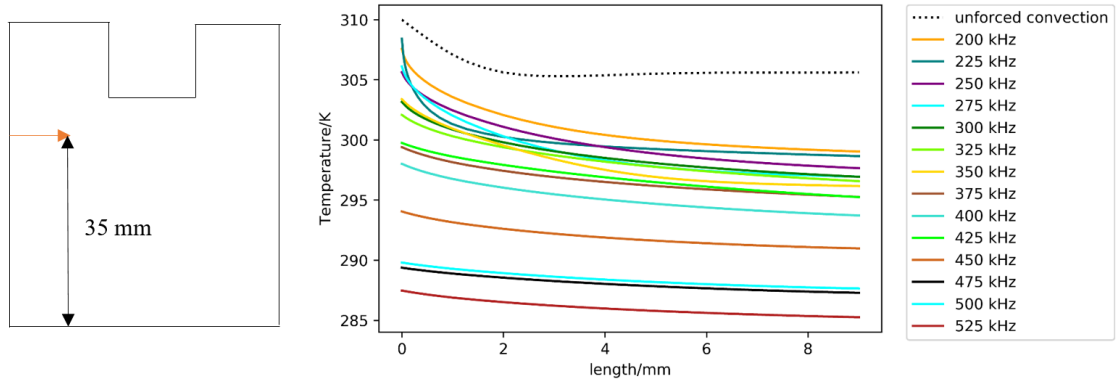
Figure 4.28: Temperature gradients for a horizontal line probe taken 35 mm from the base as demonstrated in the associated schematic.

the effects of frequency are clear; Figure 4.18 presents a net decrease in average temperature that correlates with a net increase in frequency. The net effect is that thermal mixing, which in turn causes the breakdown of wall-bounded thermal boundary layers, causes a net cooling effect that increases with frequency.

Finishing off the chapter, it is worth noting that the data presents a steady state solution of the frequencies- thus showing mean global effects across the domain for each case. In terms of parameterisation, we are not shown the instantaneous changes in the fluid structure with respect to time. For this, we should refer back to the summary in Section 2.11 of Chapter 2. Whilst, we are presented the global effects for each frequency, there is no distinction between parameters that exhibit stationary behaviour and parameters that are in flux. This leads us to Chapter 5, where observing the dynamic behaviour of the flow provides us with a window into how specific parameters change with time.

CHAPTER 5

DYNAMIC BEHAVIOUR OF ACOUSTICALLY DRIVEN FLOWS

5.1 Introduction

Having ascertained the effects on the changes to a thermal boundary layer structure over a wide range of frequencies, the logical next stage is to identify the development of the flow structure across time for the same closed fluid domain. Two frequencies from the previous chapter were chosen with a run time of 2.25×10^{-5} s. The pressure signal for a point near the pressure transducer is presented in Figure 5.1 and 5.2
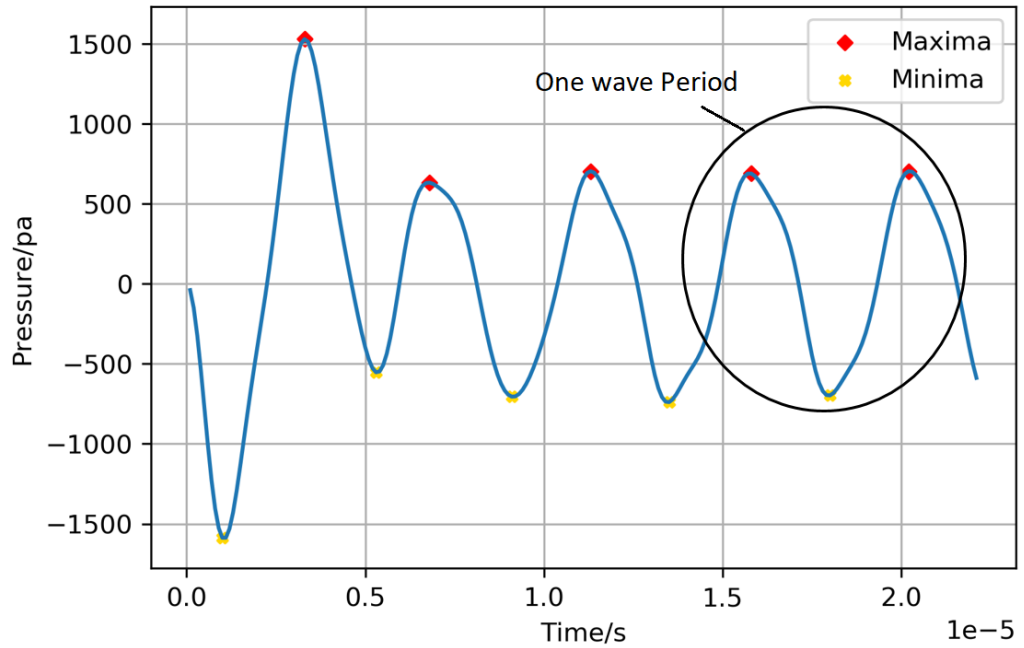
Figure 5.1: A graph to show the pressure signal for a 225 kHz frequency, the circled pressure peaks indicate one wave period where steady state has been reached, presented in Figure 5.3.
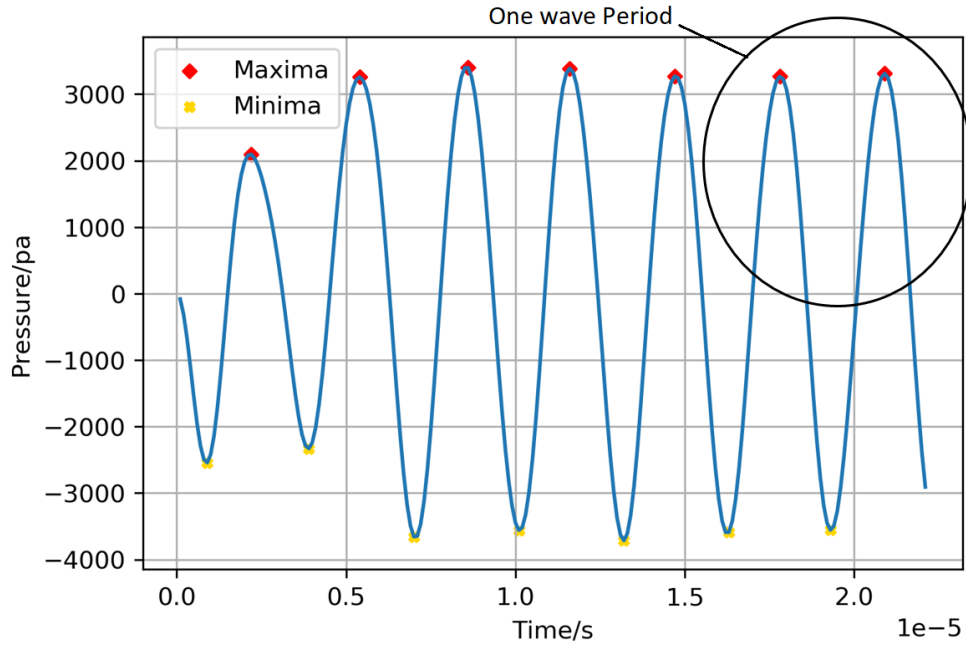
Figure 5.2: A graph to show the pressure signal for a 325 kHz frequency, again showing circled pressure peaks in one wave period where steady state has been reached.

The plots are interesting in that they show the changes in peak amplitude marked by maxima's between the two frequencies, along with changes in the distribution of the wavelength. The figures provide a qualitative window into the changes seen in figure 11. A principle observation is that an increase in frequency-as demonstrated in Figure 4.11- results in a reduction of the wavelength. For one wave period in each frequency, as marked in Figure 5.2, the instantaneous variations were modelled across this region. Thus the flow structure variation across time was modelled for one period.

The determination of a steady state solution has not been discussed in depth in this thesis. We have talked within the context of a steady state model converged from a time step for a given wave propagation but the nature of the flow through run time has yet to be touched upon.

In Figure 5.1, we refer to the final two pressure peaks (circled) indicating the oscillation of one full wave period. The velocity distributions for both points in time are presented in Figure 5.3

We notice that the distribution is marginally the same. No overtly apparent changes are visible, and the fluid bulk maintains its overall fluid structure. In essence it can be deduced that the fluid has reached a steady-state (albeit, at this point the wave propagation has caused minimal reflectance of the side walls as shown in Figure 4.10. The shape of the curves also backs the evidence in Figure 5.1 and Figure 5.2. The pressure oscillations- after a certain time- even out after attenuation, leading to uniform values of peaks and troughs.

However, what this does not tell us is the nature of the flow behaviour between
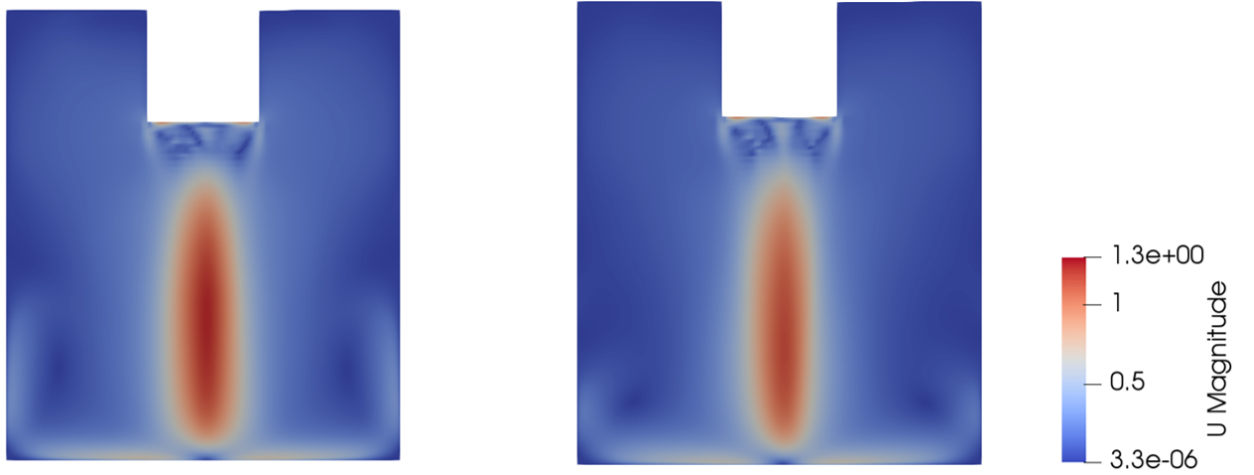
Figure 5.3: Velocity distributions at pressure oscillatory peaks representing one wave period. (left) 1.6×10^{-5} and (right) 2.02×10^{-5}.

these peaks and consequentially, the following questions arise: What happens to the fluid flow across one wave period? Moreover, what is the effect of one oscillation for a fluid in steady state on the change in shape in the boundary layer?

We know for certain that with overall run time, the temperature distribution of a flow will undergo a net change but we don't know the nature of the dynamic variation of fluid quantities such as acoustic force, temperature or thermal mixing. Thus the following chapter presents a detailed time study across one period for two frequencies; 225 kHz and 325 Khz as presented in Figure 5.1 and Figure 5.2.

5.2 Results and Discussion

Figure 5.4 is a study of the temperature distribution at incremental values in the period for an oscillating 225 kHz wave. Table 5.1 corresponds each plot from Figure 5.4 to the appropriate time.

Table 5.1: Corresponding times for each plot in Figure 5.4.

Figure	Time/ 10^{-5} (s)
a	1.6
b	1.67
c	1.74
d	1.81
e	1.88
f	2.02

Figure 5.4 presents a clear indicator of the effects of time and wave propagation on thermal mixing. The overall trend can be divided into two sub-trends that can be split across either side of the anti-node minima marked in Figure 5.1. Figure
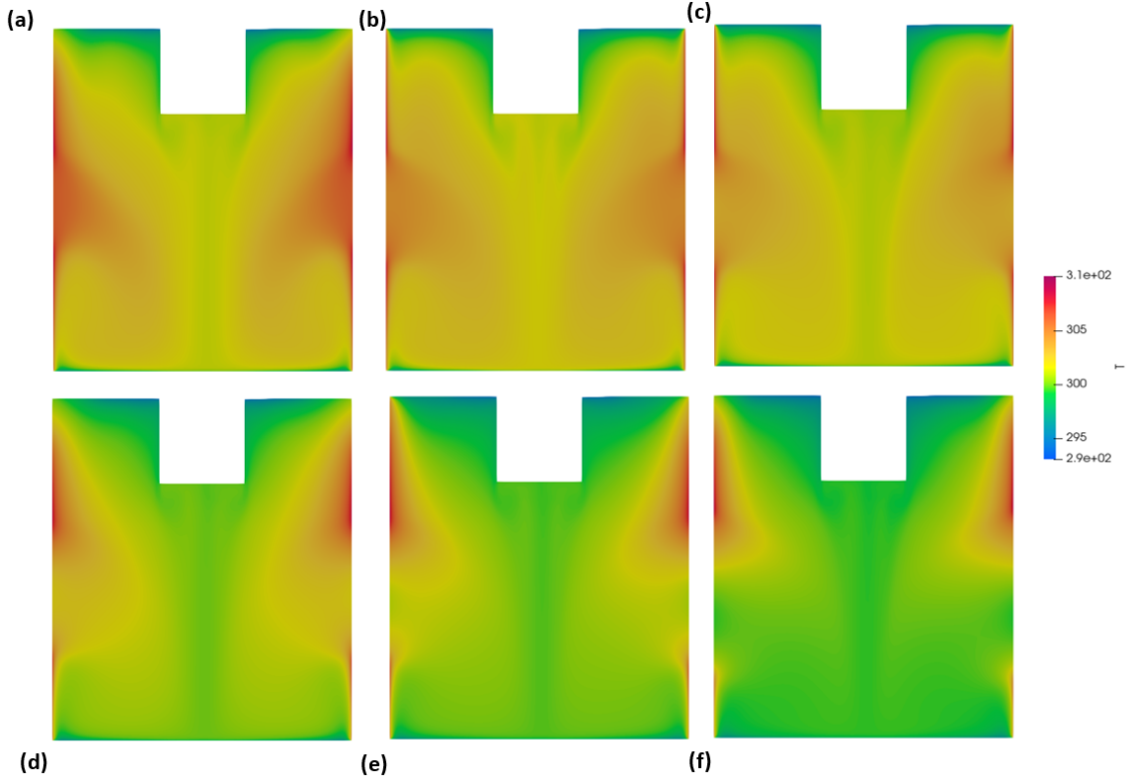
Figure 5.4: Instantaneous temperature distributions within a single period for a 225 kHz wave.

5.4a through to Figure 5.4c (on the left side of the anti-node) present a uniform temperature distribution across all time steps whilst Figure 5.4d through to Figure 5.4f present a shift in the scale of magnitude in the temperature distribution whilst maintaining a uniformity across all time steps. The outline of the fluid structure across the period stays marginally the same however there is a net decrease in overall bulk temperature as we traverse the wave period. It is interesting to note that the coldest temperature's on the left side of the anti-node lie along the geometry's axis of symmetry as presented in Figure 5.4a through to Figure 5.4b. They correspond well with maximum velocity seen at this region in figure 5.3 as a consequence of the wave motion down the axis of symmetry. This " shaft" of cold fluid appears to undergo a net expansion in width as is evident in plots a through to c. This expansion undergoes a rapid decrease as the right side of the antinode is reached. The trend indicates the mechanism behind ultrasound enhanced heat transfer in that a greater distribution of cold floor is seen as a result of acoustically enhanced mixing.

Presented in Figure 5.5 is the same distribution for a 325 kHz wave. Again, Table 5.2 corresponds each plot from Figure 5.5 to the appropriate time.

The effects of enhanced cooling with a larger frequency is evident here. The scale of magnitude across the entire period is lower in general. This said, the effects of wave propagation with respect to time is significantly less pronounced. All plots
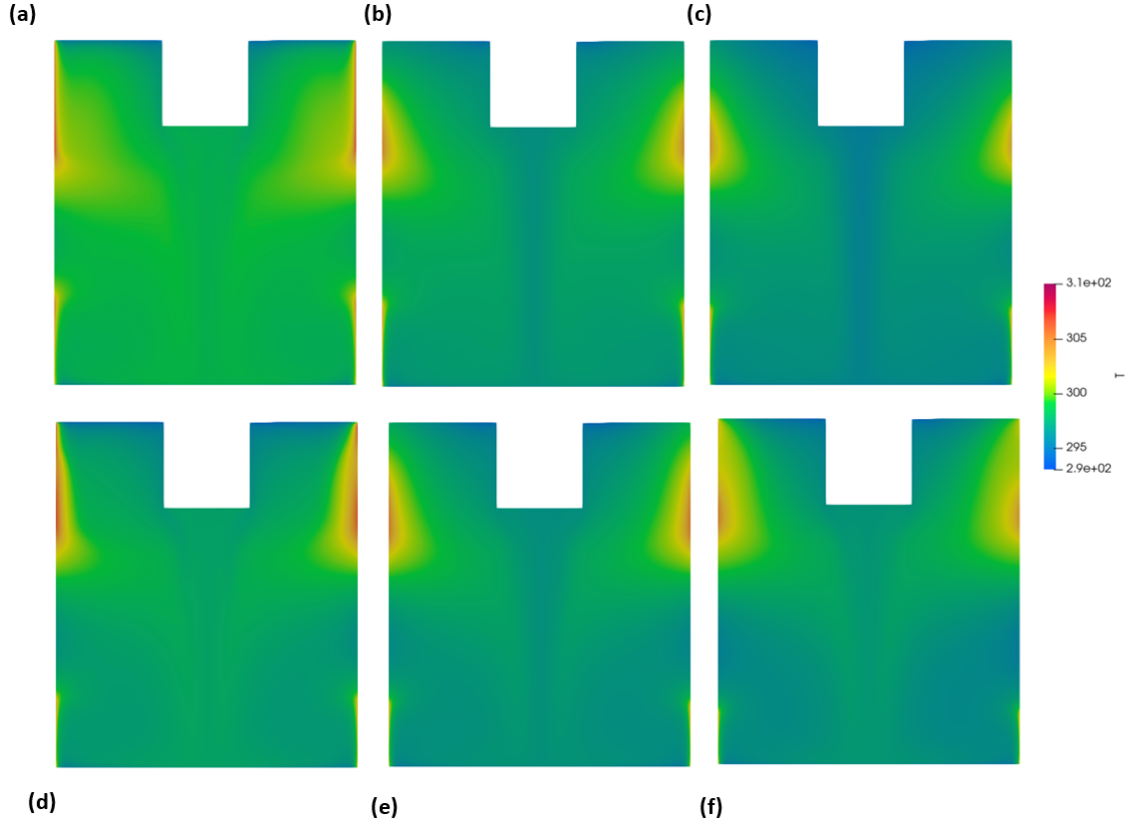
Figure 5.5: Instantaneous temperature distributions within a single period for a 325 kHz wave.

show a larger degree of uniformity compared to Figure 5.1. The change in net cooling is less prominent and thus the indication of thermal mixing as the wave propagates is less prominent. At first glance- and taking Chapter 4 into account, it appears that whilst the effects of instantaneous thermal mixing for a steady-state solution are more pronounced with a higher frequency, the net mixing observed with respect to time for one period is far less for a higher frequency compared to any steady state solutions observed in chapter 4. Referring back to Figure 4.25 , where the change in curve area for a thermal boundary layer with and without the effect of acoustically forced convection was modelled, the same technique was therefore subsequently used to make a study across time instead of frequency. Figure 5.7 present the temperature distribution at 4 different time instances for the wave period as highlighted in Figure 5.2 (see Table 5.2 for Figure 5.5 for corresponding time steps).
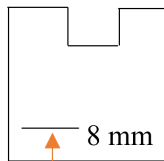
Figure 5.6: corresponding line probe for Figure 5.7.

Table 5.2: Corresponding times for each plot in Figure 5.5.

Figure	Time/ 10^{-5} (s)
a	1.8
b	1.85
c	1.9
d	1.94
e	1.99
f	2.09
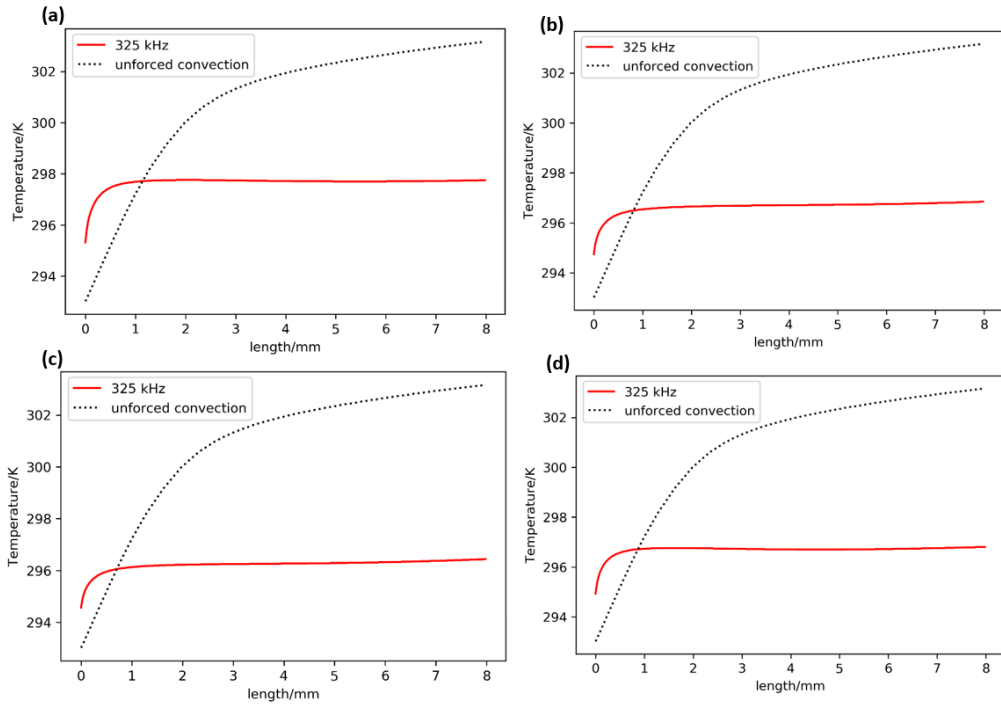
Figure 5.7: Thermal boundary layer profiles for different time steps in a 325 kHz wave period.

At first glance, it appears that in general the profile of the thermal boundary layer remains unchanged. However, taking a look at the difference in area between the two curves for each time step paints a rather different picture. Figure 5.8 presents values for this area difference across all time steps in the chosen wave period. A distinctive graphical shape is evident, showing a characteristic expansion and contraction of the distinctive thermal boundary layer shape. Of interest, is the fact that over time, the overall size of the boundary layer undergoes a net decrease as indicated by the net increase in area difference between the two curves. The findings correspond with the observation that the increased time given to allow for wave propagation results in an overall net cooling effect. This is evidenced by the net contraction of the thermal boundary layer profile as presented in Figure 5.8.

The reduction in frequency paints a different picture however. A look at the equivalent plot for a 225 kHz wave shows slight variations in the periodic trend as
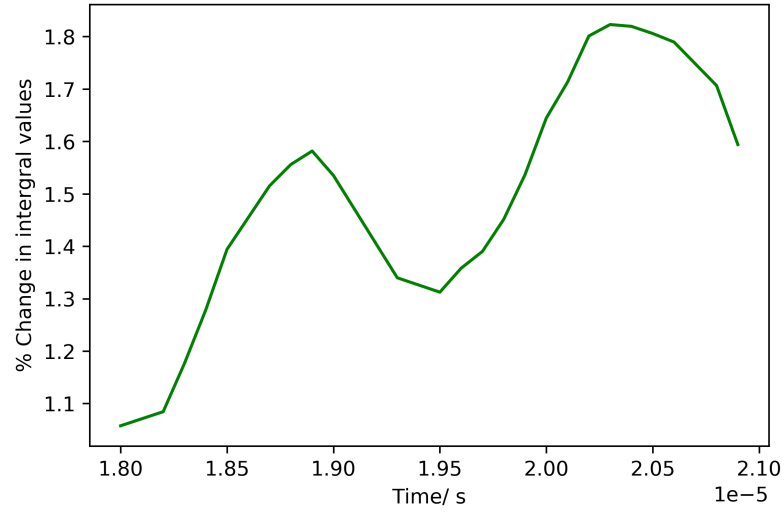
Figure 5.8: Effects on the thermal boundary layer profile across one period for a 325 kHz wave.

presented in Figure 5.9.
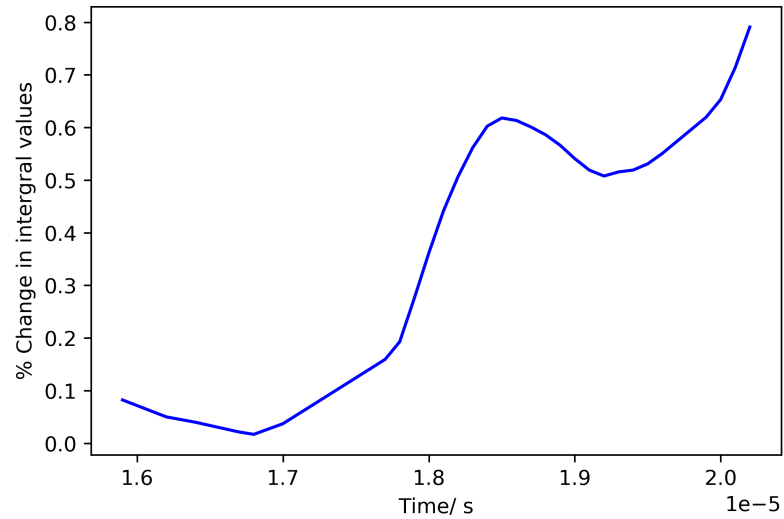
Figure 5.9: Effects on the thermal boundary layer profile across one period for a 225 kHz wave.

The oscillatory effects of an expanding and contracting temperature profile are less prominent here. Overall, the trend tend towards a slightly more coherent increase in thermal mixing, characterised by a general reduction in size of the thermal boundary layer. This finding corresponds well with observations made between Figure 5.4 and Figure 5.5. Recall that in Figure 5.4 a net expansion in cold fluid originating at the axis of symmetry is seen to increase across the noted time steps. The effects are characterised in the changes to the observed boundary layer profile in Figure 4.26 albeit for 225 kHz instead of 200 kHz. A net increase in cold fluid

disrupts the temperature profile, albeit the effects are not linear. The data still fluctuates from a potential proportionate trend. This can be attributed to the oscillatory nature of the flow. The characteristic considerably more evident in Figure 5.8, where distinctive peaks can be identified. It is also interesting to note the scale of magnitude of values between Figure 5.8 and Figure 5.9, with the latter demonstrating lower values. Again this can be attributed to the steady-state nature of both flows. Based on the plots presented in Figure 41 and the oscillatory nature of Figure 43, it could be postulated that a 325 kHz wave has reached a higher degree of steady state. This is further emphasised by the fact that the scale of magnitude of values in Figure 5.8 are larger than Figure 5.9. Focusing on Figure 5.8, if we were to extrapolate the behaviour of the curve beyond the presented run time, it could be argued that we would observe less of a net increase and more of a characteristic trend that tends towards oscillatory fluctuations, that is of course until reflection takes place on the domain walls. On the other hand, Figure 5.9 indicates that further stabilisation needs to take place. Again, extrapolating beyond the presented run time, we would expect the net increase to level out and oscillatory characteristics to take hold. As mentioned previously, the net increase observed in Figure 5.9 corresponds well with the increased cooling observed in Figure 5.4. With the levelling out of the curve in Figure 5.9, we would expect the temperature plots to be considerably similar in comparison to Figure 5.5. To summarise the above, what is clear is that the size of frequency has an effect on the rate of cooling and subsequent stabilisation/steady-state nature of the flow. Based on this, it can be presumed that for 325 kHz, for periods taken prior to the selected, the development of the temperature profile would very similar to that of Figure 5.8 with less of a prevalence for oscillatory fluctuations and more towards a net increase in area difference that can be approximated by a proportionate trend.

A further line probe was taken at the side wall as marked by an arrow, from the base. This is shown in Figure 5.10.
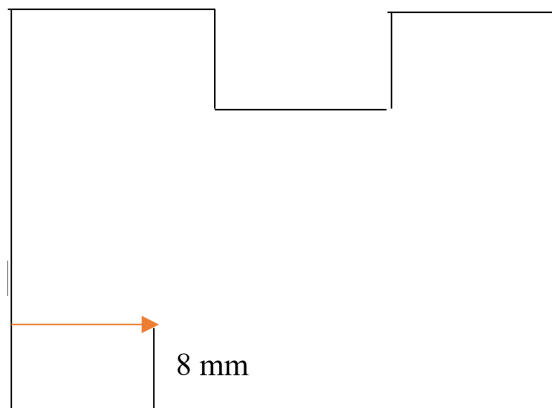
Figure 5.10: A schematic to show a line probe placement taken from the sidewall.

Figure 5.11 presents the kind of temperature profiles we see up to the point just prior to what is considered the free stream in the bulk of the fluid for the 225 kHz wave. Comparing this to the temperature profile at in the other areas of the domain,

a more fundamental picture is taken of the thermal mixing around different regions of the geometry. Again, Table 5.3 shows the corresponding times for each plot.

Table 5.3: Times for corresponding plots in Figure 5.11.

Figure	Time/ 10^{-5} (s)
a	1.6
b	1.67
c	1.99
d	2.09
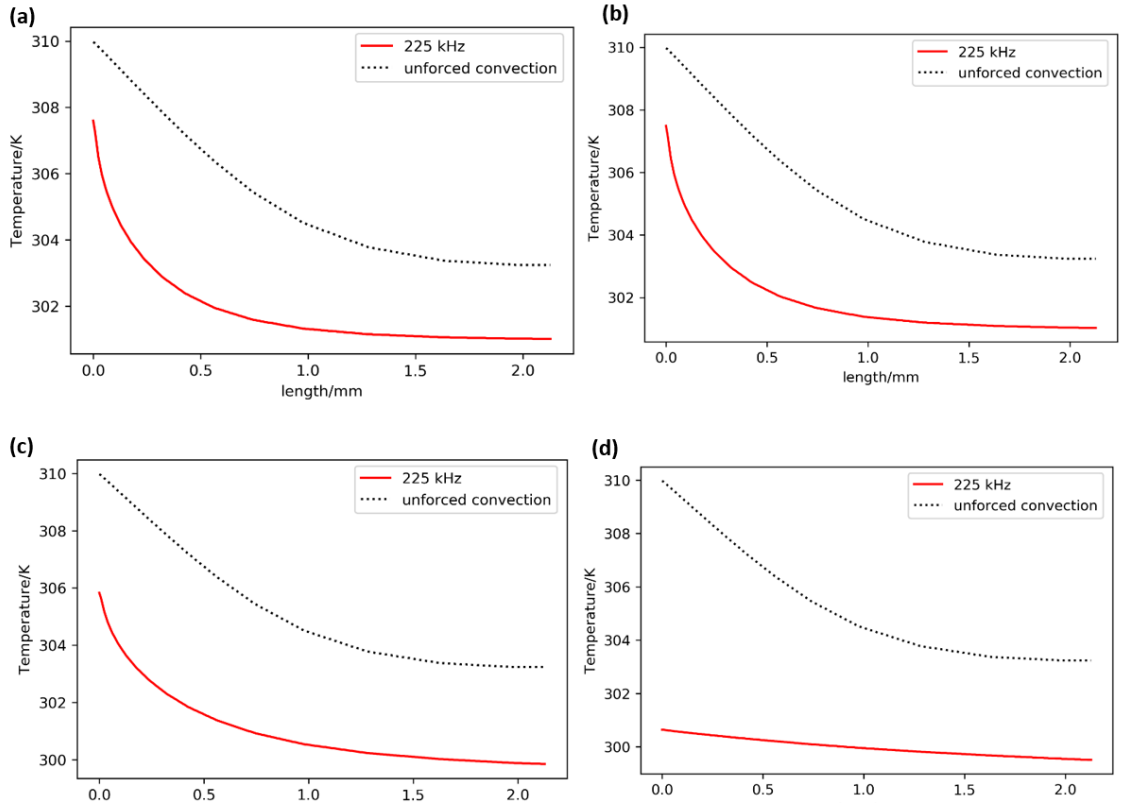
Figure 5.11: Temperature profiles taken for the side wall for 225 kHz.

Comparisons were then made with other temperature profiles. The bottom line probe, in the same position as presented with data previously and the top of the domain, taken the mid-point between the wide wall and the transducer as shown in Figure 5.12.

We notice that the distributions for the bottom and side, taken in close vicinity to each other share similar temperatures in what is considered their respective free stream. The change in shape across the period also appears to be similar, albeit the gradients of both lines are a reflection across some horizontal line taken across the y-axis. Nevertheless, both distributions appear to meet at a point across the period.
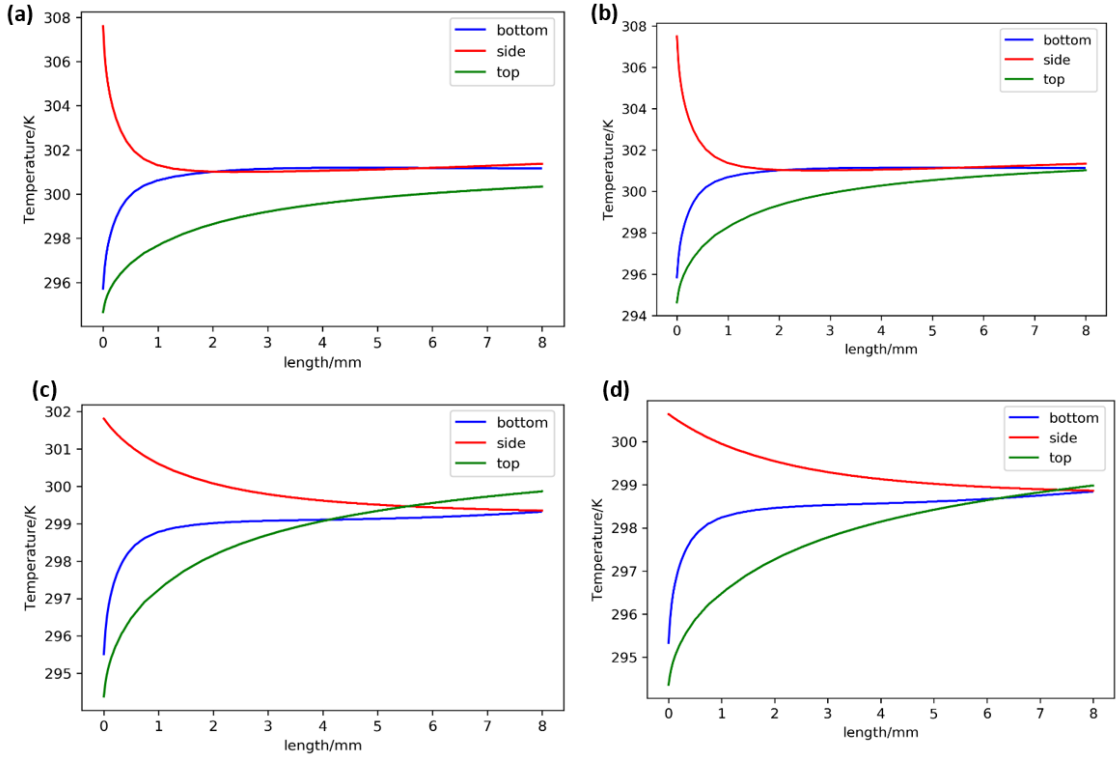
Figure 5.12: Combined temperature profiles at different points in the geometry for 225 kHz.

The distribution for the top side tells a different story however. The distinction between the profile and the free stream located in the bulk of the domain is not so clearly apparent compared to the bottom and side distribution. This is evidenced in Figure 5.4, from the resulting circulation creating a distorted profile across the top of the domain, created as a consequence of the development of cold fluid along the geometry's axis of symmetry which is seen to expand across the period (as mentioned in the previous section). This expansion effect is seen in Figure 5.12. As indicated in graph a of that figure, the magnitude of temperature is lower for the top profile compared to the bottom and side profile. As we move along the period, the top distribution appears to edge closer in magnitude to the other profiles. This can be attributed to the behaviour seen in Figure 5.4, with the expansion of colder fluid from the axial symmetry forcing warmer fluid to the boundaries of the computational domain.

The subsequent effects on the three profiles can be compared by normalizing the data for each and integrating each curve as seen in Figure 5.13.

For bottom and side profiles as presented in Figure 5.13, there is clear correlation between curve shape and time. For Figure 5.13a, curve area appears to decrease across the period thus indicating a reduction of overall thickness in the thermal boundary layer. The difference in shape can be attributed to the initial conditions for temperature. Recall that the internal field was set at a temperature of 280.5 K, whilst the bottom wall was set at a temperature of 293 K and the sidewall, a temper-

Figure 47: Normalised temperature profiles (a) at the bottom of the domain (b) taken from the side of the domain
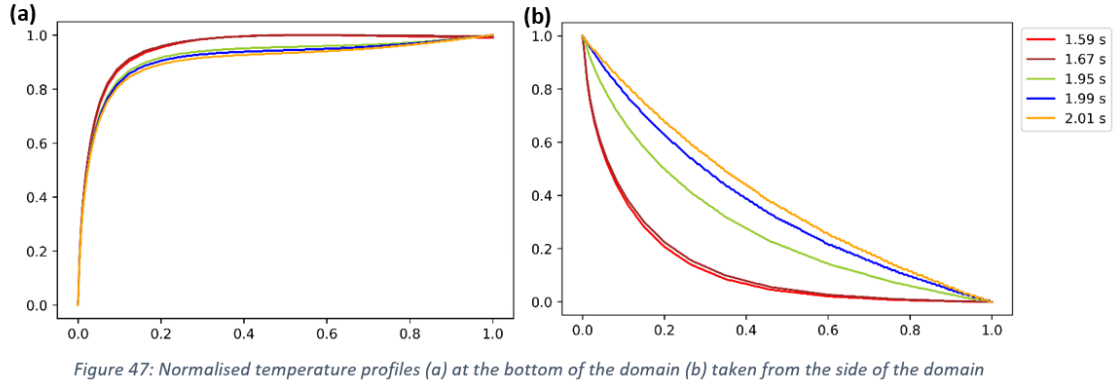
Figure 5.13: C: Normalised temperature profiles (a) at the bottom of the domain (b) taken from the side of the domain for 225 kHz.

ature of 310 K. The sidewall acts as a heat source thus explaining the difference in shape between Figure 5.13a and Figure 5.13b. The difference in temperature highlights the difference in the nature of the profiles. Figure 5.13a demonstrates (with the bottom wall acting as a cold source) a reduction in boundary layer thickness across the wave period whilst Figure 5.13b (with the sidewall acting as a heat source) demonstrates an increase in boundary layer thickness across the wave period.

The results however, are very general. A more detailed study across the wave period indicates some specific features (and in some cases deviations) to the trend as presented in Figure 5.14.
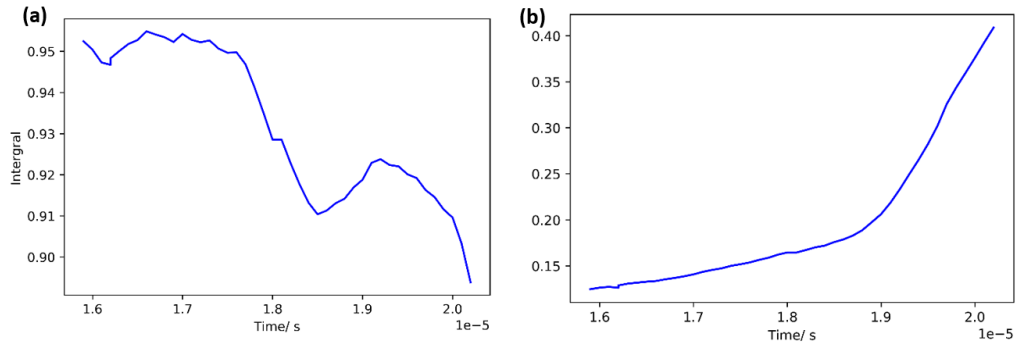
Figure 5.14: Curve areas across the 225 kHz wave period for (a) the bottom wall and (b) the sidewall.

Figure 5.14 presents integrals of curves presented in Figure 5.13 for detailed increments across the entire period. Whilst we observe in Figure 5.14a that there is a general trend towards a reduction in boundary layer thickness as in Figure 5.13, akin to Figure 5.8 and Figure 5.9 there appears to be some distinct contraction and expansion of the boundary layer size. On the other hand, Figure 5.14b, shows and overall increase in the boundary layer size. These findings are interesting as they suggest that many factors at play have an influence on the behaviour of the boundary layer across the wave period; The location in the domain and the nature

of whether the wall in question is a heat source or a cold source. These findings are important, as they build upon the knowledge of enhancing heat transfer. As stipulated in Section 2.11 Of the literature review, enhanced heat transfer comes through the disruption of the boundary layer. The data presented in Figure 5.13 and Figure 5.14 are important in telling us that the temperature of the thermal boundary, in comparison to the rest of the domain, along with its location play an extremely important role in the degree of heat transfer enhancement.

A further view of this behaviour can be gauged by observing data for 325 kHz and comparing. Figure 5.15 presents Figure 5.13b for 225 kHz in comparison with the same plot for 325 kHz at the side wall.
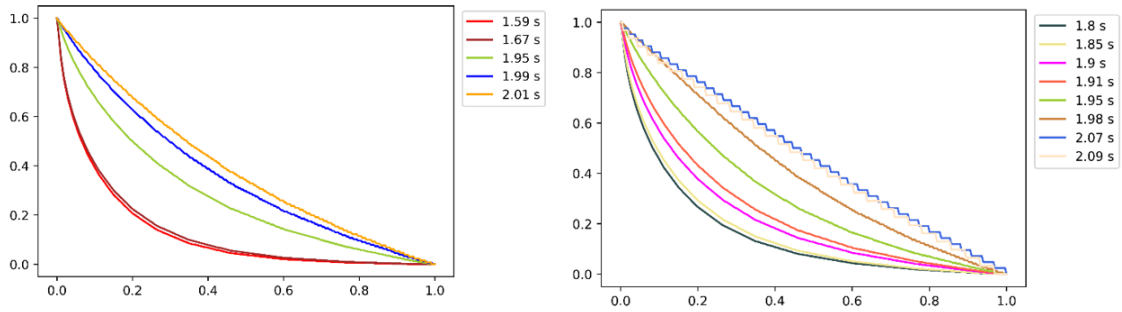
Figure 5.15: Normalised temperature profiles (a) at the bottom of the domain (b) taken from the side of the domain.

Again, their behaviour can be studied in greater depth by comparing the integral distributions across the wave period for both frequencies as presented in Figure 5.3. The time across the period for both frequencies has been normalised for comparison.

The behavioural difference between the amplitudes is significant. Figure 5.16a and Figure 5.16b are interesting in particular. The bottom boundary layer appears to mimic the oscillatory movement of the wave. A rapid expansion and contraction appears across the period however, the change in size between the two frequencies is evident. The larger frequency imposes larger fluctuations in the boundary layer size with what appears to be a gradually increasing amplitude across the period. On the other hand, the smaller frequency imposes only a very small oscillatory fluctuation and a net decrease in boundary layer size is evident. Figure 5.16b tells a different story. In contrast to Figure 50a, we observe a net increase in size at similar rates, with the only difference being the gradient variation across the period. Again, the higher frequency imposes a more drastic change in the size, but the differences in general are less prevalent. The net size of the boundary layer for a 325 kHz wave appears larger than the 225 kHz wave. Contrasted with both, Figure 5.16c shows similar magnitudes in size fluctuations for both frequencies, which is interesting as this region of the geometry is closest to the transducer. The net trends are not pronounced unlike Figure 5.16a and Figure 5.16b but the oscillatory motion imposed by the larger frequency correlates well with Figure 50a with the one crucial difference being the magnitude across the change in size.

These findings are further backed up by probe studies of individual parameters
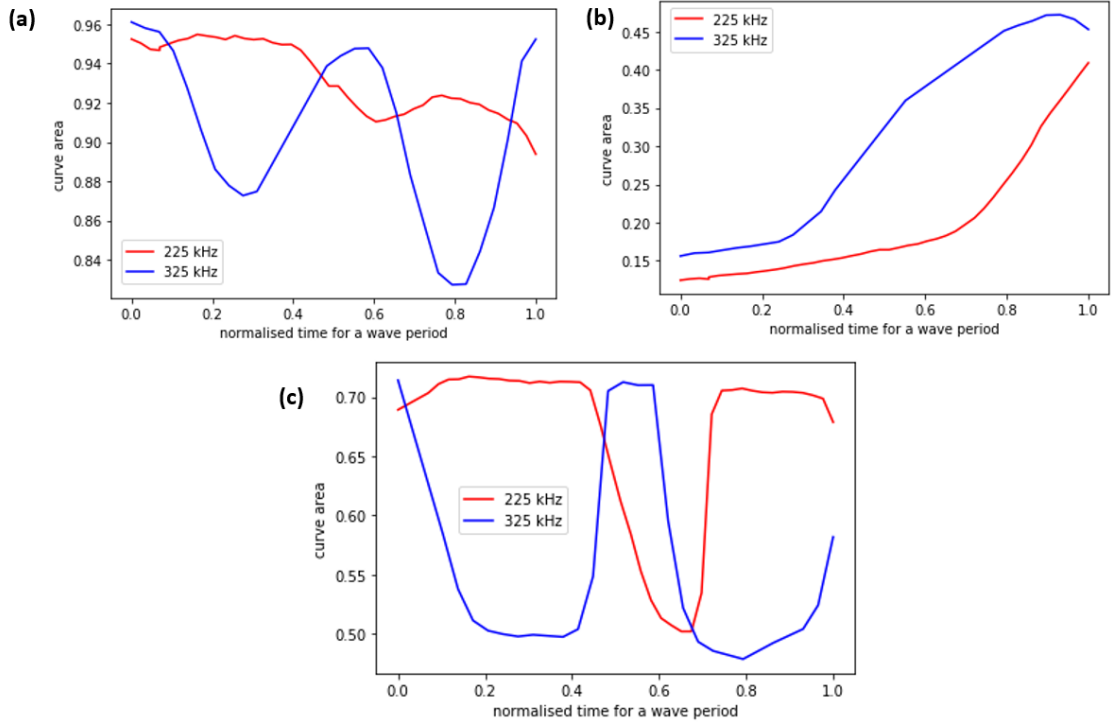
Figure 5.16: Curve areas across a wave period (normalised) for (a) the bottom wall (b) the side wall and (c) the top wall.

such as velocity and temperature. Note that a probe was placed along the geometry's axis of symmetry at point within the vicinity of the oscillating inlet boundary with coordinates $(0, 0.016, 0)$ was placed in the fluid domain, and intentionally placed along the geometry's axial symmetry. The two figures below present corresponding trends that tally well with Figure 5.8 and Figure 5.9. This is shown in Figure 5.17.

We notice that temperature variations for a 325 kHz wave have more prevalent peak and trough-like characteristics compared to the more randomised variation seen for 225 kHz. Of note however is that the general rate of cooling for each wave period is similar (keeping in mind that the wavelength of the 325 kHz period is smaller than the 225 kHz period). That being said, the findings are only a small representation of the over overall global temperature throughout the domain as we notice that in Figure 5.5, the changes between time steps are less prevalent compared to Figure 5.4. Of note however, is the distinctive oscillatory trend characterised by distinctive peaks and troughs and which appears to be associated with increased stability and steady-state of an acoustic flow. The findings can be further explored in the context of acoustic forces. The model is able to output values of acoustic force across the wave period as shown in Figure 5.18.

As stipulated in the boundary conditions, and as demonstrated in Figure 4.10, the waves propagate in the y-direction hence as presented in Figure 5.18, the largest fluctuations are seen in the y-direction. We notice once again that the trend can be likened to oscillatory variations. Figure 5.19 for 225 kHz paints a similar picture.
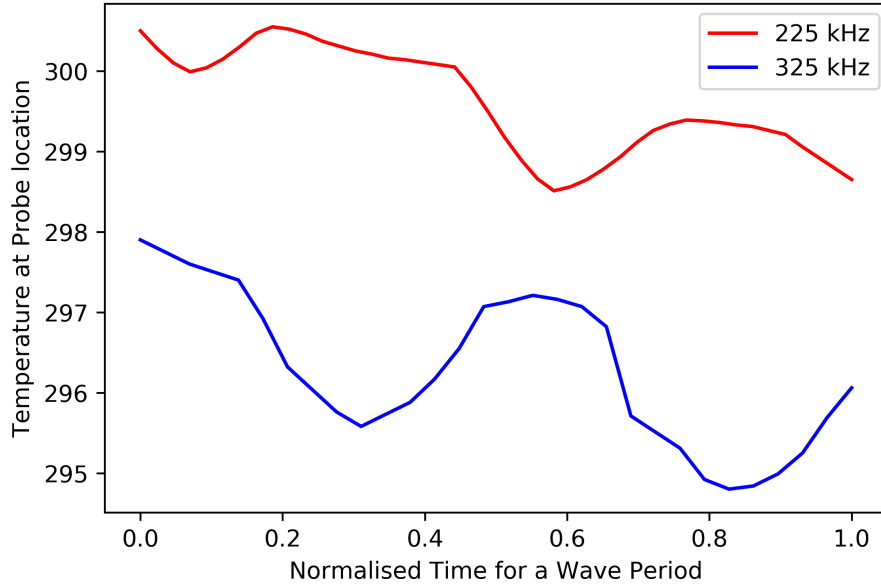
Figure 5.17: A graph to show the temperature fluctuations with time for 225 kHz and 325 kHz.

Here we notice the oscillatory nature of the acoustic flow. Z and y-components stay largely uniform at close to zero. What is interesting to note is that in both plots, a jump in the x and y-components exists at the start of the wave period. This could be attributed to the characteristic behaviour of the oscillating inlet, with the wave phase developing a pulse across the fluid domain corresponding to the beginning and then the end of one wave period. This behaviour also corresponds to the time range around the maxima marked in Figure 5.1 and Figure 5.2. The pulse across the entire domain appears to have essentially created fluctuations in all directions. It is interesting to note that both these shifts in the force components correspond to a reduction in measured temperature in these exact time ranges, as demonstrated in Figure 5.17. Furthermore, it appears that the greater jump in acoustic force (as seen for 325 kHz) corresponds with the biggest drop in temperature. Of equal interest is the similarities in variation between the temperature distribution in Figure 5.17 and the y-component of the mean acoustic force in Figure 5.18 with the jump in temperature around the 2×10^{-5} s mark corresponding with a similar jump in acoustic force.

Similar characteristics are seen for other parameters. To ascertain the steady-state, velocity was then measured across the wave period as with mean acoustic force as seen in Figure 5.20 and 5.21.

We note that there is little fluctuation across the board however, as before; the large jump in velocity corresponding to the jump in acoustic force is seen at the beginning of the period. This appears to suggest a corresponding link between acoustic force and velocity. Of further note is the increased magnitude of downward velocity for the larger 325 kHz compared to the 225 kHz wave. Putting this together, it is easy to see that the increased acoustic force seen from a higher frequency wave
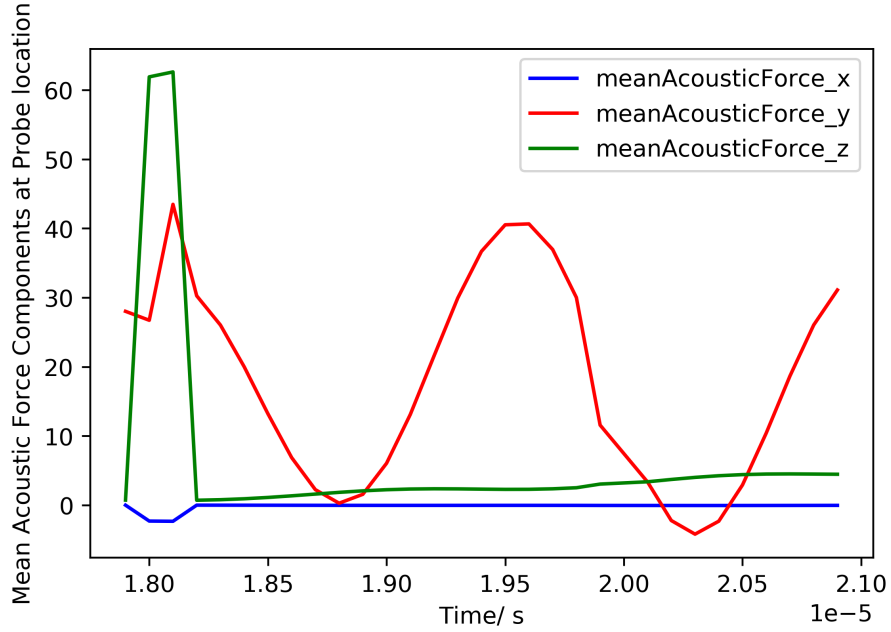
Figure 5.18: Mean acoustic force components across a wave period for 325 kHz.

enhances the mixing behaviour of the fluid and gives us a better glimpse into the way in which each parameter effects the overall structure of the fluid flow. We can also deduce that the uniformity of the x and y components for velocity can explain the relative uniformity in vorticity magnitude as presented in Figure 5.22. Moreover, we also notice a very slight increase in the downward y component of the velocity. The overall conclusion is then that we are able to identify what parameters effect what behaviours. In this instance, it can be hypothesised that velocity bares a significant influence on the mixing characteristics of the fluid. In both cases there is a net increase in the downward component velocity with time, and consequentially, the overall mixing appears to increase.

The corresponding vorticity magnitude is presented in Figure 5.22 associated with Table 5.4.

Table 5.4: Corresponding times for each vorticity plot for Figure 5.22.

Figure	Time/ 10^{-5} (s)
a	1.6
b	1.67
c	1.74
d	1.81
e	1.88
f	2.02

Here we notice that the overall shape of the distribution is marginally the same, however the size of rotational flow changes with time. The diameter of each circula-
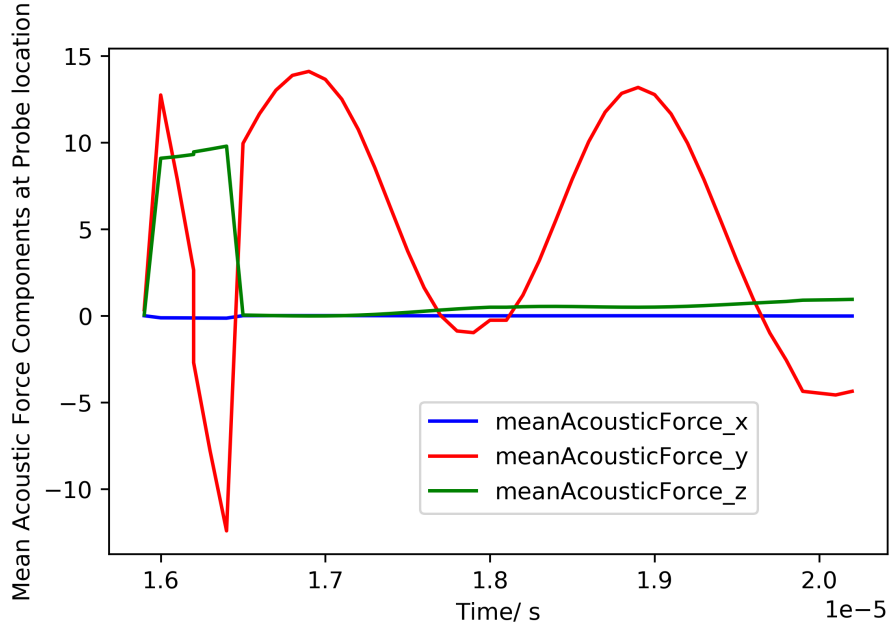
Figure 5.19: Mean acoustic force components across a wave period for 225 kHz.

tory region appears to reduce so that having reached the time for Figure 5.22(f); the significant regions of vorticity are concentrated towards the bottom of the domain. Recall Figure 5.14 where we observe a net increase in the disruption to the boundary layer at the bottom wall of the domain thus indicating a correlation between vorticity and thermal mixing. Recall also from temperature distributions presented in Figure 5.4 that there is a net increase in the volume of cold fluid, originating from the axis of symmetry. Again this could be correlated with the reduction in overall size of circulation, and the temperature behaviour. It can be deduced that the vorticity structure- with two distinct regions of circulatory flow is in effect, forcing the distribution of cold fluid from the axis of symmetry and outward.

We notice similar trends for the 325 kHz frequency as presented in Figure 5.23 (see Table 5.5 for reference).

Table 5.5: Corresponding times for each vorticity plot for Figure 5.23.

Figure	Time/ 10^{-5} (s)
a	1.6
b	1.67
c	1.99
d	2.09

The vorticity magnitudes in this case are observed to be higher, however the variations in time are similar.

A clearer picture of the vorticity structure can be gauged from studying the distribution in relation to the height of the geometry. The relationship of this height
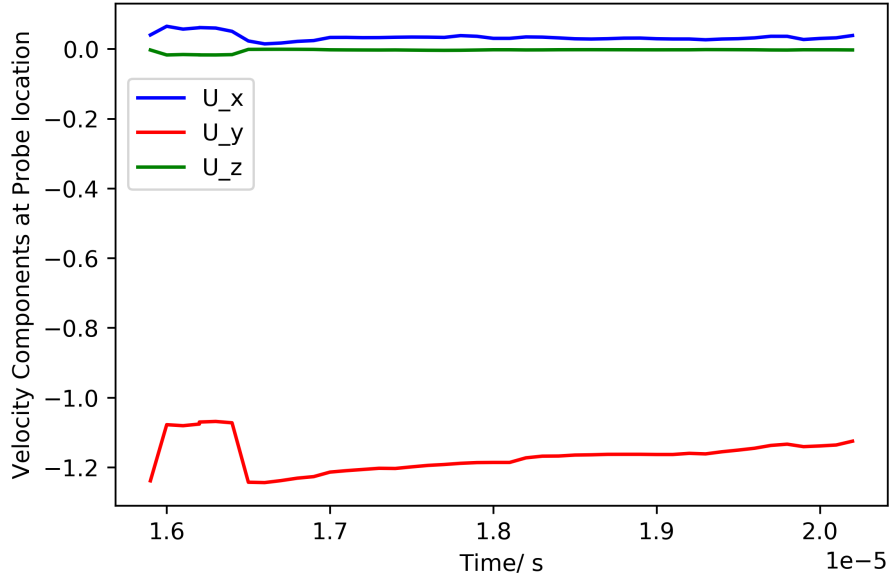
Figure 5.20: Velocity reading from a probe taken for the entire period for 225 kHz.

to the rest of the geometry is presented in Figure 5.24. A line was measured at the tips of the counter rotating regions of flow, across the period for each frequency. The resulting plot in Figure 5.25 shows the variation in height of the vortex distribution with time. That is to say, that in Figure 5.25, each individual point represents a horizontal line like in Figure 5.24 that overlays the equivalent position in the circulation at that point in the wave period. It was noticed that this line (as a result of the flow structure changes) changed position across the wave period thus culminating in Figure 5.25.

We notice that the height reduces at the same rate for both frequencies across their respective periods. Of further interest is the fact that for a 225 kHz frequency, the height and therefore the circulation distribution is more prevalent compared to the 325 kHz wave. The larger height range exhibited in the period indicates this. It is therefore interesting to note that whilst, a higher frequency wave generates a larger maximum vorticity, the overall distribution of larger magnitude vorticities is more prevalent across a period for a lower frequency wave. The rate of change to the overall structure also appears greater compared to a lower frequency wave. Figure 5.25 shows that through one wave period, the adjustment to the height across time is greater for the 225 kHz wave compared to the 325 kHz wave.

5.3 Summary

In establishing the fluid behaviour between wave periods, the first aspect of the flow behaviour that has been established is the degree of steadiness once apparent dynamic stability has been reached. This is clearly indicated by Figure 5.3 where the velocity distribution shows little variation between the respective times. However, it should be recalled that the purpose of this chapter is to ascertain the dynamic
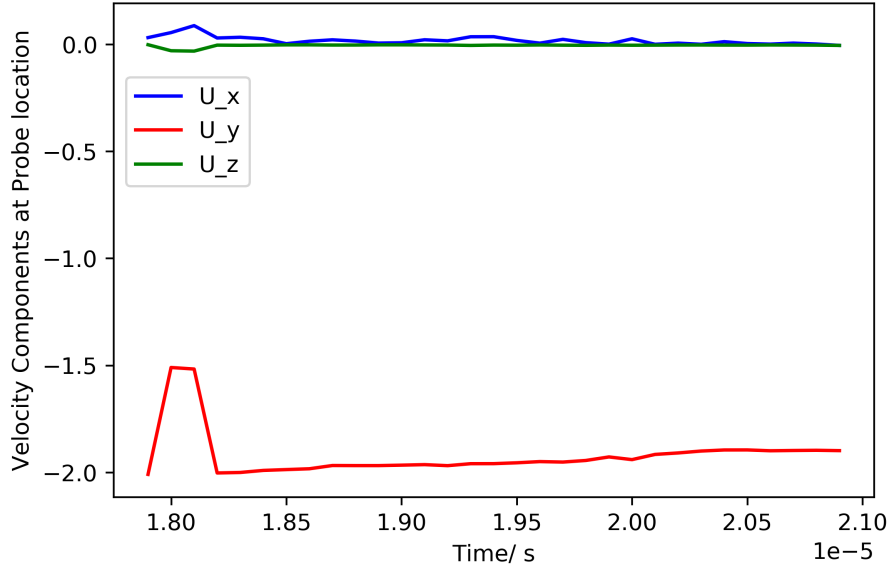
Figure 5.21: Velocity reading from a probe taken for the entire period for 225 kHz.

behaviour in between these respective peaks to gauge the fluid behaviour during a typical oscillation. By doing this, a more detailed picture is gained of how factors such as temperature distribution changes, and in tandem, the resulting effects on heat transfer.

For example, recall Figure 5.4. The detailed picture provides us with a window into how net cooling effects occur over time. The main observation was that the dynamic behaviour induces a shaft of colder fluid that originates from the geometries symmetrical axis- resulting from the circulation of the acoustically induced currents. This is clearly visible from Figure 5.4a to 5.4c. We notice a column of every decreasing temperature that steadily widens. Figure's 5.4d to 5.4f show that the shaft of fluid has undergone a dramatic widening and eventually, as the end of the wave period is reached, the entire flow domain has undergone a net cooling effect as a result of the widening of this column of fluid from the axial centre. It should be noted that the six plots presented are only mere windows from a time study with a much higher resolution. A detailed study of minute time steps as indicted in Figure's 5.8 and 5.9 provide a wider view of boundary layer behaviour across the period by measuring the percentage difference in boundary layer thickness on the bottom wall. In doing this, a detailed picture of the expansion and contraction of a boundary layer between the two frequencies is provided in tandem with the temperature plots presented in Figure's 5.4 and 5.5. It is interesting to note that on comparing the behaviour of the boundary layer for each frequency, the shapes of the graphs indicate a reversal of behaviour between the two frequencies. That is to say, that where one frequency demonstrates a distinctive series of contraction and then expansion, the other demonstrates a distinctive expansion and then contraction. Thus an indicator of the difference in phase behaviour between the two frequencies is highlighted. This is shown more clearly in Figure 5.16a where the
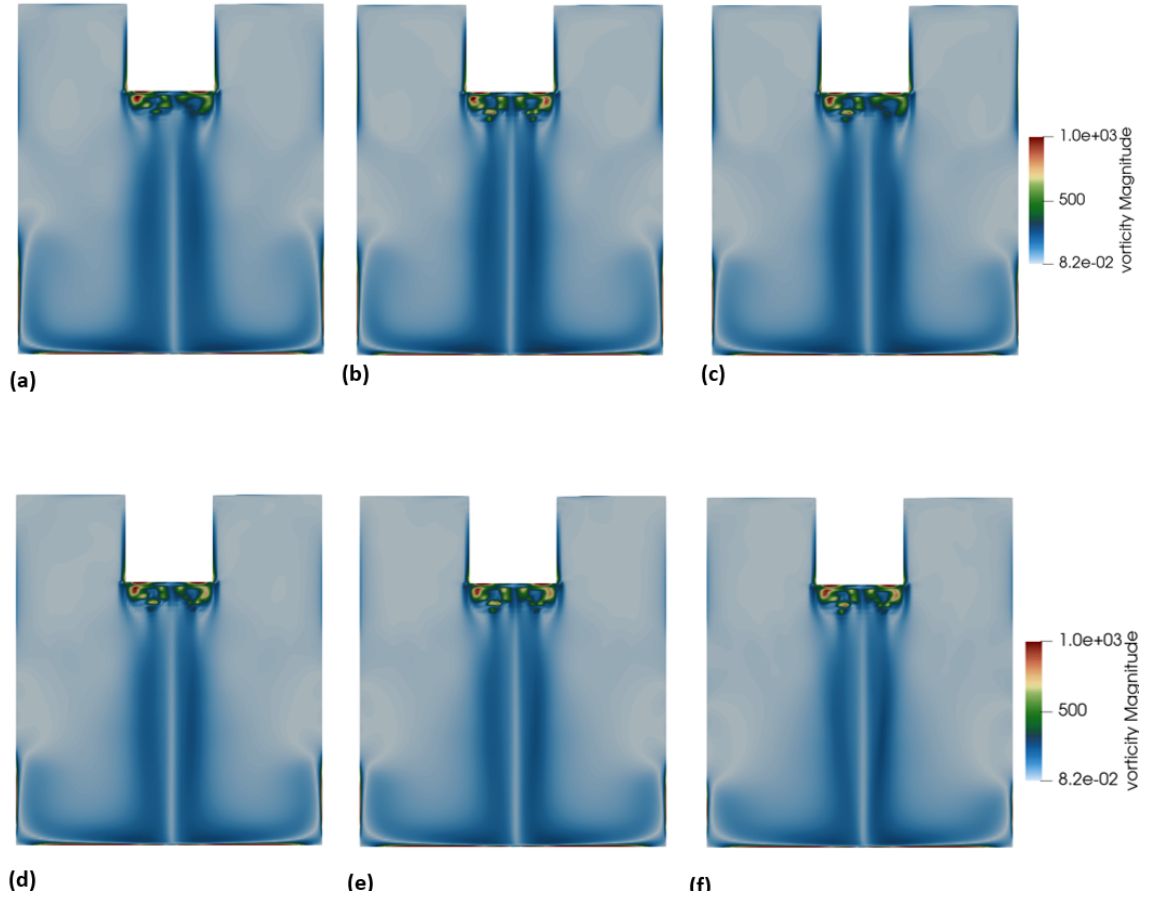
Figure 5.22: Vorticity magnitude plots for the 225 kHz frequency.

time for one period has been normalised to be able to draw comparisons between the two frequencies. Recall that the quantities measured are curve areas for each temperature gradient measured in a boundary layer. Thus, as indicated, for a 225 kHz wave, the increase in area indicates an expansion in the boundary layer. At the same region, the 325 kHz induces a contraction for the same boundary layer. The behaviour appears to be consistent across the entire period and indicates the nature of the phase difference between the two frequencies in the context of the flow structure. An interesting point is to then compare these findings with the measured acoustic force across the period as indicated in Figure's 5.18 and 5.19. Again, the configuration of peaks and troughs mimics the expansion-contraction nature of the measured boundary layers mentioned previously. For this it should be necessary to compare the y component of the acoustic forces measured from those two figures together as presented in Figure 5.26

The narrative from this is clear and correlates well with the overall discussion. The peaks and troughs can be pinpointed with reasonable correlation to each other through reasonable alignment of each consecutive peak and trough between the two frequencies. What this suggests is a clear correlation between phase positions, acoustic force and fluid structure. In the context of acoustic force, the acoustic force
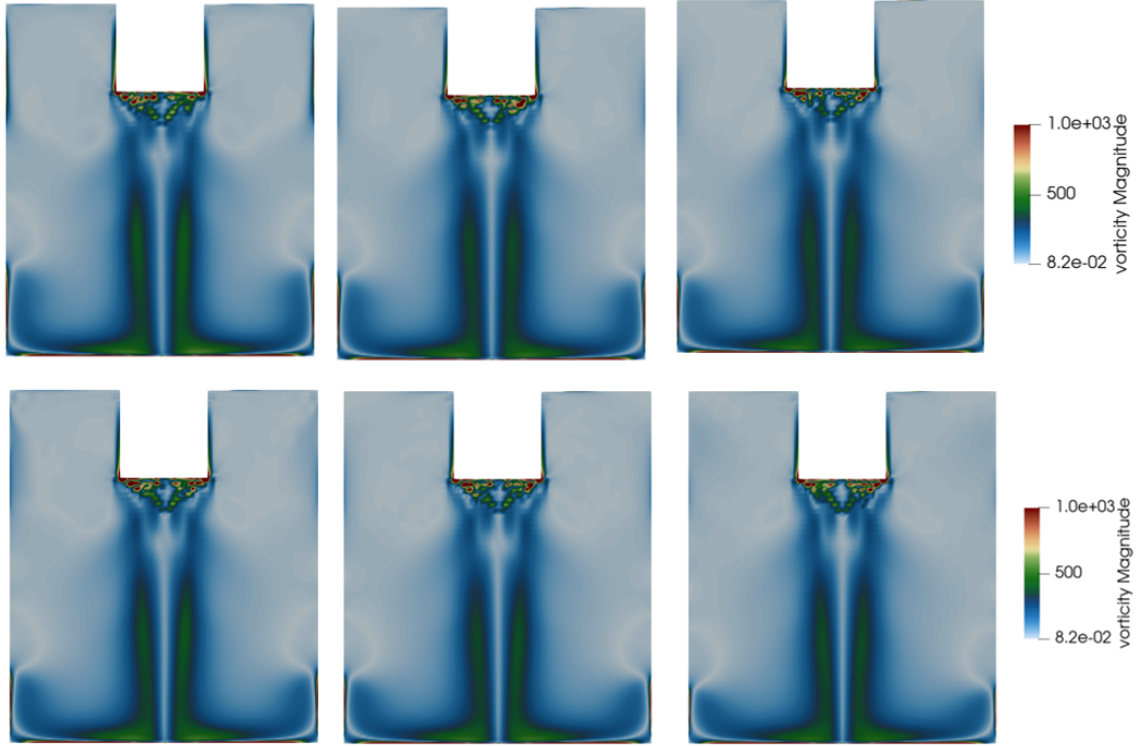
Figure 5.23: vorticity magnitudes for the 325 kHz frequency.

from the higher frequency results in a greater instantaneous cooling effect across the wave period. This is made clear between Figure's 5.4 and 5.5 but furthermore, a direct correlation can be observed between the acoustic force behaviour and the change in boundary layer shape on the bottom surface as indicated in Figure 5.16a. Specifically, the increase or decrease in acoustic force directly correlated with the increase or decrease in boundary layer size (specifically for the bottom wall). This is extremely important for our understanding of boundary layer positioning and the resulting effects from specific parameters of an acoustic flow. Based on these current findings, we can predict the behaviour of boundary layer size in this specific configuration (i.e a boundary layer formed on this geometry on the bottom wall) based on the oscillatory behaviour of the flow. To be able to explain why the correlations are seen with regards to the bottom surface boundary layer, Figure's 5.22 and 5.23 showing plots for vorticity should be revisited. This is a good indicator of the the degree of circulation observed throughout the fluid domain. For both frequencies, the largest circulation is observed across the bottom surface. This is consistent across the entire period This is extremely important for our understanding of how to optimize on cooling effects based on geometry configuration and setting acoustic parameters. As will be observed in Chapter 6 (and from literature) we know that the net cooling effects result from the disruption to the thermal boundary layer of a given heat source. The findings therefore offer us a window into what configurations are suited best to be able to fully predict the stages maximised cooling for a given setup. An idea is obtained as to what parameters are required to be
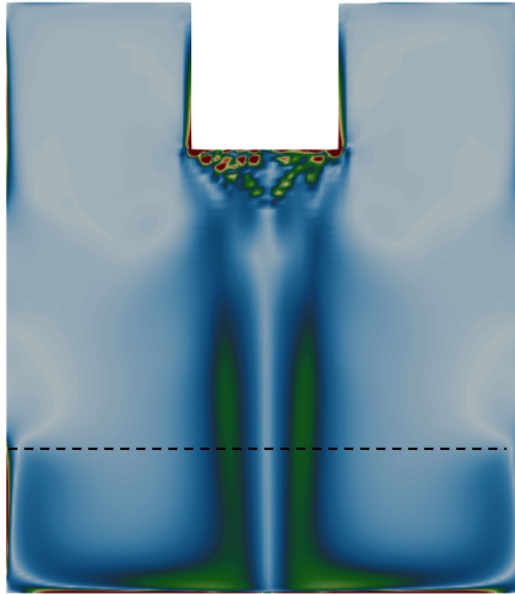
Figure 5.24: An example of a line measured to define a characteristic height of the circulation boundaries using vorticity.

considered in an effort to be able to achieve flow control to obtain the desired cooling mechanisms.
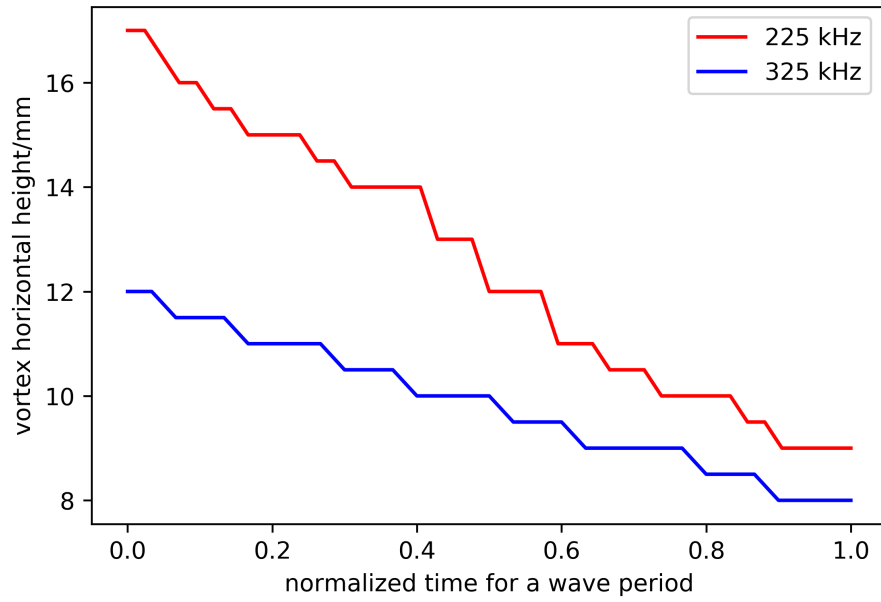
Figure 5.25: Vortex distribution heights, varying with time.
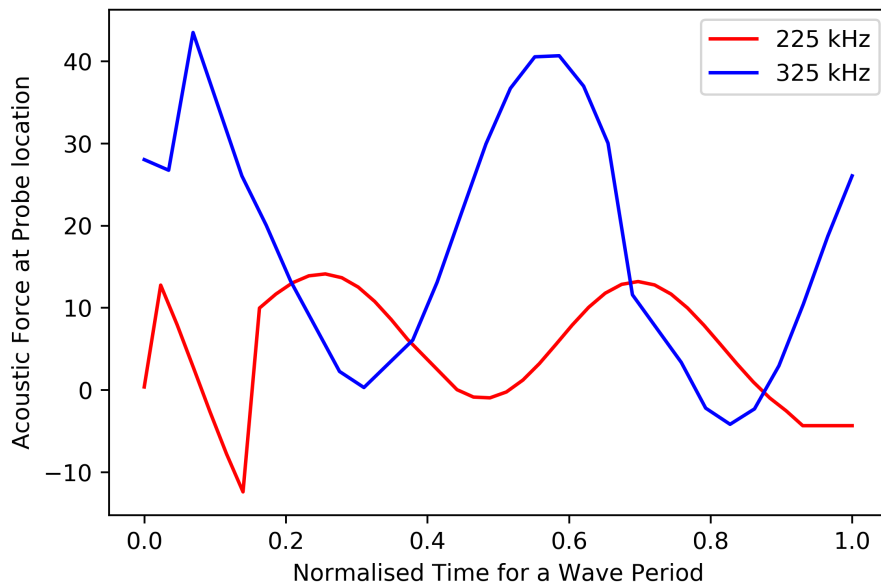
Figure 5.26: A comparison of the y-component acoustic force between the two frequencies for a normalised wave period.

CHAPTER 6

THE EFFECTS OF GEOMETRY ON ULTRASOUND ENHANCED CONVECTIVE HEAT TRANSFER

Chapter 3 provided a contribution to the knowledge base with the enhancing effects of heat transfer by ultrasound. Referring back to the literature, the consensus is that a reduction in volume leads to an increase in pressure amplitude. In the previous two chapters, a detailed parameterisation study of frequency, a primary property of ultrasound was conducted. For chapter 6 we take the same principle of parameterisation, and study the properties of a specific geometry; More specifically, the geometry setup for Dehbani et al. [13] outlined in Chapter 3. From literature, the closest to a parametric study achieved is a paper by Spigarelli et al. [118] who studied the aspect ratio of a microfluidic channel for several particle sizes. Our aim however is to identify geometries at much larger scales. Furthermore only five aspect ratios were used.

Validated results have been established, that can thus add further grounding to the findings in this chapter. Clarification is needed for research done by the likes of Hyun et al. [72] on the effects of oscillation amplitude on enhanced heat transfer. Studies of the effects of geometry parameters such as height, radius and frequency have been conducted and data is available on fluid parameters such as maximum fluid velocity and frequency effects on Nusselt number but a significant gap exists in the different effects between enclosed and open domains, proximity's of acoustic oscillators and their respective sizes. Specifically, a focus needs to be developed on the effects on heat transfer enhancement itself as it forms the principle justifications for the research. Talebi et al. [76] for example provided an overview of the effects of enclosure height on the acoustic effects but goes into little detail about the flow characteristics and its effects on heat transfer enhancement save for a measure of parameters such as average bulk velocity, maximum pressure amplitude and average bulk temperature as a function of the global solution. Thompson [119] provides an analysis of a two-dimensional wave-guide with varying height but not only is this a 2D rather than 3D analysis but emphasis is placed on the validity of the solution as opposed to a detailed paremeterisation of incrementally resolved

heights. Information about radial variation can be gained from an investigation carried out by Gubaidullin and Pyatkova [120], with a good idea of the nature of decay of Rayleigh-bound circulation as the cavity geometry in question is narrowed. The difference in circulatory position for both Schlichting and Rayleigh vortices is also studied between an isothermal and an adiabatic boundary condition but again these studies are done for only four separate radius values.

Recall that Section 4.5 for an overview of Stokes, Schlicting and Eckhart Streaming. Eckhart streaming, where the length of streaming is typically the length of the fluid chamber [121], is often known to be an unwanted side effect of cell manipulation in none-invasive tissue engineering (See Section 2.1 and 2.6). It has been noted in previous investigations that using acoustically transparent foils in resonator designs reduces the size of streaming [122]. A further investigation by the Spengler and Jekel [123] found that a decrease in vessel size along the acoustic axis might actually deter the occurrence of Eckhart-type acoustic streaming as well as reduce its size. Again, he highlighted that further research would be needed to strengthen current methods in this research area. The intention of this chapter is to carry out a refined parameter study of vertical heights as per the variation along the acoustic axis. The specific focus will be on comparisons between fluid characteristics and the corresponding effects on heat transfer enhancement.

6.1 Geometry and Boundary Conditions

For this chapter, we must refer back to Figure 3.2. The geometry represents a platinum wire submerged in a symmetrical tank of water at a depth of 80 mm. The transducer is located directly below the wire as marked in Figure 3.2. In the experimental setup, the tank was placed in an ice bath at 0°C. The boundary conditions are presented in Table 6.1.

Table 6.1: Boundary conditions for the geometry setup.

Boundary	Condition	Temperature Value/K
Tank Wall	No slip wall	273
Transducer	No slip wall	273
Platinum Wire	Fixed Gradient	Heat flux dependant

273 K was set at all walls for initial conditions to reproduce the conditions of the ice bath. Within OpenFOAM, the "Fixed gradient" boundary condition was used to mimic the heat flux conditions set across the wire surface. All walls had no slip conditions indicating zero velocity at all surfaces. For this study a heat flux of 294.6 KWm^{-2} was applied across the platinum wire.

6.2 Results and Discussion

Talebi et al. [76] postulates that an increase in enclosure height leads to a heat flux that is distributed into a greater domain volume. As discussed in the literature review, a summary of the effects of acoustic flow on bulk parameters such as average temperature and velocity is presented but little is discussed on the resulting flow characteristics and its corresponding effects on heat transfer enhancement. A height study in this case was conducted at 10 mm increments for a run time of 5.5×10^{-5} s. The evolution of the fundamental flow structure can be observed in Figure 6.1 through to Figure 6.2 using a measure of X-component velocity contours.
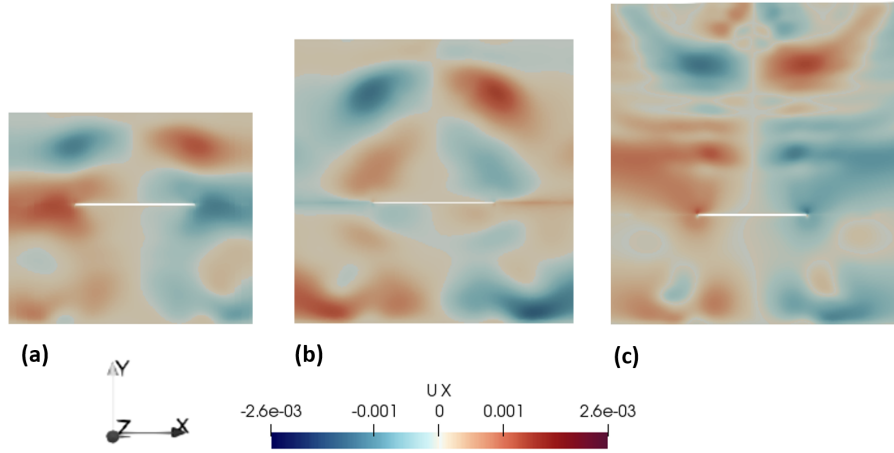
Figure 6.1: X component velocity in ms^{-1} for different heights at (a) 30 mm, (b) 40mm and (c) 50mm.

The velocity distribution is able to present a picture of the circulation evolution for various heights, a feat where previous research has been considerably lacking. What is clear is that the flow structure varies considerably between different heights. On one hand a singular pair of counter rotating circulatory loops is exhibited at 30 mm and 70 mm heights. On the other, a double, quadruple and triple pair of loops are observed at 40 mm, 50 mm and 60 mm respectively. What is also clear is that for all heights bar 70 mm, the rotation of the principle circulatory pair remains constant, in this case being anti-clockwise on the left and clockwise on the right (both the 40 mm and 50 mm heights also show smaller counter-rotating loops). A switch takes place at 70 mm which reverts back to a singular pair but with a clockwise movement on the left and an anti-clockwise movement on the right. For those heights where multiple pairs of loops form, it is important to note that one pair always appears as the dominant. For the purposes of this chapter, these dominant circulatory pairs will be referred to as the "primary". This terminology will also apply to the single circulatory pairs formed at both the 30 mm and the 70 mm heights. It is interesting to note here that changes to the number of circulatory loops take place on a macroscopic scale as as well as a microscale as presented in Section 4.5 of the literature review. We should once again refer to findings from Tajik et al. [58] who observed that acoustic streaming consistently resulted in an
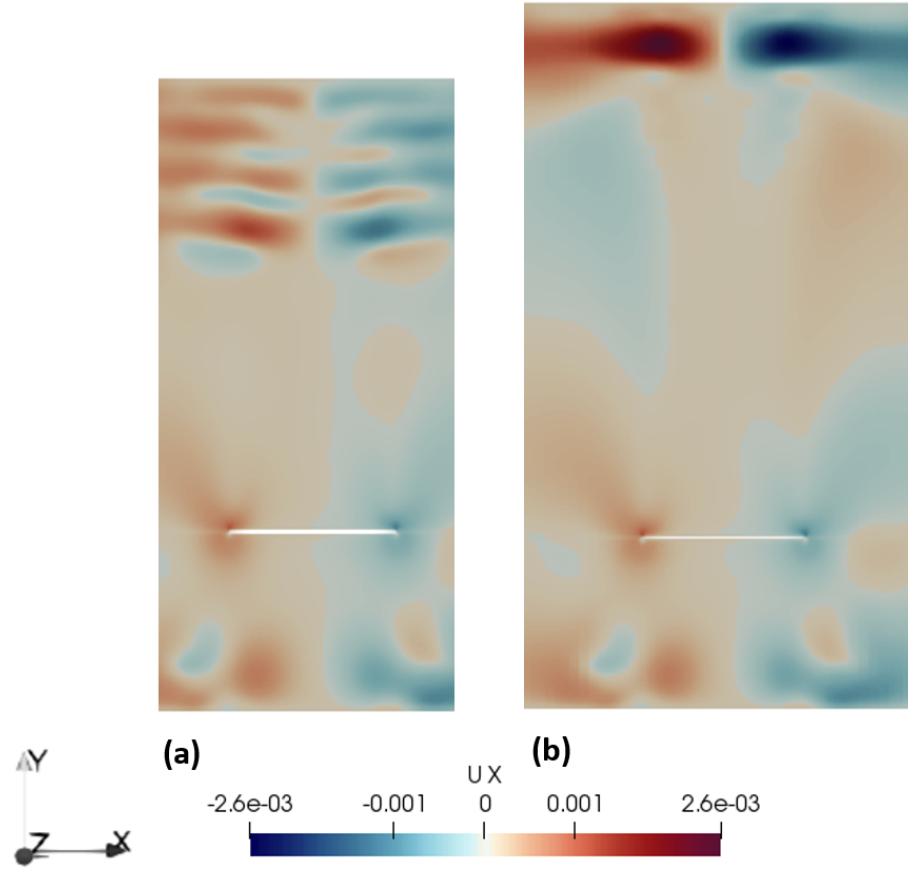
Figure 6.2: X component velocity in ms-1 for different heights (a) 60mm and (b) 70mm.

even number of loops. Morever, Wang and Kuznetsov [60] observed four circulatory loops for a height of 1.5 mm and a wavelength of 20 mm. It can be seen that a 40 mm height as observed in Figure 6.1b also matches this observation.

A line probe was taken down the vertical axis of symmetry for each primary circulation loop (in this case, the vortex on the left hand side of each pair was chosen). A reference height from the wire surface was used as a variable for each height, as the effects of heat transfer across its surface are the primary concern for this chapter. This is presented in Figure 6.3

Figure 6.3 is able to quantify the changing positions of each primary circulatory pair in reference to the platinum wire. Parameters such as circulation size, orientation (clockwise, counter-clockwise) and vertical position can all be observed. Fundamental observations can be made in each of these categories. An increase in circulation can be seen between 30 mm and 50 mm heights. This is followed by a drastic reduction at 60 mm. The circulatory pair at 70 mm demonstrates the most extreme change in behaviour with a change in the direction of rotation and a drastic increase in the vertical distance from the wire surface. What is difficult to quantify is the overall effect of each circulatory pair. For example, there is no distinct trend between maximum velocities measured at the centre of each loop although
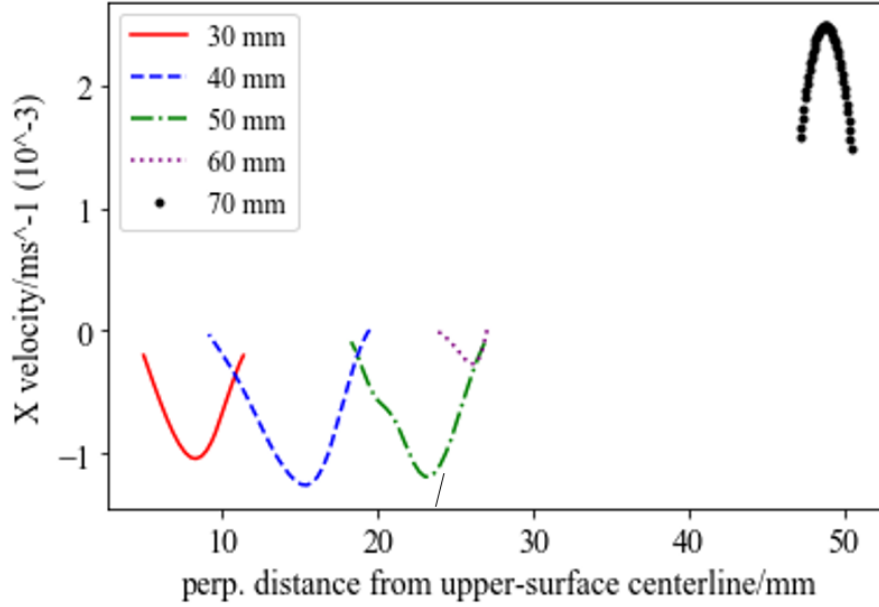
Figure 6.3: X-component velocities across vertical axis of symmetry for all heights.

an increase in loop size corresponds with a greater maximum velocity between 30 mm and 60 mm heights. On the other hand, the largest max-velocity magnitude is observed at 70 mm but the vertical height of this loop is clearly smaller than both the 40 mm and 50 mm heights. The integral of each velocity curve was therefore calculated to define a circulation intensity that accounts for both circulation size and velocity as shown in Figure 6.4.

Figure 6.4a is therefore able to define single values for each primary circulatory pair that can be compared to the resulting heat transfer enhancement seen in Figure 6.4b. The observations fit well with the findings from Figure 6.3. An increase in intensity is seen between the heights of 30 and 50 mm. The rapid decrease at 60 mm corresponds to the behaviour seen in Figure 6.3. What is interesting to note is the value at 70 mm. It is clear that despite its reduction in size compared to those found between 30 and 50 mm, that taking into account its extremely large maximum velocity results in a much more intense circulation. It is therefore important to make comparisons with the resulting heat transfer enhancement for each height. In Figure 6.4b it is evident that changes in heat transfer enhancement falls into two distinct trends. An exponential increase is observed between 20 mm and 40 mm heights. A rapid decrease marks the starting point of a trend with minimal variation up to 70 mm. The increase in heat transfer enhancement between 30 mm and 40 mm corresponds with the increase in circulation intensity within the same parameters although the two plots then diverge at 50 mm, with only a slight levelling off for circulation intensity whilst the heat transfer enhancement for the same heights undergoes a rapid decrease. From this point there appears to be little correspondence between the two variations. The rapid increase could be explained by the formation of an additional pair of counter-rotating circulations. As mentioned previously, additional pairs form at 40 mm, 50 mm and 60 mm. At this
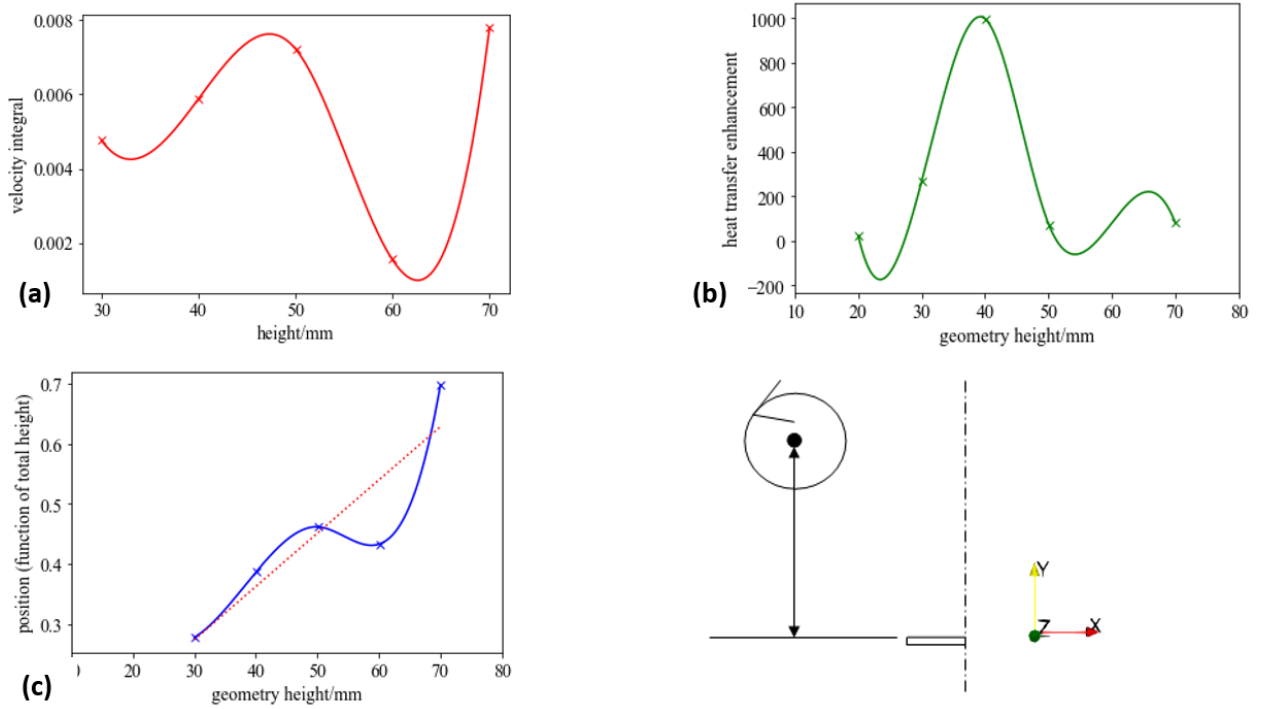
Figure 6.4: Data showing (a), X-velocity integral calculations of vortex velocity distributions for all heights, (b) heat Transfer Enhancement across the platinum wire for each height and (c) vortex centre position in reference to wire surface area.

point, we refer back to Figure 6.3 and Figure 6.2. For a 50 mm height it is worth noting that there is a considerable increase in vertical distance between the wire and the centre of the two smaller counter-rotating loops in comparison to the 40 mm height, a distinction which could thus explain the rapid reduction in heat transfer enhancement. It can also be observed that the increase in vertical distance between the primary vortex centre and the wire surface varies linearly from height to height. This is demonstrated more clearly in Figure 6.4c where the y-axis denotes the vertical position of the primary vortex centre as a function of the total height for each geometry (as denoted on the x-axis). This parameter is demonstrated more clearly in the associated schematic in Figure 6.4. At first glance, it could be argued that the result at 60 mm could be classed as an outlier however on further viewing it is clear that there is synergy with Figure 6.4a. A linear increase is observed between 30 mm and 50 mm heights and then a reduction at the aforementioned 60 mm mark albeit for Figure 64c this is considerably less pronounced. It should also be noted that the primary circulatory pairs in all heights maintained a relatively constant lateral position at approximately 8.5 to 9 mm from the center-line of the geometry's plane of symmetry.

Two primary factors are at play. On one hand it has been postulated that the formation of multiple pairs of loops could have a positive effect on heat transfer enhancement. This is seen at 40 mm for example where a value of almost 10 times the initial value at 20 mm is observed. On the other hand, this hypothesis is contra-

dicted by the fact that despite the formation of multiple pairs at proceeding heights, not only does this value decrease, but also appears to have limited effects for the final three heights. We therefore refer back to Figure 6.4. An overall increase in perpendicular distance between the vortex centre and the wire surface is observed. It could therefore be argued that vertical distance plays a gradually increasing role in the effects on heat transfer. The question arises as to what point the effects of vertical distance outweighs the effects of multiple circulatory pairs (which in theory should have a positive effect on heat transfer enhancement).

To provide a clearer picture, the height resolution study was conducted at a greater number of increments to identify the optimum enhancement. This is presented in Figure 6.5
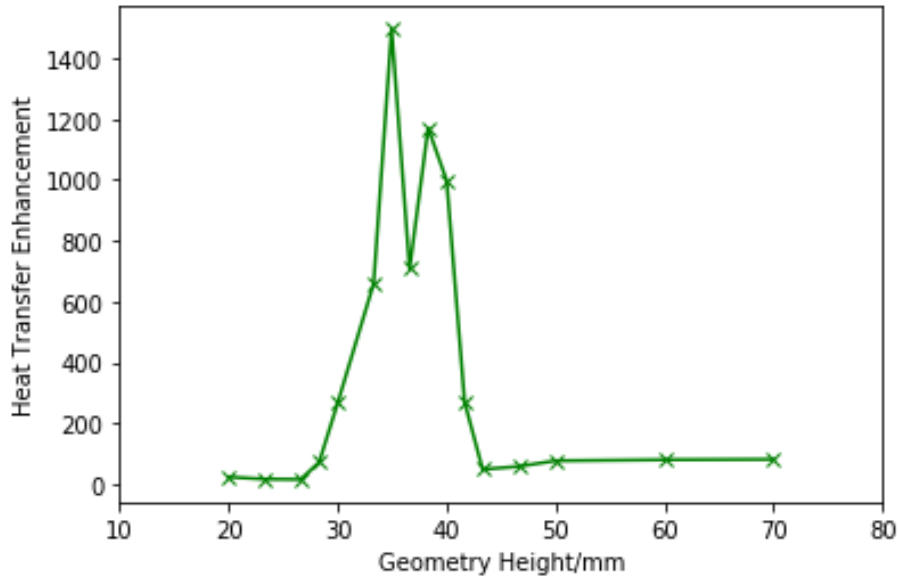
Figure 6.5: Heat transfer Enhancement for heights taken at an increased resolution.

A height range of approximately 30 to 43 mm shows profound effects on heat transfer enhancement with an optimum value seen at the 34 mm mark. Either side of this, there is minimum effect on heat transfer, and the values remain relatively uniform between each height. It is worth noting the value at 37 mm which one could class as a potential outlier however a more fuller picture of the flow behaviour can be ascertained by isolating the 30-43 mm range before any assumptions are made.

Zooming in on this so-called "optimum range", a more fundamental picture can be built by comparing the variation of heat transfer enhancement with a measurement of the maximum velocity magnitude measured at the centre of the corresponding loop for each height. This is seen in Figure 6.6.

There is significant correlation here between the variations of both quantities with a peak velocity magnitude seen at an optimum heat transfer value for a geometry height of 35 mm. Furthermore, the data at 37 mm, previously noted as a potential outlier shows corresponding deviation for vortex velocity magnitude as well thus indicating the importance of circulation behaviour in enhancing heat transfer
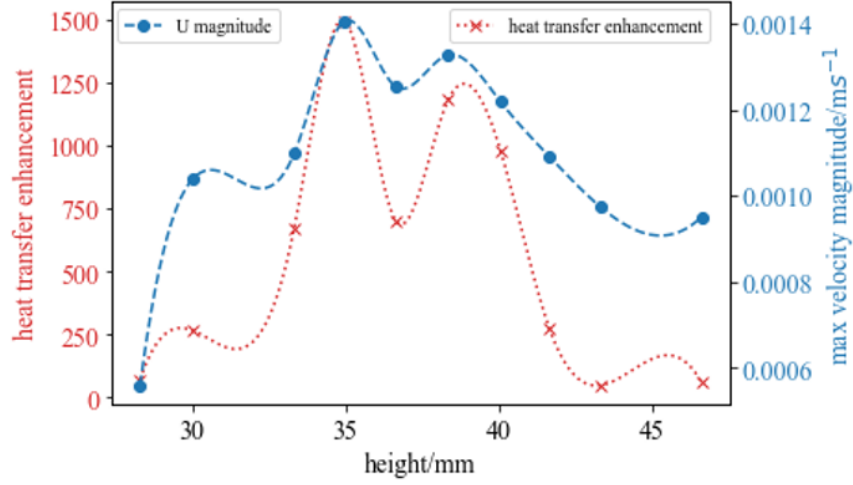
Figure 6.6: Comparisons of trends between velocity at respective loop centres and heat transfer enhancement.

acoustically.

To get a global view of loop characteristics, the vorticity was measured down the vertical axis of each loop symmetry corresponding to a height (as with Figure 6.3). The development of vorticity through the entire height range was found to fall into two distinct behavioural categories marked in three different height ranges. Figure 6.7a and Figure 6.7c show the vorticity for height ranges of 23.3 mm to 30 mm and from 41.65 mm to 70 mm respectively. Recall that in Figure 6.5, the corresponding heat-transfer enhancement changes were minimal for these ranges.

The development of vorticity between 23.3 mm and 30 mm is shown to be sporadic. The change in size of loop from height to height appears not to follow any specific trend or uniformity. The same can be said for Figure 6.7c. From 41.65 mm to 46.6 mm, the development of asymmetrical loops is seen with no clear trend in changes from height to height. When the height is increased to 50 mm and upwards, several loops form as indicated by the numerous peaks in the distribution. Again, no clear trend exists here and the distribution is random. Again, recall the changes in the corresponding heat transfer enhancement for these heights in Figure 6.5. The values were minimal from height to height.

A significant contrast is seen for the so-called "optimum range" from 33.3 mm to 40 mm range in Figure 6.7b. Recall that in Figure 6.5, this range had the most pronounced effects on heat transfer. Here the vorticity distribution is arranged in smooth parabolic trends. Also note their position in relation to the upper wire surface. Figure 6.5a and Figure 6.5c present vorticity distributions that fluctuate randomly in width and position in relation to the wire surface. In contrast, the vorticity distribution here maintains reasonably consistent widths with only slight variations in their position, the most prominent being the increase in height from 33.3 mm to 34.95 mm. An integral calculation of each curve can be performed to deduce size of vorticity in each distribution as seen in Figure 6.8.

What we notice is an increase in integral values from height to height in this range. Thus whilst this cannot be deduced to be a proportionate increase, this is more than can be said for Figure 6.7a and Figure 6.7c where the curve areas within each bound change randomly. To summarise, the development of random vortex structure changes from height to height, with minimal uniformity correlates with minimum change or effect on heat transfer enhancement. Contrast this to the "optimum range" between 30 and 40 mm, where the vorticity distributions are uniform, stable and match a trend of increasing curve area, and most importantly, correlate with significant changes in heat transfer enhancement. To establish a fuller picture of this observation, it is worth taking a look at the loop structures in their entirety within the context of vorticity. To compare and contrast, measurements in Figure 6.9 were taken for two height values within the optimum range; 34.95 mm, (where the heat transfer enhancement was seen to be the largest) and 40 mm. The 50 mm height was also measured to compare and contrast the flow structure in and outside of the optimum range.

The comparisons are clear. The development of several pairs of Von Kárman like circulatory loops that form at random sizes are clearly evident at 50 mm. To contrast this,6.9a and 6.9b show distributions that are closer in visualisation to the theoretical fluid structure as denoted by Legay [8] for acoustic streaming; Two distinctive primary regions of circulation above the wire surface (with slight vortex shedding observed in both plots) as opposed to multiple shedding regions as observed in Figure 6.9c. These findings are paramount to our understanding of acoustically enhanced heat transfer. The suggestion is that, it is not necessarily the vorticity magnitude or the derived flow quantities that factor's into enhanced heat transfer. That much is evident in Figure 6.9 where Figure 6.9b demonstrates vorticity magnitude values at the circulation centre that are larger than that of Figure 6.9a. But instead, what is observed is that it is actually the stability and the structure of the vortices themselves that contribute to enhancing heat transfer. A stable single pair of well-developed circulatory regions as characterised by the theory presented by Marshall and Wu [62]. It appears to have profound effects as opposed to unstable asymmetrical loops that form in multiple shedding pairs presented in Figure 6.9c, and demonstrated by the random fluctuations in fluid structure as seen in Figure 6.7a and 6.7c.

6.3   Summary

A CFD study of the effects of acoustically enhanced flow on heat transfer was conducted to ascertain the effects between specific flow parameters and the variation in heat transfer between different geometries. The results form the foundations of further study into the effects of circulation and geometric parameters. A clear correlation can be deduced from the effects of loop velocities and overall size. Further work, having already focused on the extent of different parameters and their effects on the thermal boundary layer in the previous two chapters, now looks at the effects of the fluid structure on heat transfer itself. Examples such as the proximity of the heat source to the loop centre verses loop velocities along with corresponding loop

size and direction are areas that can draw comparisons with the current data. The literature conveys how the number of loops and general size changes on a microscopic scale. Chapter 6, on the other hand provides us with a glimpse of how flow structures in acoustic streaming change for much larger geometries.

It is evident from the findings that geometry height has a significant effect on heat transfer enhancement. Of particular note is the hypothesis that loop structures play a larger part in enhanced heat transfer than measured fluid quantities such as velocity and vorticity magnitude. From this idea, has sprang the concept of the "optimum range" of geometry height values where the distribution of loop vorticity has constituted to the most profound effects on heat transfer. This optimum range is observed in Figure 6.5 between the heights of 26 mm and 43 mm. We should look to the characteristics demonstrated by the contour plots to ascertain certain traits that correlate with the effect on heat transfer. Within the optimum range, the contour plots show loops that form in single pairs and have uniform distributions that remain steady in size from height to height as shown in Figure 6.9a and Figure 6.9b for example. Contrast this to geometries outside the optimum range where the circulatory loops form in multiple unstable pairs- Figure 6.1c and Figure 6.9c present plots showing this- and the effects on heat transfer enhancement from height to height become minimal. The changes can be observed from a graphical point of view in Figure 6.7. Figure 6.7b presents curves modelling the vorticity for the optimum range. Recall that the appearance of the curves in this are parabolic in nature with distinct peaks between curves that exhibit a moderate degree of symmetry. This corresponds to the stability presented in their respective contour plots showing a distinct pair of counter rotating loops. In contrast, heights outside the optimum range (Figure 6.7a and Figure 6.7c) exhibit fluctuating distributions across the length of the measured distance and the corresponding curves show multiple pairs of loops.

It is interesting to note from Figure 6.7 that for all heights, the loops form within the vicinity of the upper wire surface. In some cases (as evidenced in Figure 6.7a) the surface of the wire is located very much within the circulatory cell of fluid- this is clearly the case for the 30 mm height. A larger scale of vorticity is observed here in comparison to the optimum range. Again this suggests the idea that the fluid structure and stability of the circulations plays a larger role in the degree of heat transfer as opposed to the intensity of the circulation. Comparing this to the findings of Wang and Kuznetsov [60] who identified a correlation between circulation size and enhanced heat transfer, it is evident from Figure 6.8 that the optimum range agrees with this. Figure 6.7 shows a general increase in circulation size that in general correlates with the change in heat transfer in Figure 6.5.

In terms of further work, there is potential hear to study the cooling of larger elements. In this case, the platinum wire was chosen, because a base of experiments had already been established as a starting point by Dehbani et al. [13]. Next steps for this work could be to study the effects on larger heat sources such as pipe geometries. In this way, a clearer picture of how enhanced heat transfer effects change with geometry shape thus further improving our understanding. This will be discussed in Chapter 7.

Thus to conclude, a correlation between two counter-rotating loops exists that results in the largest effect on heat transfer. Where further work is possible, the height resolution within this optimum range should be increased so as to collate further data to add greater depth to this theory. This is a significant idea for future work.
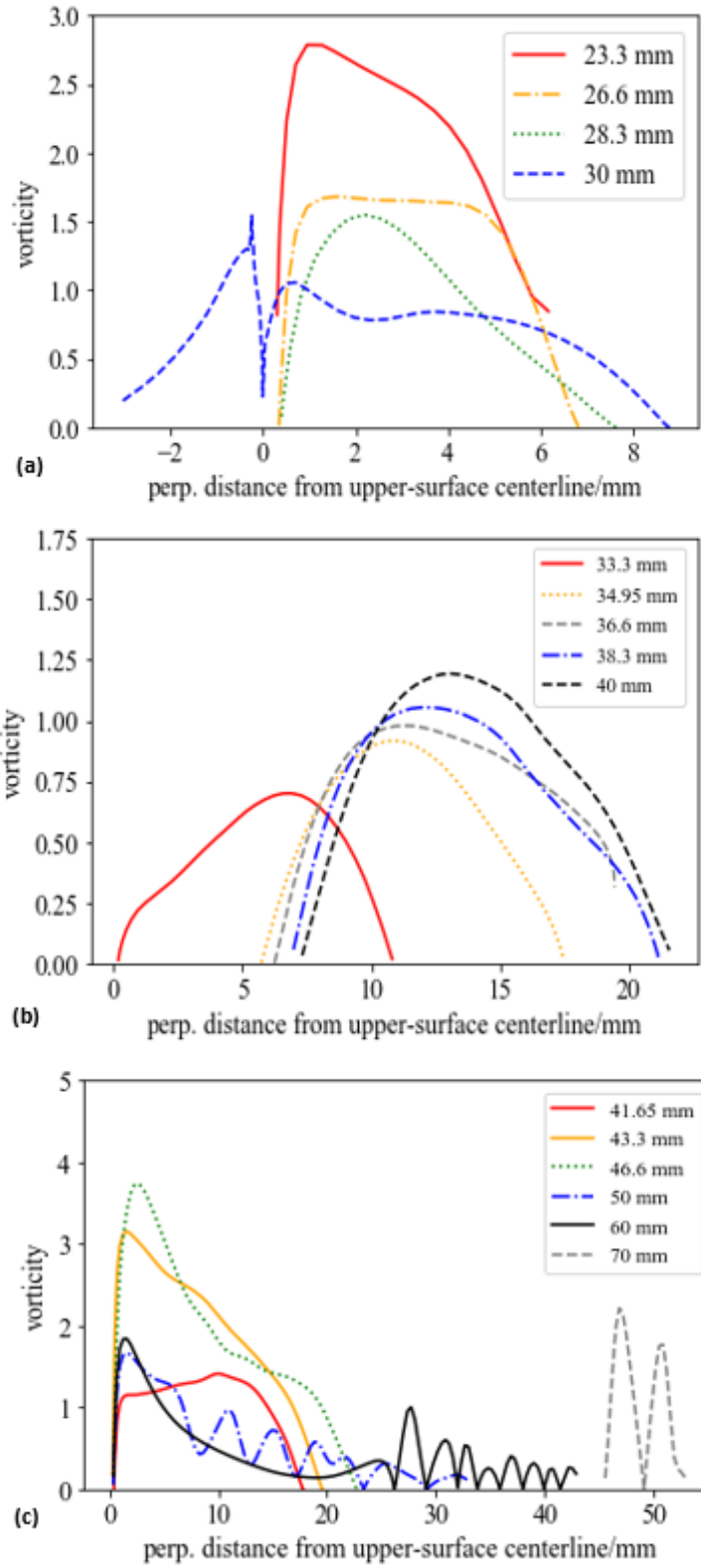
Figure 6.7: Vorticity distribution measured down the symmetrical axis of the primary vortices for a height range of (a) 23.3mm mm to 30 mm (b) 33.3mm to 40mm and (c) 41.65mm to 70mm.
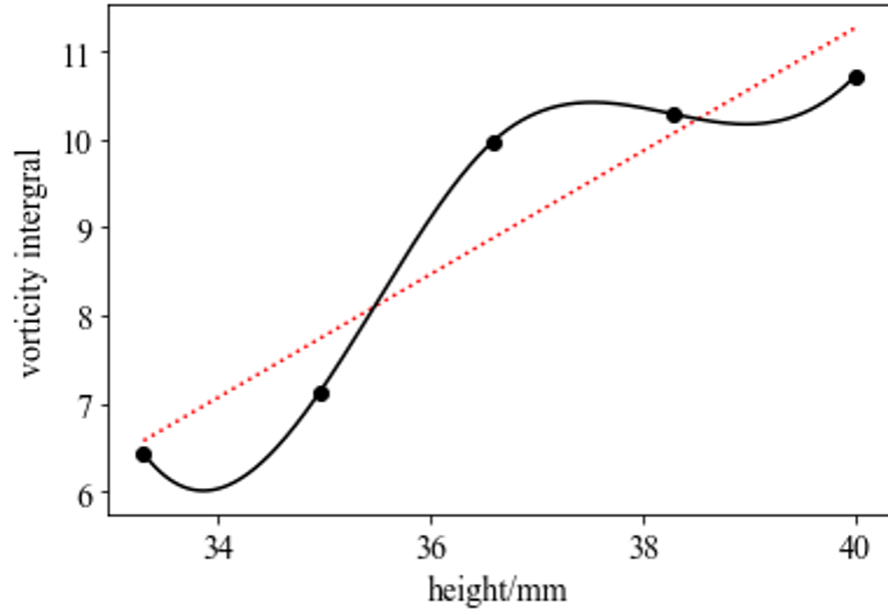
Figure 6.8: Integral calculation performed for the vorticity curves in Figure 6.7.
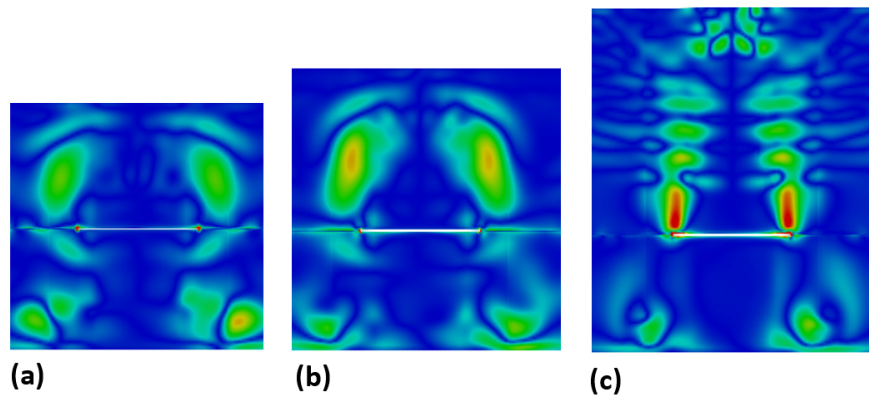
Figure 6.9: Vorticity contour plots for the geometry set at a height of (a) 34.95 mm (b) 40 mm and (c) 50 mm.

CHAPTER 7

CLOSING CONCLUSIONS AND FUTURE RECOMMENDATIONS

7.1 Summary of the Current Work

A variety of topics have been explored in this thesis, including the detailed effects of incremental frequency on aspects such as fluid structure, thermal distribution and the degree of dynamic stability between wave periods. Simulations have been conducted to show the optimum configurations based on heat transfer and thermal mixing. Detailed studies of thermal boundary layer development across different boundaries and furthermore across different frequencies provide a window into the mechanisms behind thermal heat transfer and an increased understanding of the fluid behaviour in acoustic propagation. Validation in Section 3.3 for a solver built for OpenFOAM CFD shows good correlation with experimental results for Dehbani et al. [13]. This, coupled with comparisons between thermal distributions of the OpenFOAM convection model for a thermal boundary layer with Kolar [116] on a specific meshing strategy means that a robust approach was established to explore the knowledge gaps discussed in the literature.

The detailed frequency parameterisation study in Chapter 4 essentially resolves the fluid behaviour into regimes of specified behaviour. Steady behaviour observed through a characteristic and proportional correlation between vorticity in the Schlichting layer and incremental increase in frequency are observed up to a value of 450 kHz. The flow structure in this regime is characterised by a classic symmetrical layout with characteristic circulatory currents observed in the literature. Beyond this, the sudden increase in vorticity values, corresponding with the breakdown of the symmetry in the flow result in a structure with concentrated circulation around the acoustic source. At this point, it would be useful to make comparisons with findings in Chapter 6. Recall that an "optimum range" was alluded to in classifying the best heights for the most effective enhanced heat transfer. It should be further recalled that within this optimum range, where a parabolic trend is observed in heat transfer with height-increase, that the flow structure showed characteristic appearance from the literature akin to the classic pair of circulatory currents. Outside of this range, multiple circulatory cells form. In the context of application,

the knowledge is important for filling the gaps for the flow control aspects of the literature. Importance has been emphasised and correlated between the overall flow structure, its stability and its effects on heat transfer. Chapter 1 should be referred to, in particular the closing objectives of the research. A primary aim was to build upon existing work and to widen the knowledge base for engineering applications. In this regard, this has been achieved by performing a detailed frequency study with a height resolution of increments and correlating the nature of the flow structure with other aspects such as geometry height. Thus connections can be made between Chapter 4 and Chapter 6 in this regard.

At the same time, the knowledge of overall dynamic stability has been built upon whilst also looking at the detailed behaviour of the fluid within one wave period. The simulations ascertained that dynamic stability was achieved through the visualisation of velocity plots but a closer look at the behaviour within one period conveyed the effects on thermal mixing and heat distribution. Through a detailed resolution of the wave period, the mechanism of enhanced transfer is understood by identifying the mechanism behind the change in heat distribution across it. It is observed for example, that the net cooling originates from the axis of symmetry and expands outwards. This is important for the ability to predict the net behaviour of fluid flow when designing a system with optimum heat transfer and contributes considerably to a niche in the literature for the understanding of detailed flow mechanisms in acoustic streaming.

Within one period, the simulations were able to resolve characteristic expansion and contractions between two ultrasonic frequencies. They were subsequently compared and correlated with the calculated acoustic force across one wave period for each frequency. The comparison shows a considerable correlation between the acoustic force and boundary layer size variation across the period, specifically highlighting the phase change between the two frequencies. From these observations, three important factors were identified; that the correlations were primarily observed on the bottom wall of the geometry, that the acoustic force had a clear effect on the disruption to the thermal boundary layer structure at this point and that the larger frequency had a greater effect on size variation and thus the subsequent thermal mixing in the fluid. The findings are important for several reasons. Observations of the greatest effects on the boundary layer on the bottom surface leaves room for further study of this configuration, a point that will be discussed further in the recommendations of Section 7.2.1. Why for example, are the effects on the boundary layer most prominent at this point? Is there a further parameterisation study that can allow us to predict the design of a system of optimum heat transfer based on this finding? These are all questions that can be investigated in further investigations in future work. Furthermore, they would add further depth and help provide additional answers to the findings in Chapter 6. Is the idea of an "optimum range" for geometry heights consistent across all configurations? Additionally, what are the core mechanisms behind an optimum heat transfer at a specific range of heights coupled with the observation that the bottom surface located directly under the acoustic transducer demonstrates the most prominent and correlative effects on the thermal boundary layer? Thus Section 7.2 outlines in greater detail how an

approach to further work could be evaluated.

7.2 Future Recommendations

7.2.1 *Response Surface Model Formulation*

As discussed previously, this is extremely important to home in on the understanding of boundary layer development in acoustic flow and its consequential effects on heat transfer enhancement. Further development of a new methodology can be carried out with the prime study being the orientation of the thermal boundary layer in relation to the acoustic source. It has been established in Chapter 5 that the most prominent and predictable effects were observed on the bottom wall, with the distinctive expansions and contractions. The thesis already provides a comprehensive study of boundary layer development at different locations for a specified geometry in the form of Figure 5.16. It is interesting to note that whilst the bottom wall exhibits the characteristics discussed, the sidewalls exhibit a net increase in boundary layer size. Two distinct locations in the geometry demonstrate characteristically defined behaviour for boundary layer traits. The observations leave plenty of room for a more geometry-orientated parametric study with additional dimensions to provide an engineer with a Response Surface Model (RSM) of simple geometry characteristics. The reason for this is the number of variables that should be considered. Examples include the proximity of the boundary of interest to the acoustic source in the form of a perpendicular dimension such as height- Chapter 6 already presents the commencements of such a variable study in the form of height variation. However, to build a fully integrated RSM, additional parameters need to be considered; frequency, vertical boundary layer position, horizontal boundary layer position and boundary-surface orientation angle in relation to the acoustic source are such examples. The resulting product makes use of these parameters in the form of explanatory variables in conjunction with a response variable which in this case would be heat transfer enhancement.

7.2.2 *Pipe Flow Effects*

Both the work carried out in this thesis and that of the literature review present a distinctive fluid domain that is either in a thermoacoustic streaming configuration or as a stationary bulk, characteristic of tank. A considerable gap exists in the effects on a fluid with a defined velocity in a pipe configuration. There is sufficient scope in the work to further build on the robustness of the model by incorporating fluid velocity into the system of equations without divergence of the solution. So far, investigations by Merkli and Thomann [124] have shown experimental observations for turbulence transition in oscillating pipe flow- specifically, transition in the Stokes layer at a wide range of transition Reynold's numbers and provides a window into the nature of turbulence occurrence through periodic bursts. Further work on experimental resonance in a tube geometry was carried out by the same authors [125] to identify the effects of cooling and heating on the tube wall- Again the scope in CFD is evident

to study the resonance effects on acoustic streaming in more detail by building on the existing model. Additionally, as discussed in Section 4.6, aswell as a thermal boundary layer study, the research could also benefit from a velocity boundary study in the context of pipe flow. Again, as per findings by Guo and Sun [65] who observed a breakdown in circulatory structures when a flow rate was applied, it would be important to calibrate the flow so that the effects of circulation by acoustically induced flow can still be observed. Another potential avenue is to study the effects of heating as well as cooling both in an experimental and a computational context. Further fundamental questions could be addressed such as to the effects of acoustic streaming on heating. This is a significant gap in the research.

7.2.3 *Validation and Further Study of Behaviour at the Acoustic Source*

It should be recalled from the literature that work carried out by Trujillo [19], Rahimi et al. [97] and Moudjed et al. [99] derived models to approximate the velocity profile at the tip of an acoustic source (in this case being a horn tip). The bulk of the work in this thesis primarily focuses on the fluid domain in its entirety (coupled with individual areas of study of boundary surfaces to resolve the boundary layer). There is additional room for study of velocity distributions across the surface of the acoustic boundary. For this, further experimentation would need to take place in order to further validate the model. Based on experimental results, work can be done to improve on its robustness in other areas such as at the acoustic source by comparing its approximation to said-experimental results. With this in mind, an additional objective would be to understand the lengths achieved to approximate the characteristics of the global flow in the overall domain verses the degree of approximation at the acoustic source. The contribution to the overall research in the literature would be to ensure that this model is able to mathematically approximate the model with improved accuracy in comparison to the aforementioned authors whilst also ascertaining the effects on accuracy in the overall bulk of the fluid domain. If both can be obtained then it could be argued that this is a step forward from the work of the previous authors.

7.2.4 *Critical Frequency*

Section 4.5 established a critical frequency, a frequency where the flow underwent a dramatic change in behaviour as demonstrated by Figure 4.22. It was surmised that this was a geometry-dependant quantity owing to the distance travelled by the wave before reflection off the wall boundaries took place. A further development of this initial study would be to conduct another parametisation study on geometry aspects such as area or height and studying the subsequent effects on this critical frequency. In this way, more clearer links could be drawn between acoustic characteristics such as frequency and propagation and fluid characteristics such circulation and geometry. This would further aid in the design and construction of industrial devices such as sonoreactors.

7.2.5 *Transducer Characteristics*

Power analysis of transducers is a significant next step for this research particularly in regards to Chapter 4 where a large range of frequencies is being studied. In this regard, a more realistic context can be applied to any computational findings which would have significant implications for transducer design. The potential work is beneficial as it would form a link between computational and experimental work. Within this work a study of the types of transducers and their effects on acoustic streaming would also be beneficial. Yao et al. [22] provides an extremely good overview of the different types of ultrasonic transducers but he doesn't cover their effects on a fluid. Thus the study of transducers, particularly with different impedance mismatches could be investigated.

Bibliography

[1] S. Lowe, "Ultrasonics", Encyclopedia of Vibration (2001).

[2] T. Schaaf, "'in medtech history' - ultrasound, part 1", Medtech Strategists (2019).

[3] T. Dring, "A steep learning curve: the impact of sonar technology, training, and tactics on the initial years of u.s. navy antisubmarine warfare in world war ii", Warship International, 35–57 (2019).

[4] J. Jagannathan, N. Sanghvi, L. Crum, R. Chun-Po Y abd Medel, A. Dumon, J. Sheehan, L. Steiner, F. Jolesz, and N. Kassell, "High-intensity focused ultrasound surgery of the brain: part 1- a historical perspective with modern applications", Neurosurgery, 201–211 (2009).

[5] B. Goldberg, *Medical diagnostic ultrasound: a retrospective on its 40th anniversary* (Kodak Health Sciences, 1988).

[6] "Introduction to echocardiography and ultrasound imaging", ECG and Echo Learning (2019).

[7] N. Ghani, S. Miralles, V. Botton, D. Henry, H. Hadid, B. Ter-Ovanessian, and S. Marcelin, "Acoustic streaming enhanced mass transfer at a wall", International Journal of Heat and Mass Transfer (2021).

[8] M. Legay, *Enhancement of heat transfer by ultrasound: review and recent advances*, International Journal of Chemical Engineering (2011).

[9] X. Luo, J. Cao, H. Gong, Y. Haipeng, and L. He, "Phase separation technology based on ultrasonic standing waves: a review", Ultrasonics Sonochemistry (2021).

[10] M. Wiklund, R. Green, and M. Ohlin, *Acoustofluidics 14: applications of acoustic streaming in microfluidic devices*, Lab on a Chip (2012).

[11] S. Katzir, *The beginnings of piezoelectricity*, A study in Mundane Physics (Springer, 2006).

[12] S. Lighthill, *Acoustic streaming*, Journal of Sound and Vibration (Elseviere, 1976).

[13] M. Dehbani, M. Rahimi, M. Abolhasani, A. Maghoosi, P. Ghaderi, A. Reza, and A. Alsairafi, *Cfd modelling of convection heat transfer using 1.7 mhz and 20 khz ultrasonic waves: a comparative study* (Springer, 1976).

[14] S. Catarino, J. Miranda, S. Lanceros Mendez, and G. Minas, *Numerical prediction of acoustic streaming in a microcuvette* (Canadian Society for Chemical Engineering, 2014).

[15] F. Trujillo, *A strict formulation of a nonlinear helmholtz equation for the propogation of sound in bubbly liquids. part i: theory and validation at low acoustic pressure amplitudes*, Ultrasonics Sonochemistry (Canadian Society for Chemical Engineering, 2018).

[16] T. Huttenen, M. Malinen, J. Kaipo, P. White, and K. Hynynen, *A full-wave helmholtz model for continous-wave ultrasound transmission*, Transactions on Ultrasonics, Perroelectrics and Frequency Control (Institute of Electrical and Eletronics Engineers Inc, 2005).

[17] M. Liebler, S. Ginter, T. Dreyer, and R. Riedlingler, "Full wave modeling of therapeutic ultrasound: efficient time-domain implementation of the frequency power-law attenuation", The Journal of the Acoustical Society of America (2004).

[18] M. Ovchinnikov, J. Zhou, and S. Yalamanchili, *Acoustic streaming of a sharp edge*, The Journal of the Acoustical Society of America (ASA, 2014).

[19] F. Trujillo, *A computational modelling approach of the jet-like acoustic streaming and heat generation induced by low frequency high power ultrasonic horn reactors*, Ultrasonics Sonochemistry (Canadian Society for Chemical Engineering, 2011).

[20] V. Humphrey, *Ultrasound and matter—physical interactions*, Progress in Biophysics and Molecular Biology (Elsevier, 2007).

[21] T. Mason and J. Lorimer, *Theory, applications and uses of ultrasound in chemistry*, Progress in Biophysics and Molecular Biology (1988).

[22] Y. Yao, Y. Pan, and S. Liu, *Power ultrasound and its applications: a state-of-the-art review*, Ultrasonics Sonochemistry (Elsevier, 2019).

[23] C. Hansen, *Fundamentals of acoustics*, American Journal of Physics (1951).

[24] J. Rayleigh, *Theory of sound* (Dover Publications, 1945).

[25] W. Nyborg, *Acoustic streaming near a boundary* (The Journal of the Acoustical Society of America, 1958).

[26] B. Li and D. Sun, *Effect of power ultrasound on freezing rate during immersion freezing of potatoes*, Journal of Food Engineering (2002).

[27] T. Inada, X. Zhang, Y. Akira, and Y. Kozawa, *Active control of phase change from supercooled water to ice by ultrasonic vibration 1. control of freezing temperature*, International Journal of Heat and Mass Transfer (2001).

[28] X. Zhang, T. Inada, Y. Akira, and Y. Kozawa, *Active control of phase change from supercooled water to ice by ultrasonic vibration 2. generation of ice slurries and effect of bubble nuclei*, International Journal of Heat and Mass Transfer (2001).

[29] Y. Lin and B. Farouk, *Heat transfer in a rectangular chamber with deferentially heated horizontal walls: effects of a vibrating sidewall*, International Journal of Heat and Mass Transfer (2008).

[30] A. Marzo, M. Caleap, and B. Drinkwater, *Acoustic virtual vortices with tunable orbital angular momentum for trapping of mie particles*, Physical Review Letters (American Physical Society, 2018).

[31] M. Settnes and H. Bruus, *Forces acting on a small particle in an acoustical field in a viscous fluid*, Physical Review E (APS Physics, 2012).

[32] R. Uhlenwinkel, R. Meng, and K. Bauckhage, *Investigation of heat transfer from circular cylinders in high power 10 khz and 20 khz acoustic resonant fields*, International Journal of Thermal Sciences (2000).

[33] T. Neighbors and D. Bradley, *Applied underwater acoustics* (2017) Chap. Acoustic Streaming.

[34] M. Faraday, "On a peculiar class of acoustical figures; and on certain forms assumed by groups of particles upon vibrating elastic surfaces", Phil. Trans. R. Soc. (1885).

[35] Y. Suh, *Encyclopedia of microfluidics and nanofluidics* (2008) Chap. Acoustic Streaming.

[36] B. Nowling, "Gas flow measurements by nmr", Progress in Nuclear Magnetic Resonance Spectroscopy (2008).

[37] K. Suslick (2003) Chap. Sonoluminescence and Sonochemistry.

[38] C. Peng, M. Chen, J. Spicer, and X. Jiang, "Acoustics at the nanoscale (nanoacoustics): a comprehensive literature review. part i: materials, devices and selected applications", Sensors and Actuators A: Physical (2021).

[39] A. Kumar, P. Gogate, and A. Pandit, "Mapping of acoustic streaming in sonochemical reactors", American Chemical Society (2007).

[40] D. Collins, B. Khoo, Z. Ma, A. Winker, R. Weser, H. Schmidt, J. Han, and Y. Ali, "Selective particle and cell capture in a continuous flow using micro-vortex acoustic streaming", Lab on a Chip (2017).

[41] I. Oyama T Imashiro, T. Kuriyama, H. Usui, A. Keita, A. Tetsushi, A. Morikawa, K. Kazuhide, O. Takahara, and K. Takemura, "Acoustic streaming induced by mhz-frequency ultrasound extends the volume limit of cell suspension culture", The Journal of the Acoustical Society of America (2021).

[42] H. Spengler and T. Coakley, "Ultrasonic trap to monitor morphology and stability of developing microparticle aggregates", Journal of Applied Physics (2003).

[43] H. Li, J. Friend, and L. Yeo, "Surface acoustic wave concentration of particle and bioparticle suspensions", Biomedical Microdevices (2007).

[44] A. Bernassau, P. Glynne-Jones, F. Gesellchen, M. Riehle, and D. Cumming, "Controlling acoustic streaming in an ultrasonic heptagonal tweezers with application to cell manipulation", Ultrasonics (2014).

[45] A. Bernassau, Ong, Y. Ma, P. MacPherson, C. Courtney, M. Richle, B. Drinkwater, and D. Cumming, "Two-dimensional manipulation of micro particles by acoustic radiation pressure in a heptagon cell", Ultrasonics (2011).

[46] P. Richardson, "Heat transfer from a circular cylinder by acoustic streaming", Journal of Fluid Mechanics (1967).

[47]B. Baran, K. Machaj, Z. Malecha, and K. Tomczuk, "Numerical study of baroclinic acoustic streaming phenomenon for various flow parameters", Energies (2022).

[48]D. Koster, "Numerical simulation of acoustic streaming on surface acoustic wave-driven biochips", SIAM Journal on Scientific Computing (2006).

[49]S. Maramizonouz, M. Rahmati, A. Link, T. Franke, and Y. Fu, "Numerical and experimental studies of acoustic streaming effects on microparticles/droplets in microchannel flow", International Journal of Engineering Science (2021).

[50]E. Trinh, "Acoustic streaming in microgravity: flow stability and heat transfer enhancement", NASA (2013).

[51]E. Trinh, "Acoustic streaming and heat and mass transfer enhancement", NASA (2013).

[52]K. Hasegawa et al, "Acoustic manipulation of droplets under reduced gravity", Scientific Reports (2019).

[53]M. Charrier-Mojtabi, A. Fontaine, and A. Mojtabi, "Influence of acoustic streaming on thermo-diffusion in a binary mixture under microgravity", International Journal of Heat and Mass Transfer (2012).

[54]S. Fischbach, *Streaming effects in liquid injection rocket engines with transverse mode oscillations* (2007).

[55]N. Riley, *Acoustic streaming, in theoretical and computational fluid dynamics* (1998).

[56]L. Laundau and E. Lifshitz, *Fluid mexchanics*, Vol. 6, Theoretical Physics (1987).

[57]M. Tan and L. Yeo, "Hybrid finite-difference/lattice boltzmann simulations of microchannel and nanochannel acoustic streaming driven by surface acoustic waves", Physical Review Fluids **3** (2018).

[58]B. Tajik, M. Saffar-Avval, A. Abdullah, and H. Mohammad-Abadi, *Numerical simulation of acoustic streaming for nonlinear standing ultrasonic waves in water inside an axisymmetric enclosure*, Engineering Applications of Computational Fluid Mechanics (2012).

[59]P. Osipov and I. Almakaev, *Simulation of particles drift and acoustic streaming of polytropic viscous gas in a closed tube*, Lobachevskii Journal of Mathematics (2019), pp. 802–807.

[60]Q. Wan and A. Kuznetsov, *Numerical study of the efficiency of acoustic streaming for enhancing heat transfer between two parallel beams*, Flow, Turbulence and Combustion (2003).

[61]R. Fand and J. Kaye, *Acoustic streaming near a heated cylinder*, The Journal of the Acoustical Society of America (1960), pp. 579–584.

[62]J. Marshall and W. Junru, *Acoustic streaming, fluid mixing, and particle transport by a gaussian ultrasound beam in a cylindrical container*, Physics of Fluids (1960).

[63] J. Lei, P. Glynne-Jones, and M. Hill, *Acoustic streaming in the transducer plane in ultrasonic particle manipulation devices*, Lab on a chip (1960).

[64] S. Bahrani, R. Herbaut, R. Laurent, K. Azzouz, and A. Bonetemps, *Experimental investigation of thermal and flow mixing enhancement induced by rayleigh-like streaming in a milli-mixer*, Thermal Science and Engineering Progress (2019).

[65] H. Guo and H. Sun, "Theoretical study of acoustic streaming induced cooling effect in the microscale", IEEE Ultrasonics Symposium (2008).

[66] C. Zhang, *Unveiling of the mechanisms of acoustic streaming induced by sharp edges*, Vol. 102, Physical Review E (American Physical Society, 2020).

[67] M. Setareh, M. Saffar-Avval, and A. Abdullah, *Experimental and numerical study on heat transfer enhancement using ultrasonic vibration in a double-pipe heat exchanger*, Microfluidics and Nanofluidics (2011), pp. 619–625.

[68] R. Rivlin and J. Ericksen (1955) Chap. Stress-deformation relations for isotropic materials.

[69] M. Setareh, M. Saffar-Avval, and A. Abdullah, *Heat transfer enhancement in an annulus under ultrasound field: a numerical and experimental study*, International Communications in Heat and Mass Transfer (2020).

[70] N. Nguyen and R. White, *Acoustic streaming in micromachined flexural plate wave devices: numerical simulation and experimental verification*, Ultrasonics, Ferroelectrics and Frequency Control, IEEE Transactions (2000), pp. 1463–1471.

[71] K. Frampton, K. Minor, and S. Martin, *Acoustic streaming in micro-scale cylindrical channels*, Acoustic streaming in micro-scale cylindrical channels (2004), pp. 1121–1129.

[72] D. Hyun, D. Lee, and B. Loh, *Investigation of convective heat transfer augmentation using acoustic streaming generated by ultrasonic vibrations*, International Journal of Heat and Mass Transfer (2005), pp. 703–718.

[73] P. Muller and H. Bruus, *Numerical study of thermoviscous effects in ultrasound-induced acoustic streaming in microchannels*, Physical Review E (American Physical Society, 2014).

[74] B. sajjadi, A. Raman, and I. Shaliza, *Influence of ultrasound power on acoustic streaming and micro-bubbles formations in a low frequency sono-reactor: mathematical and 3d computational simulation*, Ultrasonics Sonochemistry (2015), pp. 193–203.

[75] G. Mozurkewich, *Heat transfer from a cylinder in an acoustic standing wave*, The Journal of the Acoustical Society of America (1995), pp. 2209–2216.

[76] M. Talebi, M. Setareh, M. Saffar-Avval, and R. Abardeh, *Numerical investigation of natural convection heat transfer in a cylindrical enclosure due to ultrasonic vibrations*, Ultrasonics (2017).

[77]A. Riaud, M. Baudoin, O. Bou Matar, J. Thomas, and P. Brunel, "Influence of viscosity on acoustic streaming in sessile droplets: an experimental and a numerical study with a streaming source spatial filtering (sssf) method", Journal of Fluid Mechanics (2017).

[78]J. Piercy and J. Lamb, "Acoustic streaming in liquids", Mathematical and Physical Sciences (1952).

[79]H. Bruus, "Ultrasound rays in droplets: the role of viscosity and caustics in acoustic streaming", Focus on Fluids (1952).

[80]X. Zhang, J. Macoskey, K. Ives, G. Owens, H. Gurm, J. Shi, M. Pizzuto, C. Cain, and Z. Xu, *Non-invasive thrombolysis using microtripsy in a porcine deep vein thrombosis model*, Ultrasound in Medicine Biology (2017), pp. 1378–1390.

[81]J. Seo and Y. Kim, *Ultrasound imaging and beyond: recent advances in medical ultrasound*, Biomedical engineering letters (2017), pp. 57–58.

[82]T. Yu, Z. Wang, and T. Mason, *A review of research into the uses of low level ultrasound in cancer therapy*, Ultrasonic Sonochemistry (2004), pp. 95–103.

[83]M. Solovchuk, W. Tony, M. Thiriet, and W. Lin, *Effect of acoustic streaming on tissue heating due to high-intensity focused ultrasound* (2012).

[84]J. Huang, R. Glynn Holt, R. Cleveland, and R. Roy, *Experimental validation of a tractable numerical model for focused ultrasound heating in flow-through tissue phantoms*, Journal of the Acoustical Society of America (2004), pp. 2451–2458.

[85]T. Wessapan and P. Rattanadecho, *Acoustic streaming effect on flow and heat transfer in porous tissue during exposure to focused ultrasound*, Case Studies in Thermal Engineering. (2020).

[86]J. Pennes, *Analysis of tissue and arterial blood temperatures in the resting human forearm*, Journal of Applied Physiology (1948), pp. 93–122.

[87]S. Mozo, C. Llena, and L. Forner, *Review of ultrasonic irrigation in endodontics: increasing action of irrigating solutions*, Ultrasounds in Endontics (2012).

[88]B. Verhaagen, C. Boutsioukis, L. Van der Sluis, and M. Versluis, *Acoustic streaming induced by an ultrasonically oscillating endodontic file*, The Journal of the Acoustical Society of America (2014), pp. 1717–1730.

[89]C. Chun-Lin and F. Te-Yun L. Yiin-Kuen, "The suitability of ultrasonic and megasonic cleaning of nanoscale patterns in ammonia hydroxide solutions for particle removal and feature damage", Semiconductor Science and Technology (2020).

[90]D. Thanu, A. Antoniswamy, V. Swaminathen, E. Srinadhu, N. Dole, and M. Zhao, *Surfactants in precision cleaning* (2022).

[91]G. Gale and A. Busnaina, "Roles of cavitation and acoustic streaming in megasonic cleaning", Particulate Science and Technology (2007).

[92]A. Busnaina and T. Elsawy, "Post-cmp cleaning using acoustic streaming", Journal of Electronic Materials (1998).

[93] A. Busnaina, *Fine particle removal using high frequency acoustic streaming* (2021).

[94] L. Yifan, D. Dekel, and O. Manor, "Surface acoustic wave mitigation of precipitate deposition on a solid surface-an active self-cleaning strategy", Applied Materials and Interfaces (2021).

[95] V. Kapila, P. Deymier, H. Shende, V. Pandit, S. Raghavan, and F. Eschbach, "Acoustic streaming effects in megasonic cleaning of euv photomasks: a continuum model.", 25th Annual BACUS Symposium on Photomask Technology (2012).

[96] K. Bakhtari, O. Rasim, P. Makaram, A. Busnaina, and J. Park, "Experimental and numerical investigation of nanoparticle removal using acoustic streaming and the effect of time", Journal of The Electrochemical Society (2006).

[97] M. Rahimi, S. Movahedirad, and S. Shahhosseini, *Cfd study of the flow pattern in an ultrasonic horn reactor: introducing a realistic vibrating boundary condition*, Ultrasonics Sonochemistry (2017), pp. 359–374.

[98] H. Schlichting, *Boundary layer theory* (McGraw-Hill, 1979).

[99] B. Moudjed, V. Botton, D. Henry, H. Hadid, and J. Garandet, *Scaling and dimensional analysis of acoustic streaming jets*, Physics of Fluids (2014).

[100] J. Eisener, T. Nowak, C. Cairos, F. Reuter, and R. Mettin, *Characterization of acoustic streaming beyond 100 mhz*, Vol. 70, Physics Procedia (2015), pp. 151–154.

[101] H. Bailliet, V. Gusev, R. Raspet, and R. Hiller, *Acoustic streaming in closed thermoacoustic devices*, The Journal of the Acoustical Society of America (2001).

[102] G. Penelet, P. Lotton, V. Gusev, and M. Bruneau, *On the use of acoustic streaming for heat transfer applications*, ICUltrasonics (2007).

[103] G. Swift, *Thermoacoustic engines*, Vol. 84, The Journal of the Acoustical Society of America (1988), pp. 1145–1180.

[104] G. Lebon, G. Salloum Abou Jaoude, D. Eskin, L. Tzanakis, K. Pericleous, and P. Jarry, *Numerical modelling of acoustic streaming during the ultrasonic melt treatment of direct-chill dc casting*, Vol. 54, Ultrasonic Chemistry (2019), pp. 171–182.

[105] T. Yamamoto, K. Kubo, and S. Komarov, *Characterization of acoustic streaming in water and aluminum melt during ultrasonic irradiation*, Vol. 71, Ultrasonics Sonochemistry (2019).

[106] P. Parvizian, M. Rahimi, N. Azimi, and A. Alsairafi, "Cfd modeling of micromixing and velocity distribution in a 1.7-mhz tubular sonoreactor", Chemical Engineering Technology **37**, 113–122 (2014).

[107] S. Sadhal, "Analysis of acoustic streaming by perturbation methods", Lab on a Chip (2012).

[108] W. Nyborg, *Acoustic streaming due to attenuated plane waves* (The Journal of the Acoustical Society of America, 1953).

[109] I. Rahbari and G. Paniagua, "Acoustic streaming in turbulent compressible channel flow for heat transfer enhancement", Journal of Fluid Mechanics (2020).

[110] S. Rashwan, I. Dincer, and A. Mohany, "Investigation of acoustic and geometric effects on the sonoreactor performance", Ultrasonics Sonochemistry (2020).

[111] F. Navarro-Brull, A. Teixeira, G. Giri, and R. Gomez, "Enabling low power acoustics for capillary sonoreactors", Ultrasonics Sonochemistry (2019).

[112] A. Saeed and A. Alkaabi, *Fundamentals of nuclear reactors* (2019).

[113] D. Ghosh, D. Mohanty, R. Raj, and S. Saha, "Onset of nucleate boiling, void fraction, and liquid film thickness", Microchannel Phase Change Transport Phenomena (2016).

[114] J. Xu, Y. Gan, D. Zhang, and X. Li, "Microscale heat transfer enhancement using thermal boundary layer redeveloping concept", International Journal of Heat and Mass Transfer (2004).

[115] H. Li and M. Nalim, "Thermal-boundary-layer response to convected far-field fluid temperature changes", Journal of Heat Transfer (2008).

[116] M. Kolar, "Experimental investigation of the thermal boundary layer in a confined liquid", NASA (1966).

[117] Y. Asakura, K. Yasuda, S. Kato, Y. Kojima, and S. Koda, "Development of a large sonachemical reactor at a high frequency", Journal of Chemical Engineering (2008).

[118] L. Spigarelli, N. Vasile, C. Pirri, and G. Canavese, "Numerical study of the effect of channel aspect ratio on particle focusing in acoustophoretic devices", Scientific Reports (2020).

[119] T. Ch., "Acoustic streaming in a waveguide with slowly varying height", Journal of the Acoustical Society of America **75** (1984).

[120] A. Gubaidullin and A. Pyatkova, "Acoustic streaming in a cylindrical cavity at variation of its radius and boundary conditions", Thermophysics and Aeromechanics **26** (2019).

[121] C. Eckhart, "Vortices and streams caused by sound waves", 68 (1948).

[122] H. Hertz, "Standing- wave acoustic trap for nonintrusive positioning of microparticles", Journal of Applied Physics (1995).

[123] J. Spengler and M. Jekel, "Ultrasound conditioning of suspensions–studies of streaming influence on particle aggregation on a lab- and pilot-plant scale", Ultrasonics (2000).

[124] P. Merkli and H. Thomann, "Transition to turbulence in oscillating pipe flow", Journal of Fluid Mechanics **68** (1974).

[125] P. Merkli and H. Thomann, "Thermoacoustic effects in a resonance tube", Journal of Fluid Mechanics **70** (1973).